CFD MODELING IN DESIGN AND EVALUATION OF AN ENDOVASCULAR CHEMOFILTER DEVICE

by

Nazanin Maani

A Dissertation

Submitted to the Faculty of Purdue University

In Partial Fulfillment of the Requirements for the degree of

Doctor of Philosophy

Weldon School of Biomedical Engineering

West Lafayette, Indiana

December 2019

THE PURDUE UNIVERSITY GRADUATE SCHOOL
STATEMENT OF COMMITTEE APPROVAL

Dr. Vitaliy L Rayz, Chair
Weldon School of Biomedical Engineering
Dr. Craig J Goergen
Weldon School of Biomedical Engineering
Dr. Eric A Nauman
School of Mechanical Engineering
Dr. Luis Solorio
Weldon School of Biomedical Engineering
Dr. David M Umulis
School of Agricultural & Biological Engineering

Approved by:
Dr. George R. Wodicka
Head of the Graduate Program

To my Mom and Dad who made this journey possible with their continuous encouragement, love, and support.

ACKNOWLEDGMENTS

Firstly, I would like to thank my advisor, Vitaliy Rayz, for being an amazing mentor and teacher throughout my PhD. Thank you for encouraging me to challenge myself, and think about the big picture. I'll remain grateful for your continuous patience and flexibility, to always make time for your students and prioritize our professional growth.

I also would like to thank my incredible committee, Dr. Craig Goergen, Dr, Eric Nauman, Dr, Luis Solorio, and Dr. David Umulis, for all the guidance and inspiration that you provided and your input to my work. Thank you for your support, feedback, and helping me approach my work from different angles. To all members of Rayz lab, thank you for being great people to work with on a daily basis, especially, to Tyler Diorio, thank you for your editing assistance and being a good listener. Additionally, I would like to express my appreciation for all the staff of the BME department at Purdue, for their behind the scenes work, administrative help, and professional advice.

I would like to express my appreciation to all of our collaborators in the Chemofilter group; to the head of Chemofilter group, Dr. Steven Hetts, thank you for your continuous support and positive attitude during our work together. To Dr. Nitash Balsara, thank you for your invaluable input and feedback on my work. To Dr. Julia Greer and Daryl Yee, thank you for providing us the CAD files of architected material and all the fruitful discussions. To Colin Yee, thank you for sharing your experimental data and great conversations. To Teri Moore, thank you for arranging all the meetings as well as the professional advices that you provided to me. I would also like to express my gratitude towards the animals that have been and will be sacrificed in the Chemofilter studies.

I would also like to acknowledge my funding source: the NIH NCI grant R01CA194533, titled "Endovascular Chemofiltration: Optimizing Removal of Chemotherapeutics and Nanoparticles from the Blood to Reduce Toxicity and Improve Image-Guided Drug Therapy".

Finally, I would like to share my gratitude to my family and friends who were always there for me during this journey. To my parents and siblings, thank you for all your enthusiasm and unwavering belief in me. I would also like to appreciate J.S. Bach, whose music has been the companion of my long study days and nights since high school. And last but far from the least, to my partner, Peter, thank you for your continuous love, for moving to Indiana to accompany me and for offering many light hearted moments through the hard days. I'm grateful to have you besides me in this chapter of my life.

TABLE OF CONTENTS

LIST OF TABLES

LIST OF FIGURES

NOMENCLATURE

This section is the nomenclature of Chapter 4

c	molar concentration of a single electrolyte, mol/m^3
c_i	concentration of species *i*, mol/m^3
c_T	total solution concentration, mol/m^3
c_0	concentration of solvent, mol/m^3
D_i	diffusion coefficient of species *i*, m^2/s
D_{eff}	effective diffusion coefficient, m^2/s
$\mathfrak{D}$	diffusion coefficient of electrolyte, based on a thermodynamic driving force (Stefan-Maxwell diffusion coefficients), m^2/s
$\mathfrak{D}_{ij}$	diffusion coefficient for interaction of species *i,* and *j*, m^2/s
F	Faraday's constant, 96,487 C/equiv
$\mathbf{i}$	current density, A/m^2
K_{ij}	friction coefficient for interaction of species *i,* and *j*, J.s/m^5
m	molality of a single electrolyte, mol/Kg
n	number of electrons involved in electrode reaction
N_i	flux of species *i*, mol/m^2.s
R	universal gas constant
$\mathcal{R}_i$	rate of homogeneous elimination of species *i* (source term), mol/cm^3.s
s_i	stoichiometric coefficient of species *i*
t_+^0	transference number of species *i* with respect to the velocity of species 0
T	absolute temperature
u_i	mobility of species *i*
$\mathbf{v}$	velocity, m/s
$\mathbf{v}_i$	velocity of the species *i*, m/s
z_i	charge number of species *i*
γ_{+-}	mean molar activity of an electrolyte

κ	ionic conductivity
μ_e	chemical potential of an electrolyte, J/mol
μ_i	electrochemical potential of species i, J/mol
ν	Number of moles of ions into which a mole of electrolyte dissociates
ν_+, ν_-	Number of moles of cations and anions into which a molecule of electrolyte dissociates
ψ	electrostatic potential

subscripts

+	cation
-	anion
0	solvent
cb	concentrated binary
dnb	dilute-non-binary
db	dilute-binary
eff	effective
r	resin
s	solution

ABSTRACT

Author: Maani, Nazanin. PhD
Institution: Purdue University
Degree Received: December 2019
Title: CFD Modeling in Design and Evaluation of an Endovascular Chemofilter Device
Committee Chair: Vitaliy Rayz

Intra-Arterial Chemotherapy (IAC) is a preferred treatment for the primary liver cancer, despite its adverse side-effects. During IAC, a mixture of chemotherapeutic drugs, e.g. Doxorubicin, is injected into an artery supplying the tumor. A fraction of Doxorubicin is absorbed by the tumor, but the remaining drug passes into systemic circulation, causing irreversible heart failure. The efficiency and safety of the IAC can be improved by chemical filtration of the excessive drugs with a catheter-based Chemofilter device, as proposed by a team of neuroradilogists.

The objective of my work was to optimize the hemodynamic and drug binding performance of the Chemofilter device, using Computational Fluid Dynamics (CFD) modeling. For this, I investigated the performance of two distinct Chemofilter configurations: 1) a porous "Chemofilter basket" formed by a lattice of micro-cells and 2) a non-porous "honeycomb Chemofilter" consisting of parallel hexagonal channels. A multiscale modeling approach was developed to resolve the flow through a representative section of the porous membrane and subsequently characterize the overall performance of the device. A heat and mass transfer analogy was utilized to facilitate the comparison of alternative honeycomb configurations.

A multiphysics approach was developed for modeling the electrochemical binding of Doxorubicin to the anionic surface of the Chemofilter. An effective diffusion coefficient was derived based on dilute and concentrated solution theory, to account for the induced migration of ions. Computational predictions were supported by results of *in-vivo* studies performed by collaborators. CFD models showed that the honeycomb Chemofilter is the most advantageous configuration with 66.8% drug elimination and 2.9 mm-Hg pressure drop across the device. Another facet of the Chemofilter project was its surface design with shark-skin inspired texturing, which improves the binding performance by up to 3.5%. Computational modeling enables optimization of the chemofiltration device, thus allowing the increase of drug dose while reducing systemic toxicity of IAC.

CHAPTER 1. INTRODUCTION

1.1 Chemofilter Device and its Significance

Hepatocellular carcinoma (HCC), the primary liver cancer, is the third leading cause of cancer death worldwide [1]. In cases that are not amenable to surgery, Intra-Arterial Chemotherapy (IAC) is the most common HCC treatment [2, 3]. During the hepatic IAC procedure, chemotherapeutic drugs are injected to the hepatic arteries that supply HCC tumors, via catheterization of the femoral artery. These drugs are subsequently injected over the course of a 10 minute period, depending on patient anatomy or specific tumor conditions. Localization of the chemotherapy agents in IAC allows targeted drug delivery to the tumor, as opposed to the systemic intravenous chemotherapy. However, up to 50-70% of IAC drugs, such as doxorubicin (Dox), pass through the liver and accumulate near healthy organs, thus lowering the treatment efficiency. Clinical [4-10] and experimental [11-13] studies show that tumor suppression linearly increases with increasing the Dox dose. However, the recommended dosage of IAC is greatly limited by the detrimental cardiotoxicity induced at doses above 360 mg, known to cause irreversible heart failure [14-18].

Chemofilter is a novel catheter-based endovascular filtration device that chemically binds selected drugs to its surface in order to remove them from blood. The Chemofilter is temporarily deployed from a catheter in a vein distal to the organ undergoing IAC infusion and remains in place for the duration of the procedure. In the context of HCC, IAC would deliver Dox to the liver via the hepatic artery while the Chemofilter would capture the excess Dox as it exits through the hepatic veins or inferior vena cava (IVC) and before the drug could reach the heart and other organs, as shown in Figure 1-1.

The idea of endovascular chemofiltration for enhancing the IAC procedure was initiated by Dr. Hetts' group at the University of California, San Francisco (UCSF), where they developed and designed the first prototype of the Chemofilter. The main goal of the Chemofilter design is to increase tumor suppression by increasing the drug dose, while decreasing the toxicity of the IAC procedure. Consequently, it is expected that using the Chemofilter during the IAC will reduce the number of the chemotherapy sessions, e.g. requiring 2 sessions instead of current average of 3-5 sessions, thus improving the overall cost and effectiveness of the procedure [14].

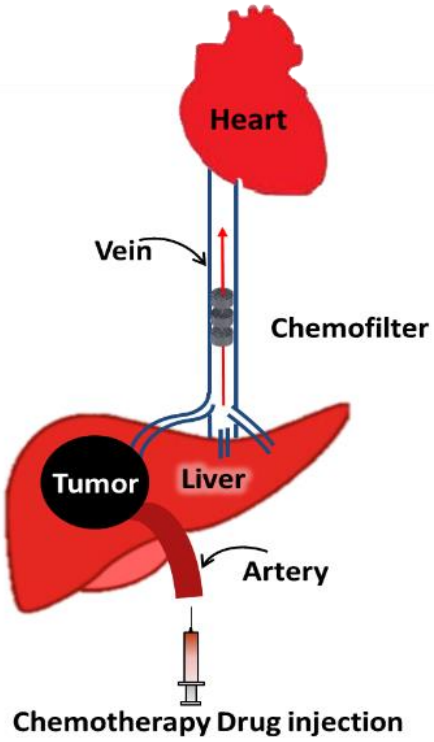

Figure 1-1 Schematics of IAC procedure and Chemofilter deployment in the hepatic vein

The Chemofilter development is a multidisciplinary project which requires design of the overall shape of the Chemofilter for optimal hemodynamics, design of its surface for enhanced near-wall flow dynamics and drug binding, design of stable chemical absorbers which make strong bonds with Dox and do not leach into the blood stream, and, finally, design of safe methods for catheterization, deployment and removal during the IAC procedure. Examining each of these aspects requires various *in silico*, *in vitro*, and *in vivo* studies by cross-disciplinary groups of scientists, engineers, and clinicians.

My PhD project was mainly focused on optimization of the hemodynamics and binding performances of the device with Computational Fluid Dynamics (CFD) methods, while other groups were studying various binding mechanisms (e.g. ion exchange, DNA binding, magnetic binding) with *in vitro* and *in vivo* porcine experiments. The CFD analysis of the Chemofilter device provides guidance to collaborators for more efficient experiments and minimizes the cost and time of the experimental studies, as well as the number of required animal studies.

1.2 Background

To reduce the side effects of the IAC procedure, previous studies have proposed the application of DC and LC Beads™ (BTG, United Kingdom) slowly releasing doxorubicin, and Hepatic CHEMOSAT™ delivery system (Delcath Systems, New York, NY) for extracorporeal filtering of the excessive drugs that pass through the liver. The Hepatic CHEMOSAT™ platform creates significant blood flow disturbance in addition to high cost and technical challenges, which has led to safety concerns by the FDA [19, 20]. Therefore, design of the Chemofilter device was proposed for addressing the problem.

1.2.1 Doxorubicin and its Binding Mechanisms

Doxorubicin ($C_{27}H_{29}NO_{11}$) is a cytotoxic antineoplastic antibiotic, isolated from cultures of *Streptomyces caeruleorubidus* bacteria, and is commonly used in the treatment of solid organ cancers [21]. It prevents cell replication by intercalating into the DNA double helix and inhibiting both DNA replication and RNA transcription [22]. Dox is a relatively small particle with a diameter of about 1.5 nm [23], and its diffusion properties vary based on composition (such as encapsulated as opposed to non-encapsulated particles). The low efficiency of this drug in tumor suppression is aggravated by tendencies to self-associate in aqueous solution, and accumulate in healthy organs. Despite all the aforementioned limitations, Dox remains a corner stone drug for cancer treatment due to its potent effect on tumors [22].

Dox is an ionic agent, which can be captured through three distinct mechanisms: ion-exchange [24], DNA binding [15, 17, 25, 26], or magnetic capture [27, 28]. The mechanism of interest in this study is the ion-exchange approach, where a block copolymer PtBS-PEP-PSS-PEP-PtBS coating the surface of the Chemofilter is utilized [24]. Several studies have characterized Dox/resin chemical and thermodynamic properties, mostly dedicated to enhancing the efficacy of DC Beads™ [29-34]. In addition, mathematical and numerical models were developed to elucidate the Dox transport/release mechanism [35-38]. Dox is susceptible to capture by the anionic strong-acid sulfonate groups of the ion-exchange resin, which have high affinity for oppositely charged counter ions.

In the case of the IAC procedure, non-encapsulated *Dox-HCl* is injected into the blood stream [24]. It is known that about 50-85% of Dox resides in plasma [39], which causes elevated concentration of Dox in the near-wall regions devoid of RBC's [40]. Moreover, the diffusion

coefficient of Dox in plasma is about 3 times greater than that of blood, based on Stokes-Einstein relation relationship [41]. Since the electrochemical forces are dominant near the surface, high concentration of Dox in the plasma layer proves beneficial to the binding.

1.2.2 Mechanical Properties of Blood

Depending on a particular problem or vascular territory, blood flow can be modeled as a Newtonian, non-Newtonian, or a multiphase flow. Blood is often modeled as a Newtonian fluid (i.e. the viscosity is a constant and independent of the shear rate) when it is flowing through large vessels (about 500 μm and larger) at shear rates over 100 s^{-1} [42]. However, blood is generally considered to be a non-Newtonian fluid at low shear rates, where its viscosity depends on the rate of shear. Fahraeus and Lindqvist showed that in blood vessels with diameter less than 300 μm, the apparent blood viscosity decreases with decreasing diameter [43]. However, with a further decreasing diameter in the range of 20-100 μm, viscosity starts to increase due to the presence of the cells in the flow [44]. Liepsch *et al.* showed that for the shear rate smaller than 100 s^{-1}, blood flow exhibits non-Newtonian behavior [45]. Cokelet conducted experiments on blood flow through narrow vessels and observed that a peripheral layer of plasma is free of cells while the suspension of RBCs is concentrated at the core [46].

The non-Newtonian behavior of blood in smaller blood vessels (20 μm – 100 μm) with even lower shear rates (<10 s^{-1}) is due to the comparable size of blood cells with the size of the vessels [45, 47, 48]. Since blood is a suspension of particles, one can define its yield stress property due to RBCs aggregation in the absence of shear. Tu and Deville [42] and Scott Blair and Spanner [49] showed that the Herschel-Bulkley (H-B) model, accounting for both shear-thinning and yield stress properties, can be used for the flow at very low shear rates where the yield stress is high and the vessel diameter is less than 0.065 mm [47, 48].

1.2.3 Platelet Activation

In design of endovascular devices, platelet activation and accumulation is particularly concerning and needs to be addressed. The deployment of the Chemofilter can significantly impact local hemodynamics. A stagnant or recirculating flow around the device may increase the risk of blood clotting [50-53]. A computational study of partially occluded IVC filter used for

trapping thromboemboli, suggested that large shear stresses may result in resumption of thrombotic-like behavior around the vein's wall or the acceleration of thrombolysis [52, 54, 55].

Thrombus formation occurs due to activation, adhesion, and accumulation of platelets and fibrin in the blood [56, 57]. Platelet cells circulate in normal blood flow, and are physiologically activated upon injury to the cardiovascular system. Mechanistically, platelet activation and accumulation is hypothesized to be initiated by changes in hemodynamic shear stress, leading to increased levels of pro-coagulant biomolecules [58-60]. Once activated, platelets change shape and aggregate, and eventually accumulate near the site of injury [57]. Previous studies suggested various models for platelet activation: 1) levels of platelet activation, determined by summation of shear stress and exposure time [61], 2) damage accumulation due to shear stresses [62], and 3) combining damage accumulation and platelet sensitization from previous exposure [63]. In general, studies showed that increased shear stress and exposure time produced higher levels of platelet activation [60, 64, 65]. It is important to note that the platelet activation can be found at both high shear stress levels greater than 7.5 Pa, or at very low shear stress, less than 0.3 Pa. At low shear stress levels, the residence time increases and the activated platelets can accumulate.

1.2.4 Chemofilter Surface Design

Besides the configuration of the Chemofilter, the surface texture can be designed to improve the hemodynamics and binding performance. In order to further reduce the drag force and facilitate blood flow, biomimetic approaches can be applied to the chemofilter design. Biomimetics (also called "bionics" or "biomimicry") is the application of methods found in living nature to the study and design of engineering systems and modern technology. The human-made materials, such as steel, typically require high temperatures and pressures to produce. Instead, materials in living nature typically have a composite structure and hierarchical organization [66]. Such organization provides flexibility needed to adapt to changing environment. Furthermore, the hierarchical organization provides a natural mechanism for the repair or healing of minor damage in the material thus leading to the new field of self-healing materials [67].

Kim *et al.* studied the relation between the water contact angle and thrombus deposition applying the multiscale lotus effect on the surface and observed the decrease in the platelet

adhesion with increase of the hydrophobicity [68]. Chen *et al.* mimicked the inner cell layer topography of the real blood vessel tissue with submicron ridges and nano-scale proturbances to reduce the platelet adhesion to the surface and concluded that the best results are obtained using the multiscale surface [69]. Liu *et al.* designed a surface with microscale longitudinal aligned grafts and observed a reduced thrombus formation on the textured surface compared to that on the smooth one [70]. In a study of the shark-skin effect on the biofilm formation leading to blood clotting, Chung *et al.* designed riblets with a microtopography of 2 μm width, 3 μm spacing and various height for their *in vitro* experiment on the *S. aureus,* a bacterial pathogen. The biofilm colonies started forming on the modified surface after day 21 while on the smooth surface the biofilm was formed at day 7 and matured at day 14 [71].

In the biomimetic surfaces with the shark-skin effect, the surface is covered with micro-riblets positioned parallel to the flow, similar to those in the shark-skin scales. The shark-skin effect leads to a reduction in drag resistance; a report by Bechert *et al.* found the reduction up to 9.9 percent [72]. Viscous drag is the measure of the energy required to transfer momentum between the fluid and surface, as well as the layers of the fluid flowing relative to each other due to velocity gradients. The bursting and translation of vortices out of the viscous sublayer in the near-wall region, their collision and ejection and the chaotic flow in the outer layers are various types of momentum transfer that contribute to the flow drag. However, having riblets on the surface causes the latter vortices to form and remain above the riblets, thus introducing the zones of low velocity fluctuation in the valleys between riblets. Therefore, the high velocity vortices only interact with the small area at the tips of the riblets, counteracting the drag due to the addition of the riblets, which results in the overall drag reduction [73-75]. The shark-skin effect is well known for water flow; however, here we propose to apply a similar effect on the Chemofilter surface, introducing a "hemophobic" surface (blood repelling, similar to the hydrophobicity or oleophobicity).

1.3 Summary of Chapters

The computational optimization of the Chemofilter design is a multifaceted project which is explored throughout this dissertation. In **Chapter 2:** *"A two-scale approach for CFD modeling of endovascular Chemofilter device",* design and hemodynamic performance of the

porous Chemofilter Basket, is presented. Chemofilter basket consists of architected material (a matrix of tessellated microscale unit-cells) that forms an umbrella-shaped basket. The membrane is installed on a self-expanding nitinol frame, to be placed in a catheter for deployment. Simulations resolving the microscale structure of the device were carried out to determine the permeability of the microcell membrane. The resulting permeability coefficient was used for macroscale simulations of the flow through the device modeled as a porous material. CFD-predicted flow metrics were evaluated to minimize flow obstruction and thrombosis while providing sufficient binding surface. This chapter is adapted from a publication in "Journal of Biomechanics and Mechanobiology" [76].

In **Chapter 3:** "*Computational modeling of drug transport and mixing in the chemofilter device: enhancing the removal of chemotherapeutics from circulation"*, transport and binding performance of two alternative non-porous Chemofilter configurations, the honeycomb and the strutted Chemofilters, is presented. The honeycomb configuration was developed and optimized with CFD modeling, where the geometry modifications were intended to increase the flow mixing and residence time. The strutted prototype was loaded with ion-exchange resins and used in the porcine *in vivo* studies to examine the electrochemical adsorption of Dox to the Chemofilter surface. A comparative multiphysics study was conducted to computationally evaluate the performance of these configurations, utilizing the heat/mass transfer analogy. The results obtained with modeling were compared with the experimental results from animal studies [24]. This chapter is adapted from the manuscript under review submitted to the "Journal of Biomechanics and Mechanobiology"[77].

Chapter 4: "*Electrochemistry of Doxorubicin binding to the ion-exchange resin: an effective diffusion coefficient to account for ionic migration",* investigates the transport and binding of Dox with different electrochemical models. The material balance equation was derived based on dilute and concentrated solution theory. In these equations, an effective diffusion coefficient is introduced which includes the contribution of both the ionic migration and molecular diffusion. The effective diffusion coefficient, derived with the dilute solution assumptions, was then integrated into the CFD model to predict the overall Dox elimination from the venal flow. The concentrated solution assumption is more generally valid for expressing the binding efficacy, however only an approximate value of the resulting effective diffusion was incorporated in the CFD models due to the lack of experimental results. These simulations were

conducted on different Chemofilter configurations, discussed in Chapter 2 and 3, and their performance was compared with one another as well as the *in vivo* results. This chapter is adapted from the manuscript to be submitted to the Journal of Electrochemical Society [78].

Another facet of the Chemofilter project is the surface design, explored in **Chapter 5:** "*The shark-skin effect on platelet activation, hemodynamic and drug binding performance of the Chemofilter: from hydrophobicity to 'haemophobicity'"*. The shark-skin effect is an application of biomimetic surface texturing for reducing the drag force and facilitating the flow. For application of shark-skin effect, the surface was covered with riblets, aligned parallel to the flow. CFD simulations of the flow on a textured surface of a rectangular microchannel and a cylindrical tube were conducted to assess the effect of the riblets on wall shear stress and platelet activation. These results were then used to apply surface texture to the channels in the honeycomb Chemofilter in order to assess the improvement in its binding performance. This chapter is partially adapted from the published works [79, 80].

Finally, in **Chapter 6: "***Conclusion"* the overall achievements in my PhD research and its impact are summarized.

.

CHAPTER 2. A TWO-SCALE APPROACH FOR CFD MODELING OF ENDOVASCULAR CHEMOFILTER DEVICE

2.1 Introduction

In this study, we assess the hemodynamic performance of a Chemofilter membrane manufactured from micro-scale architected materials. Current Chemofilter prototypes range from mesh bags to macro-porous strutted membranes, which are difficult to manipulate and optimize to improve hemodynamic performance. Microscale architected materials present a possible alternative as they can be fabricated in any arbitrary size and shape. As shown in Figure 2-1, the Chemofilter consists of a matrix of microscale unit-cells (microcells) that connect to each other in layers to form an umbrella-shaped porous membrane. The membrane is installed on a self-expanding nitinol frame, which is placed in a catheter for deployment. The hemodynamic performance of the proposed device is evaluated with Computational Fluid Dynamics (CFD) in order to optimize the design of the Chemofilter microstructure as well as the overall shape of the device.

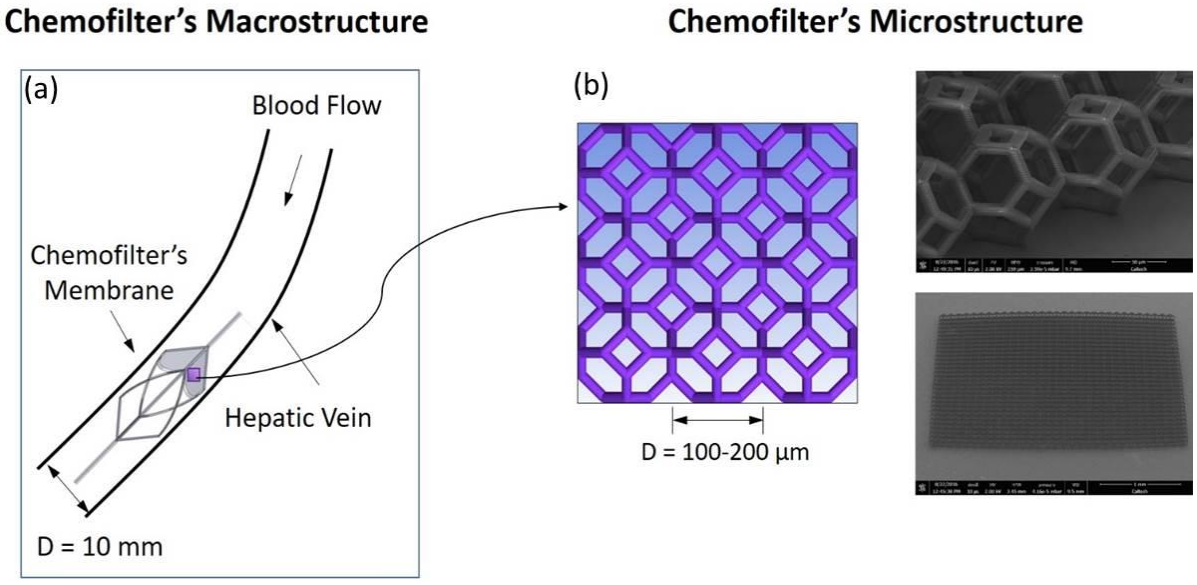

Figure 2-1 The multiscale approach for modeling the Chemofilter (a) the schematic of the device deployed in the hepatic vein (b) The schematic and SEM image of a matrix of microcells

2.2 Methods

In this study, various porous configurations of the prototype Chemofilter device are considered in order to evaluate their hemodynamic performance. The flow proximal to the deployed Chemofilter will be retarded, thus facilitating drug binding to the device. At the same time, reducing flow stagnation regions around the filter is crucial for preventing thrombus formation. Thus, the Chemofilter design should be aimed at providing sufficient surface for the chemical binding of the drugs, while minimizing flow obstruction. Since the vein diameter, approximately 10 mm, is 2 orders of magnitude larger than the size of a 100-micron micro-cell, a multiscale approach is used to model the flow through the Chemofilter. In this approach, the flow through a representative matrix of the micro-cells is resolved in order to determine the permeability of the lattice. The obtained values are then used to simulate the flow through the whole device modeled as a porous membrane. Darcy's law is applied to calculate the porous characteristics of the membrane. By computing the pressure on both sides of the lattice comprising the Chemofilter's membrane, the permeability tensor $\overrightarrow{\overrightarrow{\boldsymbol{K}}}$ (m^2) is calculated as:

$$\vec{q} = -\frac{\overrightarrow{\overrightarrow{\boldsymbol{K}}}}{\mu}.\vec{\nabla}P \tag{2-1}$$

where $\vec{q}$ is the blood flux per unit area (m/s), μ is the blood viscosity, and $\vec{\nabla}P$ is the pressure gradient. The components of the permeability tensor were determined by carrying out CFD simulations for different orientation of the membrane relative to the flow, as characterized by the angle (α). Porosity is defined as the average volume of the pores divided by the total volume:

$$\boldsymbol{\varepsilon} = \frac{\boldsymbol{V_p}}{\boldsymbol{V}} = \frac{\mathbf{1}}{\boldsymbol{V}}\int_{\boldsymbol{V_p}} \boldsymbol{dV} \tag{2-2}$$

Idealized models of the Chemofilter and a representative segment of the microcell lattice were generated using SolidWorks (Dassault Systems) software. In designing these microcells, the following principles were used to enhance the fluid flow: a) the microcells are tessellated in order to fill the space in 3D, b) a hollow space within the microcell minimizes potential disruption of the flow, and c) the surface area is high relative to the enclosed volume. With these three features in mind, an open cell tetrakaidecahedron was chosen as the initial unit cell candidate for this study.

2.2.1 CFD Modeling

A multiscale modeling approach was used for the analysis of blood flow through the Chemofilter. In this approach, a detailed numerical simulation was carried out for the flow through a matrix of 2x2 microcells with periodic boundary conditions (BC) on the walls in order to determine the flow resistance of the whole membrane. The unstructured mesh with prism layers around the micro-trusses was generated using ANSYS ICEM software. In order to ensure that the mesh elements at the periodic boundaries are identical, one quarter of the domain was initially meshed and the volume mesh was then mirrored in both directions to provide conformity of elements on the walls. The simulations of blood flow through the microcell matrix were conducted to characterize the performance of the lattice with different microcell sizes (ranging from 100 to 200μm), number of microcell layers (from 1 to 3), and different membrane orientations relative to the flow. Consequently, the porosity and permeability of the microcell matrix was obtained and the whole Chemofilter device was modeled as a porous membrane without resolving the individual cells. To ensure that the 2x2 microcell matrix could adequately represent the membrane, the results were compared with those obtained in simulation for a 4x4 microcell matrix. In addition, a mesh size sensitivity analysis was conducted to ensure sufficient resolution of the boundary layer formed around the micro-trusses. Increasing the number of computational elements from 2 to 8 million (1 layer of 2x2 microcell matrix simulation) resulted in less than 10% change of the calculated pressure drop across the microcell lattice.

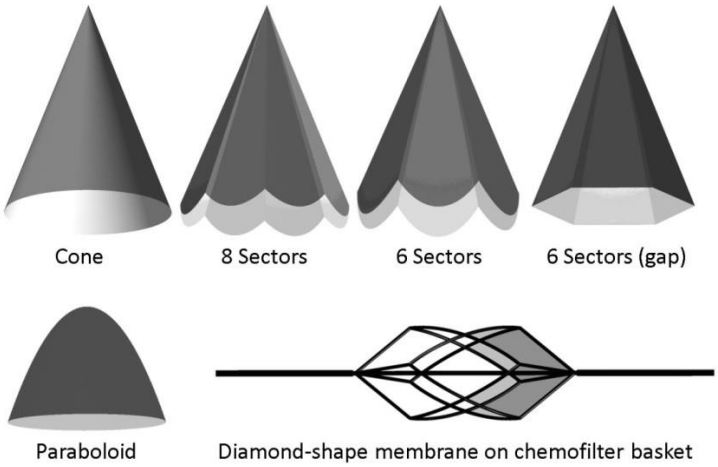

Figure 2-2 Different configurations of the Chemofilter's membrane. The membrane may consist of 1 to 3 layers of microcells with 100 to 300 μm diameter. The angle of idealized umbrella-shaped membrane varies between 22º to 60º

In the macroscale model, the idealized membrane was modeled as a canopy that fits the blood vessel's cross section. Various configurations of the porous membrane resembled an umbrella, as shown in Figure 2-2. In order to evaluate the flow for an umbrella-shaped device, the membranes with 6 and 8 sectors were modeled. The hemodynamic performance of the membranes with different opening angles (tip angle), thicknesses, and shapes were compared. A model where the umbrella sectors were extended all the way to the vessel wall, thus forming petal-shaped flat surface canopies, was compared to that with a gap formed between the triangular canopy sectors and the vessel. Once the flow through the umbrella-shaped membrane was characterized, a porous membrane installed on a supporting nitinol frame, analogous in shape to the RX Accunet embolic protection device (Abbott Labs), was modeled. In this configuration of the Chemofilter, the membrane covered the 4 diamond-shaped sectors of the structure (Figure 2-2). The macroscale geometry was also meshed in ICEM CFD (ANSYS) software. A hybrid meshing was used to resolve the flow around the device by increasing the number of elements in proximity to the porous membrane, with a gradual increase of the element size farther away from the filter. The mesh density was adjusted in order to control the mesh growth size in the flow regions adjacent to the filter. In order to reduce computational time by using the symmetric geometry of the umbrella-shaped device, one sector of the membrane, i.e. one quarter of the domain, was modeled and symmetry boundary conditions were applied on the side walls.

In the simulations of the whole device, the hepatic vein was modeled as a straight rigid tube with 10 mm diameter. The section of the tube proximal to the device was sufficiently long to ensure the flow becomes fully developed before reaching the Chemofilter. Blood was modeled as a Newtonian, homogeneous fluid with the constant density and dynamic viscosity of $\rho = 1060$ kg/m^3 and $\mu = 0.0035$ kg/m·s respectively. The Navier-Stokes equation was solved with a finite-volume solver, Fluent (ANSYS), using a Coupled scheme for velocity-pressure coupling. A second-order and third-order MUSCL schemes were used for the pressure and momentum spatial discretization respectively. The flow was modeled as steady due to a negligible effect of the heart pulse in the hepatic vein, and the relatively low Reynolds number (Re = 300) ensured the flow remained laminar. The inlet velocity was set to 0.1 m/s and the outflow boundary condition was assigned to the outlet.

2.3 Results

The Chemofilter deployment results in a pressure drop across the porous membrane and formation of a flow disturbance region around the device. The CFD simulations conducted for different configurations of the Chemofilter's membrane demonstrated the effect of device geometry on the resulting flow fields.

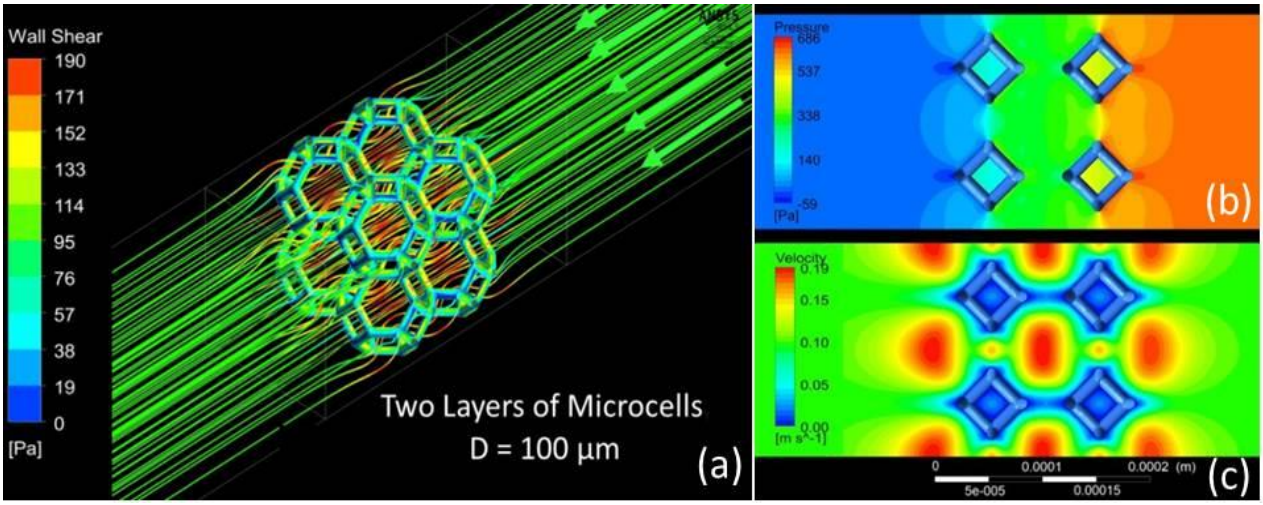

Figure 2-3 (a) Flow streamlines and shear stress distribution for a 2x2 microcell matrix (b) Pressure and (c) Velocity contours calculated for the flow through two layers of 2x2 matrix with 100 µm microcells

2.3.1 Microstructure Model

Figure 2-3 shows the flow through a segment of the lattice, characterized by the accelerated flow through the microcells and higher shear stress on the front face of the micro-trusses. For a two-layer matrix of 2x2 microcells with 100µm size, the pressure drop was about 600 Pa across the membrane. The comparison of the lattices made of 2x2 and 4x4 matrix showed a 3% difference in the pressure drop, with the higher value for the 2x2 matrix. Since the difference was negligible, the rest of the microscale simulations were carried out for the 2x2 matrix. The parametric studies were conducted to determine the dependence of the pressure drop across the membrane on the size and thickness of the lattice. The microcell diameter ranged between 100 and 200 µm and the lattice consisted of 1, 2, and 3 layers of the cells. Figure 2-4 indicates that increasing the microcell size resulted in a smaller pressure drop for the same

number of layers. Increasing the number of layers of identical size microcells resulted in increase in the pressure drop across the membrane.

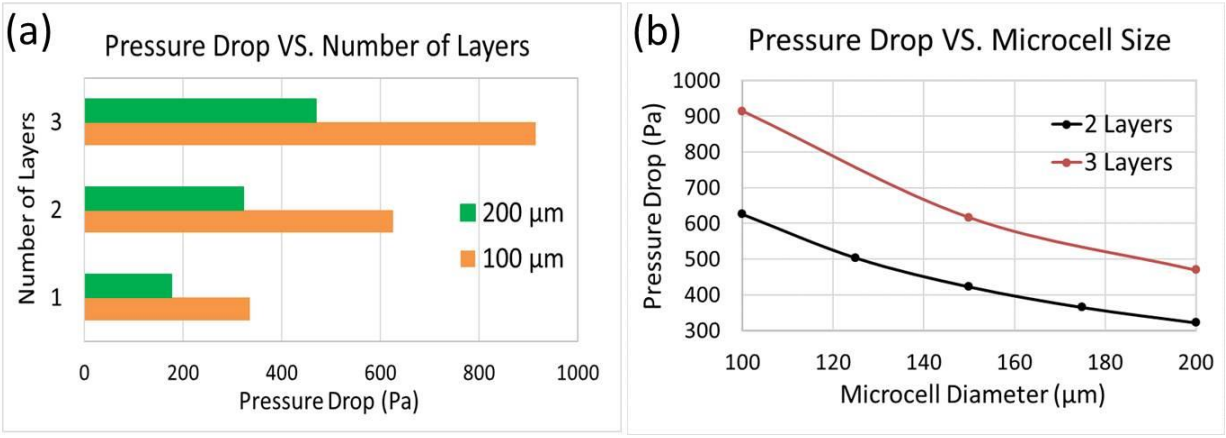

Figure 2-4 The effect of the microcell size and number of layers on the pressure drop across the membrane

To calculate the permeability tensor, the simulations were run for various angles of the lattice with respect to the flow. Figure 2-5(a) shows the schematic of the Chemofilter, and Figure 2-5(b) shows the flow as it approaches the lattice at an angle of $\alpha = 30^{o}$, but leaves it normal to the lattice surface. The results suggested an isotropic behavior of Chemofilter:

$$\overrightarrow{\overrightarrow{\boldsymbol{K}}} = \begin{Bmatrix} K & 0 & 0 \\ 0 & K & 0 \\ 0 & 0 & K \end{Bmatrix}$$

The membrane's porosity is $\varepsilon = 0.92$ and permeability of the membrane is depicted in Figure 2-6(d).

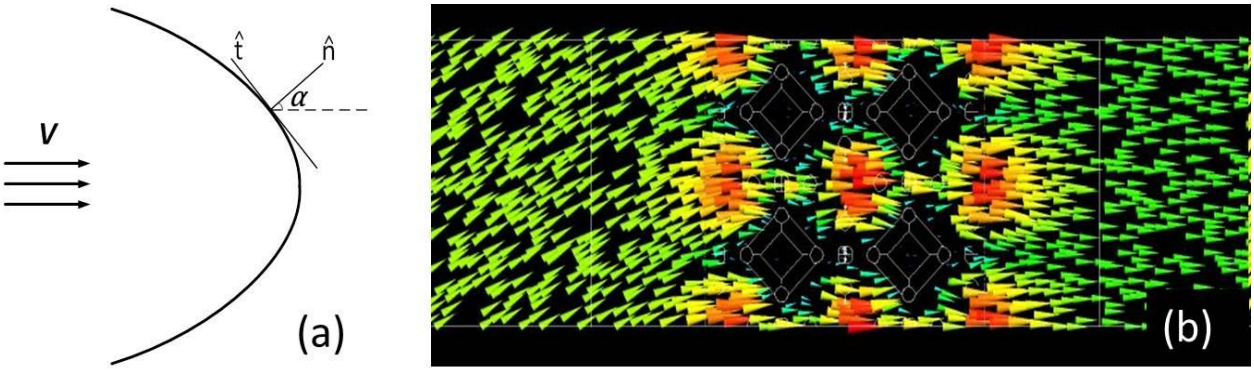

Figure 2-5 (a) Schematics of the Chemofilter geometry with an arbitrary angle α, (b) velocity vectors around the lattice with α = 30º

2.3.2 Macrostructure Model

The umbrella-shaped membrane was considered as the primary Chemofilter geometry. Figure 2-2 demonstrates the schematics of various device configurations, including a membrane forming a cone, a membrane made of 6 or 8 sectors extending to the vessel wall, a membrane shaped out of 6 triangular sectors with a gap near the wall, the paraboloid, and a diamond-shape membrane installed on the nitinol frame structure.

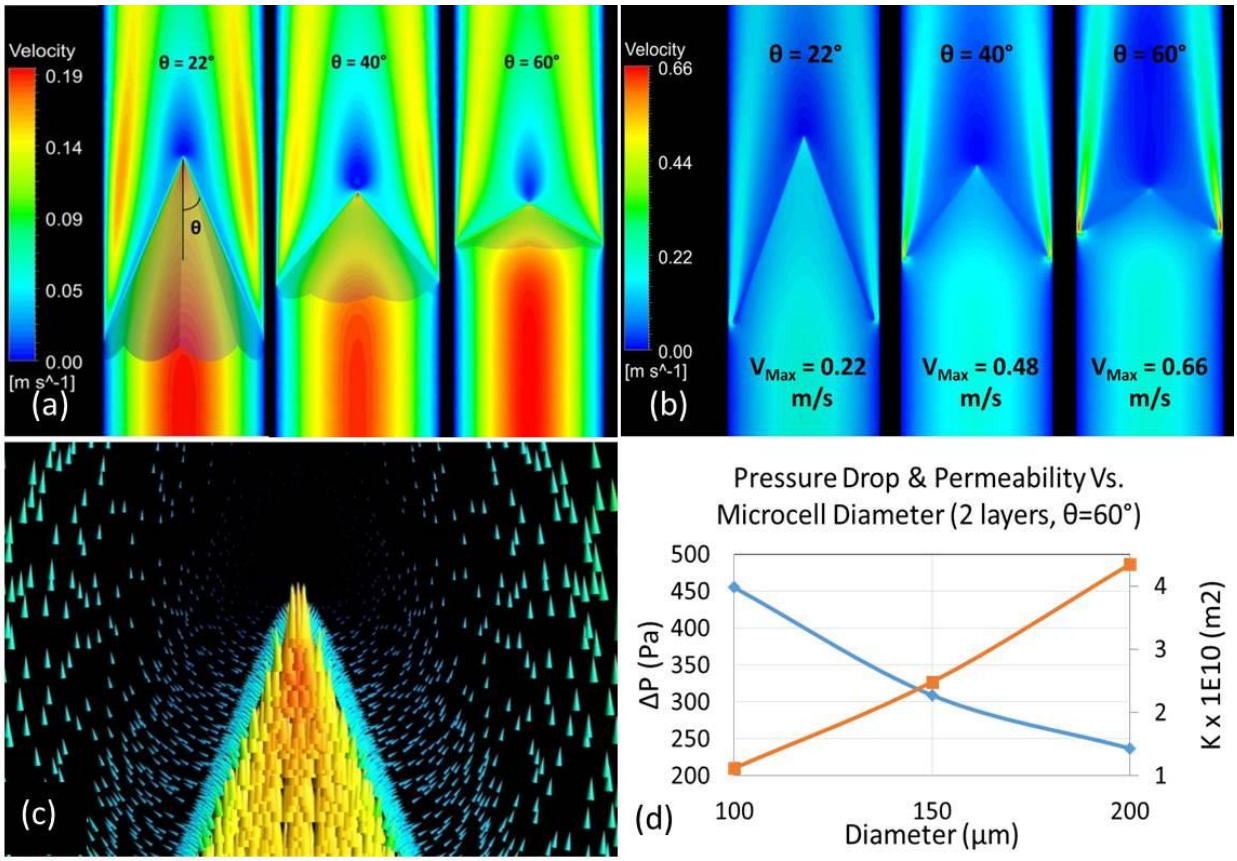

Figure 2-6 Velocity contours for an umbrella-shaped Chemofilter with different tip angle θ (a) extended all the way to the wall (b) with a gap; (c) Velocity vectors around the membrane's tip for 2 layers of 100 μm cells; (d) The effect of microcell diameter on the overall membrane's permeability and pressure drop

Figure 2-6 demonstrates the effect of the tip angle on the flow through the membrane consisting of 8 petal-like sectors. The geometries with the angles of 22º, 40º, and 60º were modeled. The velocity contours in Figure 2-6 (a) show the formation of a high velocity jet between the membrane and the vessel wall and a stagnant flow downstream of the membrane's tip. A gap may form between the sectors of the membrane and the vessel wall either because of the non-circular shape of the sectors or because of the imperfect placement of the device. Figure 2-6 (b) shows that the maximum velocity of the flow escaping the membrane through the gap increases for larger tip angles. Consequently, a greater fraction of the blood can bypass the Chemofilter. Figure 2-6 (d) shows that the pressure drop decreases with increasing the microcell size, as the membrane's permeability increases.

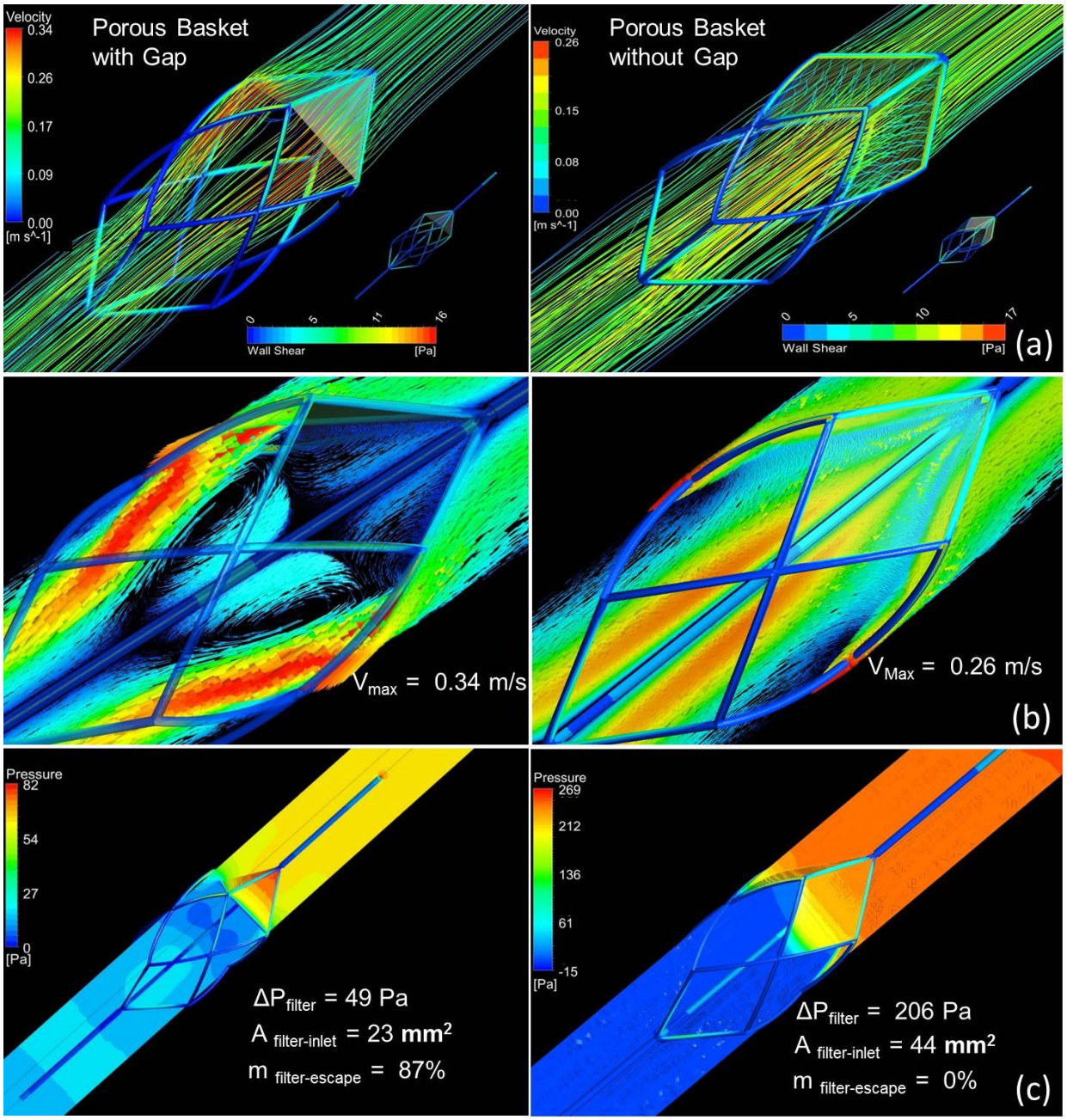

Figure 2-7 (a) Flow streamlines passing through the filter and shear stress on the Chemofilter basket structure (b) Velocity vectors and (c) Pressure distribution on the mid-plane parallel to the flow

The hemodynamic performance of different membrane configurations is shown in Table 2-1. The pressure drop decreases if the number of the membrane sectors is reduced. For smaller tip angles, the pressure drop decreases, while the membrane area increases. The gap area and, consequently, the mass flow rate escaping through the gap for the 6- sector configuration is larger than that of the 8-sector one.

Table 2-1 Comparison of hemodynamic performance of different membrane shapes (2 layers of 100μm microcells)

2 layers of microcells (D = 100 μm)	Membrane's tip angle θ	Without gap		With gap		
		ΔP (Pa)	Area (m^2)	ΔP (Pa)	Escaped blood flow	Surface area (gap/membrane)
cone	22º	94	$1.095x10^{-3}$	---	---	---
6 petal	22º	74	$1.238x10^{-3}$	66	28%	21%
8 petal	22º	79	$1.171x10^{-3}$	79	12%	11%
	40 º	237	$0.691x10^{-3}$	185	24%	10%
	60 º	455	$0.497x10^{-3}$	293	36%	10%

2.3.3 Chemofilter Basket Design

Figure 2-7 depicts the velocity vectors and pressure and shear contours obtained for the Chemofilter designed as an embolic protection device basket covered by a porous membrane. The lattice consisting of 2 layers of the 150 μm microcells, with the tip angle of 40º, and 4 sectors was chosen for the simulation of the membrane installed on the structure. The case where the sectors of the canopy have a flat triangular shape, thus causing a gap between the filter and the wall, is compared with the case where the membrane is extended to cover the gap. The blood escaping through the filter leads to a larger flow recirculation region with the maximum velocity of 0.34 m/s for the case with the gap compared to 0.26 m/s for the fully covered frame. The pressure drop across the triangular membrane decreases to about a quarter of that computed for the fully covered design, while the triangular membrane's surface area is a half of the fully covered one.

2.4 Discussion

Blood flow through the Chemofilter device is studied with multiscale CFD simulations that resolve the flow through a lattice of microcells as well as model the flow across the filter's porous membrane. The non-Newtonian blood behavior was neglected because the size of the vessel is much larger than the size of red blood cells and the shear rates around the microtrusses

are larger than 100 s^{-1}[42]. In the microscale models, the pressure drop is directly proportional to the number of the membrane's layers while it is inversely proportional to the microcell size. For example, the pressure drop for the 3 layers of 150 μm microcells is about the same as that of the 2 layers of 100 μm microcells, while the overall thickness of the membrane is 2.25 times larger for the former. The larger microcell size allows an easy passage of blood cells through the membrane due to its lower resistance. However, more Dox particles are likely to escape through the filters with larger microcell size and smaller number of layers, which lowers the amount of drug bound to the filter.

Examining the lattice orientation relative to the flow, the components of the permeability tensor were calculated and the membrane porous structure was found to be isotropic. The isotropic behavior of the lattice is due to the symmetric geometry of microcells and their repeating arrangement in the lattice. The detailed view of the flow near the tip shown on Figure 2-5 and Figure 2-6(c), confirms that filtered blood exits the membrane normal to its surface, regardless of the entrance angle.

By calculating the pressure drop across the lattice, the porous characteristics of the Chemofilter were determined and used to evaluate the design of the membrane's overall shape. The optimal geometry would minimize the pressure drop and reduce flow disturbance, while maximizing the surface area and flow residence time around the membrane in order to facilitate drug absorption. Therefore, different geometries were considered to study the effectiveness of the device, while avoiding the risk of blood clotting.

The study of the idealized umbrella-shaped membrane (Figure 2-2, and Figure 2-6), indicates that a lower number of the membrane's sectors, acute tip angles, and larger microcell size result in decreased pressure drop. However, chemical binding may be negatively affected by the latter parameters. The greater pressure drop across the membrane with larger number of sectors is due to the increase in the overall membrane surface area, as well as the discontinuity of the geometry at the intersection of sector's canopy. The membrane with smaller tip angle causes less obstruction to the flow as it reaches the filter, resulting in lower pressure drop.

The design of a Chemofilter basket porous membrane was guided by the results obtained from studying the idealized umbrella-shaped prototypes. A 4-sector membrane with the tip angle of 40º is installed on the nitinol struts forming the basket. The lattice has 2 layers of 150 μm microcells to provide relatively large contact area and low resistance to the flow. The fully

developed flow, upon reaching the filter, uniformly exits the filter's membrane normal to its surface. On the downstream side of the Chemofilter, the high velocity jet is formed closer to the vessel wall, while a stagnant area is developed around the tip of the device due to the sharp angle of the membrane. The gap amplifies the jet velocity, as it provides a low resistance passage where the flow can escape unfiltered. The overall configuration of the device allows a moderate pressure drop and flow separation region. The results show that a gap in the Chemofilter basket design results in 87% of flow bypassing the filter, besides reducing the surface area. Therefore, the extended membrane's canopy, which provides both mechanical strength and larger contact area, is preferred in this design. The curved extending part of the membrane forms a narrow space between the membrane and the wall, where the maximum velocity is found in the domain. Blood flow through the flat umbrella-shaped filter was also compared with that of a paraboloid-shaped prototype to examine the membrane's tip effect (see Figure 2-2). For the paraboloid membrane, the sharp tip that caused flow disturbance for the umbrella design was avoided. By allowing a smooth transition between the high velocity jet and mainstream flow, the area of stagnant flow behind the tip was reduced.

2.5 Limitations and Future Work

The slow flow through a porous membrane as well as in the stagnant regions downstream of the membrane may result in thrombus deposition. Since the Chemofilter is temporarily deployed during a 30-60 minutes chemotherapy session, the risk of thrombus formation can be minimized by administering a high dosage of heparin during the procedure.

One of the limitations of this study is the assumption of a rigid vessel wall, as the vein's compliance may cause a gap near the edges of the Chemodilter, thus leading to a leakage of unfiltered blood at the periphery of the device. In addition, the apposition of the device can be imperfect, also resulting in a leakage of Dox through the gaps between the device membrane and the vessel.

Computational modeling of the Chemofilter is used for optimizing the device's configuration and guiding the design of in-vitro experiments and animal studies. The clinicians still debate whether the device will be deployed in the hepatic vein or IVC. Therefore, approximate numbers for the vein's diameter and average velocity, suggested by clinicians, were chosen, matching the order of magnitude of the *in vivo* parameters. Since the study is evaluating

the relative advantages of the alternative designs, the results are useful as long as the Reynolds number and flow conditions remain the same across the CFD simulations.

This work presents an initial study that aims at developing a two-scale CFD model of the Chemofilter device. The model will be expanded to include chemical binding of the drugs to the membrane's surface. The multi-scale approach will be applied to first evaluate the drug binding to the individual microcells, and consequently determine the change of the drug concentration for the flow through the porous membrane. The effect of the membrane's elasticity will also be assessed in the future analysis. The Chemofilter design can benefit from increasing surface area which provides more binding sites. Using the architected material porous membrane allows to increase the surface area of the device as well as to enhance flow mixing. In addition, a lower Peclet number, defined as the ratio of the diffusion and advection time scales, can improve the filtration efficiency by providing sufficient time for the Dox particles to bind to the filter's surface. The optimum design of the Chemofilter will therefore provide sufficient surface area and reaction time for the Dox binding.

2.6 Conclusion

The multiscale CFD simulations were used to evaluate hemodynamic performance of the Chemofilter membrane. The size of the microcells composing the porous membrane should allow for unobstructed passage of blood components, while it should be small enough to ensure sufficient adsorption of toxins and prevent their escape through the pores. A larger number of the microcell layers can provide adequate residence time and drug binding sites for filtration. The more acute tip angle of the membrane also results in a larger contact area for drug binding. However, the sharp tip angle should be avoided to reduce flow separation downstream of the filter. In general, a larger area of the filter causes more resistance to the flow, which consequently leads to larger pressure drop. A gap between the device and the vein's wall reduces the efficiency of the filtration. Thus, extending the membrane's canopy to cover more area of the Chemofilter frame structure will reduce the gap, while providing mechanical strength and larger surface area.

CHAPTER 3. COMPUTATIONAL MODELING OF DRUG TRANSPORT AND MIXING IN THE CHEMOFILTER DEVICE: ENHANCING THE REMOVAL OF CHEMOTHERAPEUTICS FROM CIRCULATION

3.1 Introduction

In the current study, which is a continuation of Chapter 2, Maani *et al.* [76], two alternative, non-porous Chemofilter design, the *honeycomb* and *strutted* configurations, are optimized with computational fluid dynamics (CFD) simulations to maximize drug binding while minimizing the pressure drop and flow obstruction. The flow channels of the non-porous prototypes are an order of magnitude larger than those of the porous membrane. This disparity results in different ranges of surface area, residence time, and mixing. A comparative study was performed for evaluating different configurations utilizing an analogy between heat and mass transport mechanisms. The results obtained with this multi-physics modeling approach were compared with experimental results obtained in animal studies [24].

3.2 Methods

In order to evaluate and compare the performance of different Chemofilter configurations, numerical simulations were conducted and results were compared with that of the *in vivo* porcine studies reported in Oh *et al.* [24]. The computational studies were conducted on two different configurations of the Chemofilter with a non-porous membrane: the *honeycomb* Chemofilter and the *strutted* Chemofilter. The strutted Chemofilter, used previously in experimental studies [24], consists of a uniform cubic lattice of struts as shown in Figure 3-1 (b). The honeycomb Chemofilter, developed in computational studies, Figure 3-1 (c), consists of parallel hexagonal channels which resemble the natural honeycomb. In the original, “plain" honeycomb design, hexagonal channels are aligned with the direction of blood flow. The upstream flow divides between the honeycomb’s cylindrical channels where Dox particles bind to the coated surfaces. In order to further enhance drug adsorption, the honeycomb channels can be a) perforated to allow flow mixing between the channels, and b) twisted to disrupt boundary layer formation in the channels Figure 3-1 (c).

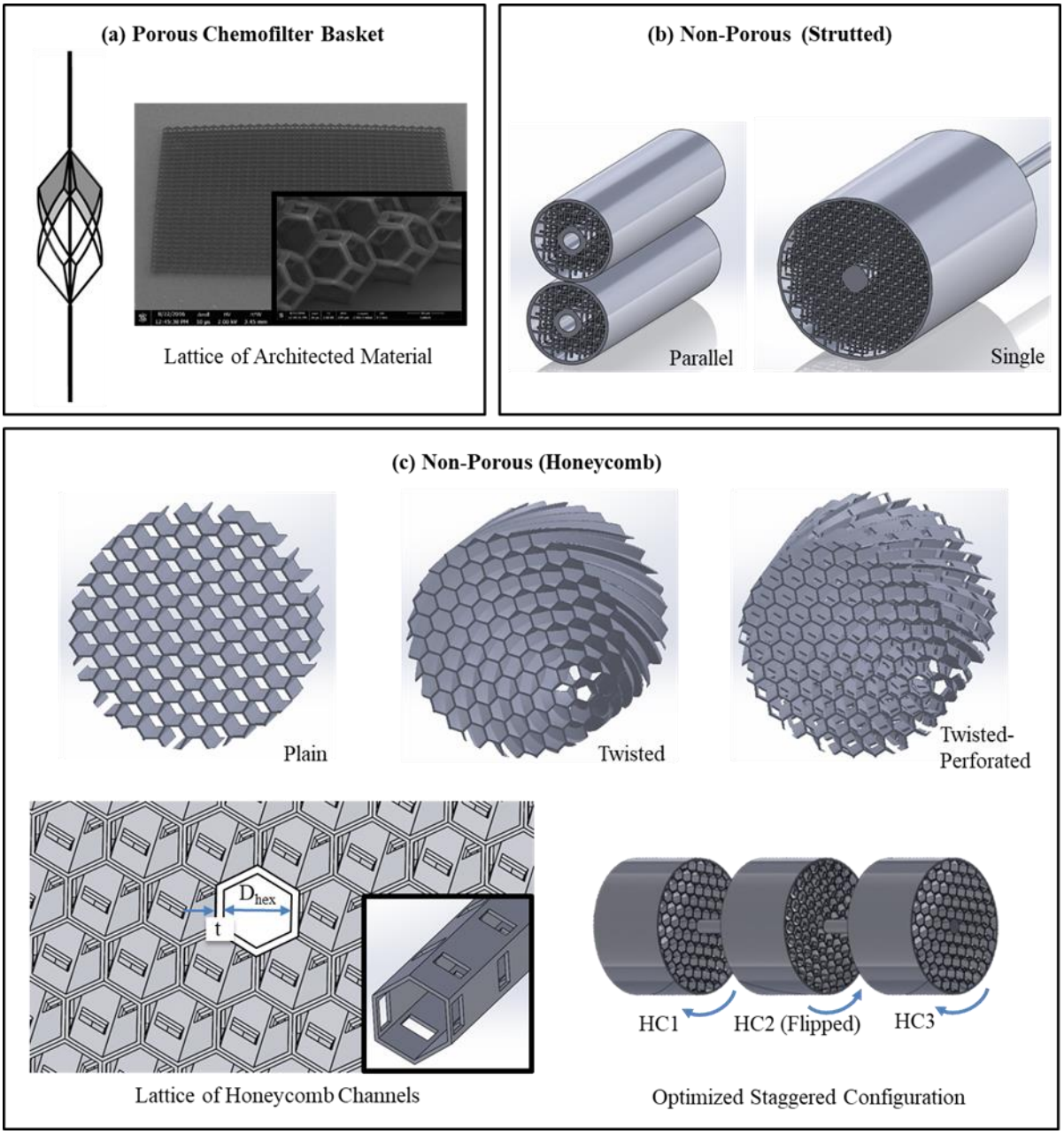

Figure 3-1 Chemofilter device configurations include (a) the porous Chemofilter basket [76], (b) the non-porous strutted Chemofilter (tested experimentally [24]), and (c) the non-porous honeycomb Chemofilter (developed in this study).

3.2.1 Heat Transfer Analogy

In this study, the analogy between the mass and heat transfer was utilized as a simple and tangible method for comparing the performance of different honeycomb configurations. In order to use this analogy, the Schmidt number (Sc), i.e. the ratio of momentum and mass diffusivity,

and the Prandtl number (Pr), i.e. the ratio of momentum and heat diffusivity, were matched. The Peclet number (Pe), expressing the ratio of diffusion time to advection time was also matched in both systems by setting the thermal diffusion coefficient equal to the mass transport diffusion coefficient. The flow conditions were identical for both models, thus maintaining the same velocity boundary layers. We note that in the above analogy, only the passive diffusion of species was considered.

3.3 CFD Modeling

For the CFD simulations of the Chemofilter, the geometry was generated in SolidWorks (SolidWorks Corp., Dassault Systèmes) software. To generate the flow domain in SolidWorks, the device was modeled in a straight tube, long enough to ensure fully developed flow upstream of the filter and prevent reversed flow at the outlet. The CAD file was then imported to ANSYS ICEM (ANSYS, Inc.) for discretization and meshing. The mesh density around the Chemofilter was increased to achieve a minimum length of 0.02- 0.05mm, in order to ensure adequate flow resolution within individual channels. Mesh independence of the numerical solution was confirmed for all configurations with negligible discrepancies in temperature and pressure drop (< 3 %) by varying the number of elements around the Chemofilter by a factor of two. The discretized geometry was imported to ANSYS Fluent for numerical solution, and the results were processed using ANSYS CFD-Post software.

The coupled Navier-Stokes and Advection-Diffusion-Reaction equations were solved with a finite-volume solver, ANSYS Fluent. A second-order scheme was used for pressure and third-order MUSCL schemes were used for momentum, energy, and species transport spatial discretization. The flow was modeled as steady due to the negligible effect of the cardiac pulse in the hepatic vein, and the Reynolds number is low enough (Re = 300) for the flow to remain laminar. The inlet velocity was set to 0.1 m/s and the outflow boundary condition was assigned to the outlet. To model Dox binding to the Chemofilter, the energy and species transport were activated in Fluent. In the simulations with heat transfer analogy, only the energy equation was activated.

3.3.1 Parameter Characterization and Sensitivity Analysis

In order to find the optimal honeycomb configuration, the sensitivity of the model to the various geometry and transport parameters was investigated. The following parameters were studied as presented in Table 3-1: (1) diameter of hexagonal channels, (2) twist angle of the channels, (3) length of the honeycomb channels, (4) spacing of multiple honeycomb sections in series, (5) inlet velocity, and (6) thermal diffusion coefficient. The other boundary conditions and the vessel geometry remained the same in all simulations. The diameter of hexagonal channels was varied from 0.45 to 0.90 mm to identify the benefit of decreasing the diameter on drug adsorption. The twist angle of the channels was varied from 0^0 for the plain honeycomb to 45^0 (equal to helix angle of 84^0) and the honeycomb length was varied between 5.8 mm and 20 mm. In the staged configuration, the sensitivity of the results to the spacing between honeycomb sections was investigated by varying the spacing between 1.3 mm to 11.6 mm (staged configuration in Figure 3-1). The inlet velocity was varied from 0.01 to 0.10 m/s to represent porcine and human venous hepatic blood flow velocity, respectively. The diffusion coefficient of Dox in blood was varied from 10^{-7} to 10^{-10} m^2/s to compare the effect of active diffusion by the ion-exchange resin to passive diffusion. To evaluate the sensitivity of the results to design parameters and intrinsic properties (the diameter of hexagonal channel, the inlet velocity, and diffusion coefficient), the Cotter's method for sensitivity analysis was utilized [81]. Since the channel diameter range was varied by a factor of two and the velocity range was varied one order of magnitude, the diffusion coefficient range was also limited to one order of magnitude (diffusion coefficient of 10^{-9} m^2/s used as the upper bound) in the Cotter's sensitivity analysis, to maintain comparable effect of these variables on the results.

Using SolidWorks, hexagons were constructed with an apothem length of 0.50 mm and a corresponding edge length of 0.58 mm to construct the configuration with 0.90 mm diameter. In the perforated honeycomb models, channels were perforated in a spiral pattern such that each hole exposed an area of 0.4x0.4 mm^2 to adjacent channels. In the plain and perforated honeycomb, $1/6^{th}$ of the domain was considered with a symmetry boundary condition applied on the side walls to save computational time and cost. However, full geometry modeling was required for the twisted configurations.

3.3.2 Comparison to *in-vivo* Experiments carried out for Strutted Chemofilters

Preliminary animal studies were conducted by collaborators on the strutted Chemofilter configuration [24], therefore the flow and transport through this configuration were also modeled to compare its performance with that of the proposed honeycomb configuration. In the animal studies, two strutted Chemofilter devices with 5 mm diameter were placed in parallel in the porcine IVC, as described in Oh *et al.* [15]. Dox was continuously injected during the first 10 minutes of the study and the concentration downstream and upstream of the device was measured during this time period. In order to compare the computational results with available *in vivo* data, two 30 mm long strutted Chemofilters deployed in parallel were modeled. Since the actual diameter and velocity in the vein were not measured in the experimental study, the model assumed an oval cross section, with a gap between the filters and the wall of the vein. The hydraulic diameter of the elliptical stretched vein was matched with the 10 mm diameter of the vein in the other simulations. The geometry of a strutted configuration with 10 mm diameter, termed the single strutted Chemofilter, was also developed and modeled as an alternative configuration to be deployed in the IVC during future animal studies. For the single strutted Chemofilter, a quarter of the domain was considered and symmetry boundary conditions were applied to the side walls. For the parallel strutted Chemofilter, half of the elliptical domain, cut along the long axis of the ellipse, was modeled with symmetry boundary condition.

3.3.3 Matching Mass and Heat Transport Boundary Conditions

In the mass transport simulations, the Dox mass fraction was set to 0.005 at the inlet and the filter surface was modeled as a mass sink with unlimited binding sites, thus neglecting the saturation of the filter surface or adsorption of other proteins to the surface. In the analogous heat transfer simulations, the temperature of the inlet flow was set to 800 K and the thermal sink on the surface of the filter was modeled with a constant temperature of 300 K, resulting in the cooling of fluid as it passed through the filter. This model is analogous to the reduction of Dox concentration, with the drug adsorbing to the Chemofilter surface instead of heat being transferred. Since Dox does not adsorb to the vessel wall, the wall was set to be adiabatic in the thermal system. The passive diffusion coefficient of Dox in blood (approximately 10^{-10} m^2/s) would result in underestimated drug adsorption for each device configuration due to the effect of electrochemical forces being neglected. The effect of these forces that attract the ions towards

the surface can be expressed in terms of an effective (or active) diffusion coefficient, D_{eff}. According to a multiphysics model that was developed based on the concentrated solution theory, D_{eff} is in the order of 10^{-8} m^2/s [78]. Utilizing this D_{eff} in the simulations of porcine blood flow with an average velocity of 0.01 m/s through the Chemofilter demonstrated close match of the computational and experimental results. Guided by the above results, the diffusion coefficient used in this study was increased to 10^{-7} m^2/s, to match the resulting Peclet number (in the range of 225-450) for the human venal flow.

3.4 Results

3.4.1 Honeycomb Configurations

The performance of alternative Chemofilter configurations was evaluated based on their hemodynamics and transport effectiveness using the heat and mass transport analogy. In Figure 3-2, four configurations of the honeycomb Chemofilter are compared based on their respective filter surface area and temperature drop across the device. The length and diameter of all configurations were kept at 5.8 mm and 10 mm respectively. The plain honeycomb with straight hexagonal channels delivered a temperature drop of 112 K with a corresponding pressure drop of 99 Pa, Figure 3-2 (a). By perforating the channel walls, Figure 3-2 (b), the ΔT increased by 5.36% to 119 K and ΔP decreased to 98 Pa. The addition of a 45° twist angle of the honeycomb channels resulted in a 13.4% increase in ΔT to 127 K with a corresponding pressure drop of 141 Pa, Figure 3-2 (c). Combining the perforations with a 45° twist angle produced the largest ΔT of 151 K and a resulting ΔP of 116 Pa, Figure 3-2 (d). Comparing the twisted-perforated honeycomb to the plain honeycomb, there was a 34.8% improvement in cooling.

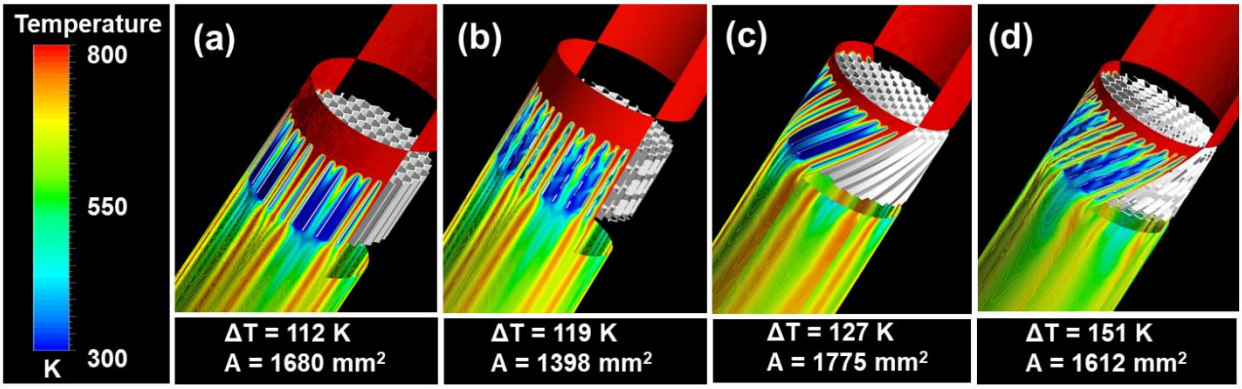

Figure 3-2 Thermal performance of different honeycomb Chemofilter configurations, each with parameters of L_{filter} = 5.8 mm, $\theta_{twist} = 45^0$, D_{hex} = 0.90 mm. Configurations include: a) Plain, b) Perforated, c) Twisted, d) twisted & perforated channels.

In order to verify that the heat transfer analogy adequately represented the filtration of Dox, the results for both transport models were compared as shown in Figure 3-3, showing the temperature drop (a) and Dox mass reduction (b) across the device simulated for identical honeycombs at identical flow conditions. Both heat and species transport models predicted a 42.0% reduction in temperature and Dox mass fraction, respectively. In addition, the matching patterns in the heat maps prove the accuracy of the provided analogy.

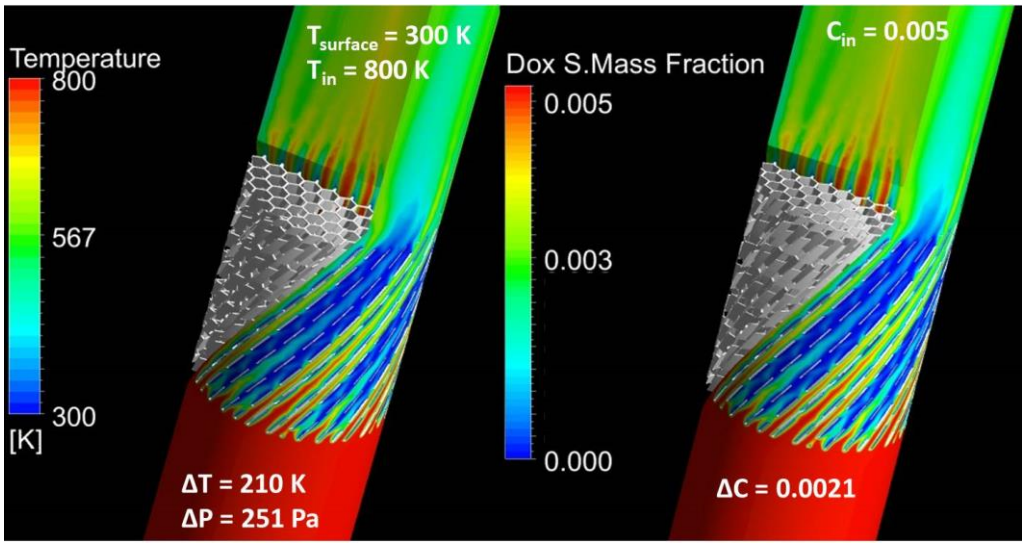

Figure 3-3 Comparison of heat and mass transport results for honeycomb Chemofilter with configuration parameters of L_{filter} = 10 mm, $\theta_{twist} = 45^0$, D_{hex} = 0.90 mm.

3.4.2 Parameter Characterization and Sensitivity Analysis

In order to optimize the geometry of the twisted-perforated honeycomb, the sensitivity of temperature and pressure changes to the parameters stated in Table 3-1 was studied. Figure 3-4 (a) shows that the temperature drop for a plain, 16mm long honeycomb can be increased from 215 K to 387 K by decreasing the channel size from 0.90 mm to 0.45 mm, due to doubling the overall Chemofilter surface area and reducing by half the Peclet number. However, the pressure drop for this configuration with tighter channels increased 3.75 times. The effect of the twist angle on the perforated honeycomb with 5.8 mm length is demonstrated in Figure 3-4 (b). The temperature drop increased from 119 K to 151 K by increasing the twist angle from 0^0 to 45^0, however the pressure drop also increased from 98 to 116 Pa. The effect of the filter length on cooling performance was evaluated in terms of ΔT per unit length. For example, Figure 3-4 (c) shows that the cooling effectiveness of a 45^o twisted-perforated honeycomb decreased from 26.0 K/mm to 17.6 K/mm as the length of the honeycomb increased from 5.8 mm to 20 mm, due to the formation of thermal boundary layers within the channels. However, the pressure drop per length was uniform as expected. A Cotter's sensitivity analysis was performed on channel diameter, flow condition, and diffusion coefficient (marked by * in Table 3-1). Figure 3-4 (d) demonstrates that the effective diffusion coefficient is the dominant factor which defines the binding performance. The overall range of the studied parameters is summarized in Table 3-1.

Table 3-1 Summary of parameters with respective ranges varied during optimization of the Honeycomb configuration Chemofilter

Parameter	D_{Hex}* (mm)	Velocity* (m/s)	θ_{twist} (°)	L_{Filter} (mm)	Spacing (mm)	D* (m^2/s)
Range	0.45 – 0.90	0.01 - 0.10	0 - 45	5.8 - 30	1.3 – 11.6	10^{-9} – 10^{-10}

D_{Hex} *: T*he hexagonal channel diameter*;* θ_{twist}*:* the twist angle; L_{Filter}*:* the length of the Chemofilter*;* Spacing*:* the distance between the stages of honeycomb*; D:* the diffusion coefficient

** Denotes parameters considered for the Cotter's sensitivity analysis.*

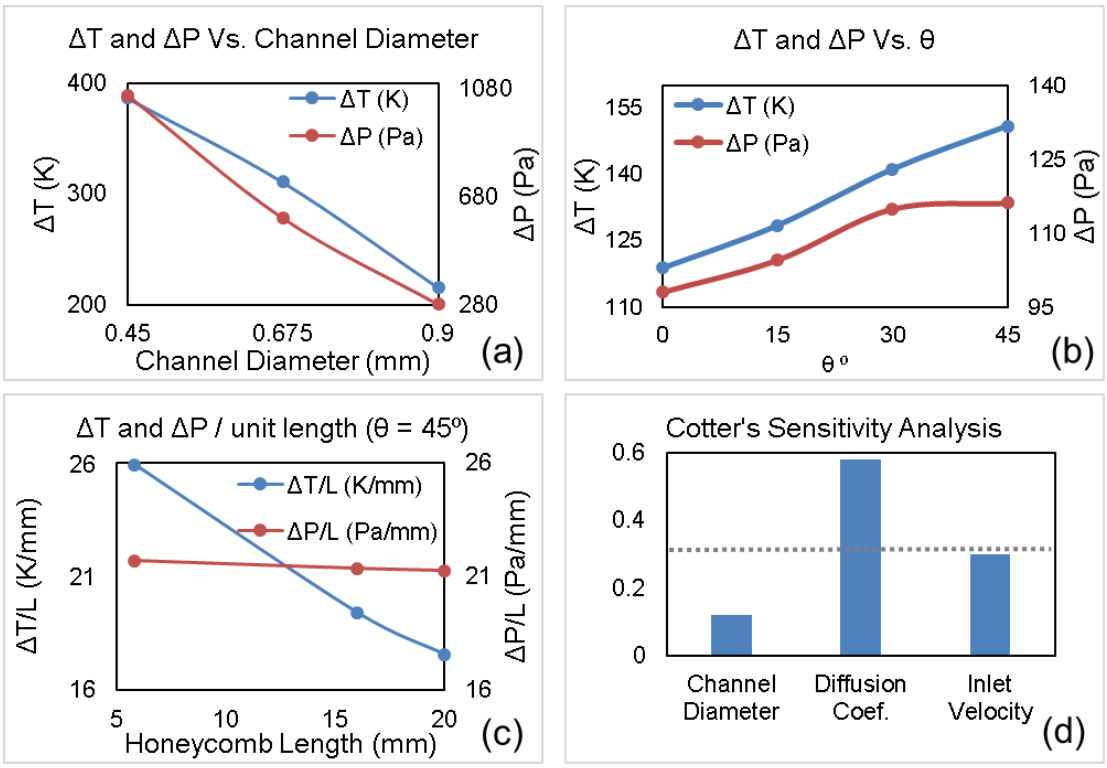

Figure 3-4 Evaluation of temperature and pressure drop as a function of (a) channel diameter, D_{hex} (θ_{twist} = 0, L_{filter} = 16 mm), (b) twist angle, θ_{twist} (L_{filter} = 5.8 mm, D_{hex} = 0.90 mm), and (c) unit filter length, L_{filter} (θ_{twist} = 45, D_{hex} = 0.90 mm). All data points were generated using diffusion coefficient α = 1e-7 m^2/s. (d) Cotter's sensitivity analysis investigating D_{hex}, velocity, and diffusion coefficient.

3.4.3 Final Design: Staged Honeycomb Chemofilter

The decrease in the cooling rate of the fluid (or equivalent drug binding) along the length of the Chemofilter can be addressed by replacing a long continuous honeycomb, by a series of shorter honeycomb sections. A proper spacing distance between sections of the staged honeycomb configuration disrupts the flow and concentration boundary layers formed in the channels and allows re-mixing of the flow prior to entering the channels of the next honeycomb section. Though many simulations were conducted in optimizing the design, six representative models with the channel twist angles of 30° and 45° were chosen for the simulations comparing the continuous and staged configurations as shown in Table 3-2. By comparing temperature drop per unit length in configurations (i.e., model #1 vs. #2 and #5 vs. #6), it can be noted that staged device configurations provide greater cooling performance per unit length than the continuous

configurations. However, the effect of spacing distance can be observed in comparing the models #1 and #2. Though both have the nominal lengths of 20 mm, the continuous configuration has an overall larger ΔT than the staged model.

Table 3-2 Comparison of six representative continuous and staged honeycomb configuration models

Model #	**θ_{twist}**	**Configuration**	**L_{filter} (mm)**	**$A_{surface}$ (mm^2)**	**ΔT (K)**	**ΔP (Pa)**	**ΔT/L (K/mm)**	**ΔP/L (Pa/mm)**
1	30°	Continuous	20	5420	319	371	16.0	18.6
2		Staged (3 sections) 1.3 mm spacing	5.8 x 3	4710	304	337	17.5	19.4
3		Staged (2 sections) 5.8 mm spacing *Flipped*	5.8 x 2	3140	243	240	20.9	20.7
4		Staged (2 sections) 5.8 mm spacing	5.8 x 2	3140	237	227	20.5	19.5
5	45°	Continuous	20	5570	352	425	17.6	21.3
6		Staged (3 sections) 11.6 mm spacing	5.8 x 3	4840	334	391	19.2	22.5

The effectiveness of individual honeycomb stages for models # 2, 3, 4, and 6 (Table 3-2) is demonstrated in Figure 3-5. Comparing the 3 stages of model #2 and #6 shows that by providing larger spacing, the performance of the 2nd and 3rd stages increased. In addition, the overall cooling per unit length increased from 17.5 for model #2 to 19.2 K/mm for model #6 due to increased twist angle. Another strategy for increasing the effectiveness of the staging was to change the secondary flow direction by twisting the channels of the intermediate stage, HC2, in the opposite direction. The increase in mixing through the introduction of centripetal forces is shown by models #3 and #4 in both Table 3-2 and Figure 3-5. Table 3-2 shows only 2% improvement in the cooling due to reversing the twist direction of the second stage. Therefore, the overall performance of each section of models #3 and #4 are approximately equal, with HC1 and HC2 contributing about 60% and 40% of total cooling, respectively (Figure 3-5).

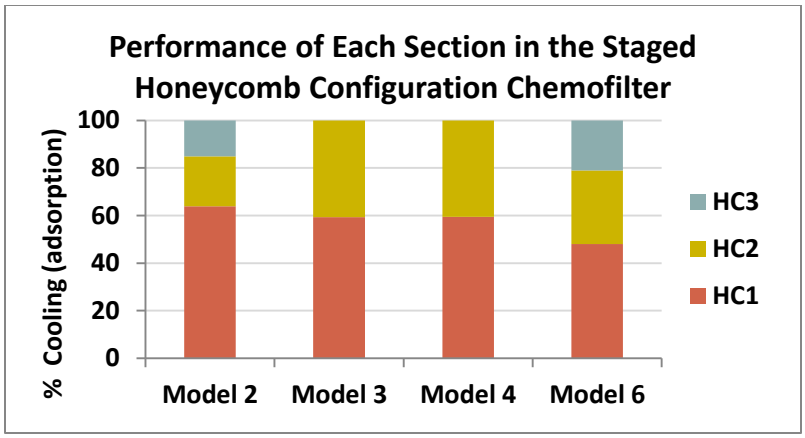

Figure 3-5 Percentage of cooling in each section of the staged honeycomb configuration models. (Model #'s from Table 3-2)

The results of the above simulations were used to determine the optimal Chemofilter design to be used in the next phase of animal studies. Figure 3-1 (c) demonstrates the progression and schematics of the optimized honeycomb Chemofilter, with a length, channel diameter, twist angle, and spacing of 5.8 mm, 0.90 mm, 45^0, and 5.8 mm, respectively.

3.4.4 Comparison to *in-vivo* Experiments carried out for Strutted Chemofilter

The strutted configurations, which were tested in porcine animal studies, are 5 mm in diameter and 30 mm in length [24]. Multiple devices (9 to 12) were deployed into the pig's IVC and hepatic veins during the *in vivo* studies. Due to the increased diameter of the IVC compared to the hepatic veins, the devices were placed next to each other in parallel to fill the lumen. The computational models of parallel and single strutted Chemofilter devices are compared to the continuous honeycombs of identical length in Table 3-3. These simulations of the strutted devices deployed in parallel, predicted a ΔT of 117 K and ΔP of 146 Pa, Figure 3-7 (a), and Table 3-3). The single strutted configuration provided an overall 40.4% reduction in temperature, 202 K with a corresponding ΔP of 288 Pa, while the plain honeycomb provided a 43.0% reduction in ΔT, 215K, with a corresponding ΔP of 281 Pa. Despite the 2.35 times larger surface area, the plain honeycomb configuration resulted in almost the same ΔP. However the cooling increased to 62.2%, with a ΔT of 311 K in the twisted-perforated honeycomb. Moreover, the optimized staged configuration provided a 66.8% decrease in temperature with a corresponding ΔP of 391 Pa (2.9 mm Hg).

Table 3-3 Comparison of strutted and continuous honeycomb configurations.

Model #	**Configuration** (16mm length)		**Area (mm^2)**	**ΔT (K)**	**ΔP (Pa)**	**ΔT/L (K/mm)**	**ΔP/L (Pa/mm)**	**Temperature Drop %**
7	Strutted	Parallel	2050	117	146	7.30	9.10	23.4
8		Single	1950	202	288	12.6	18	40.4
9	Honeycomb	Plain	4590	215	281	13.4	17.6	43.0
10		Twisted-Perforated	4460	311	342	19.4	21.4	62.2

The temperature drop along the length of the Chemofilter for alternative designs is shown in Figure 3-6. The entrance region of each device demonstrates the greatest rate of temperature drop. The strutted design (model #8) demonstrates the lowest slope due to the more monotonic and undisturbed flow it promotes, while the continuous and staged honeycombs (models #5, 6, 10) demonstrate greater slopes. The staged honeycomb configuration (model #6) performed better for the longer device, as shown by the continuous decrease in temperature. Numerical results predict a three-fold improvement in cooling by the staged honeycomb compared to the parallel strutted Chemofilter. These results are also visualized as temperature contours in Figure 3-7.

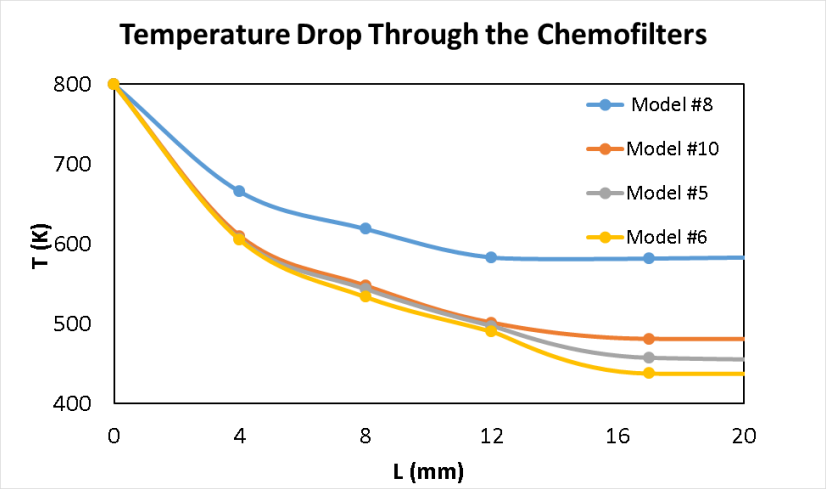

Figure 3-6 The temperature drop along the length of different Chemofilter configurations.

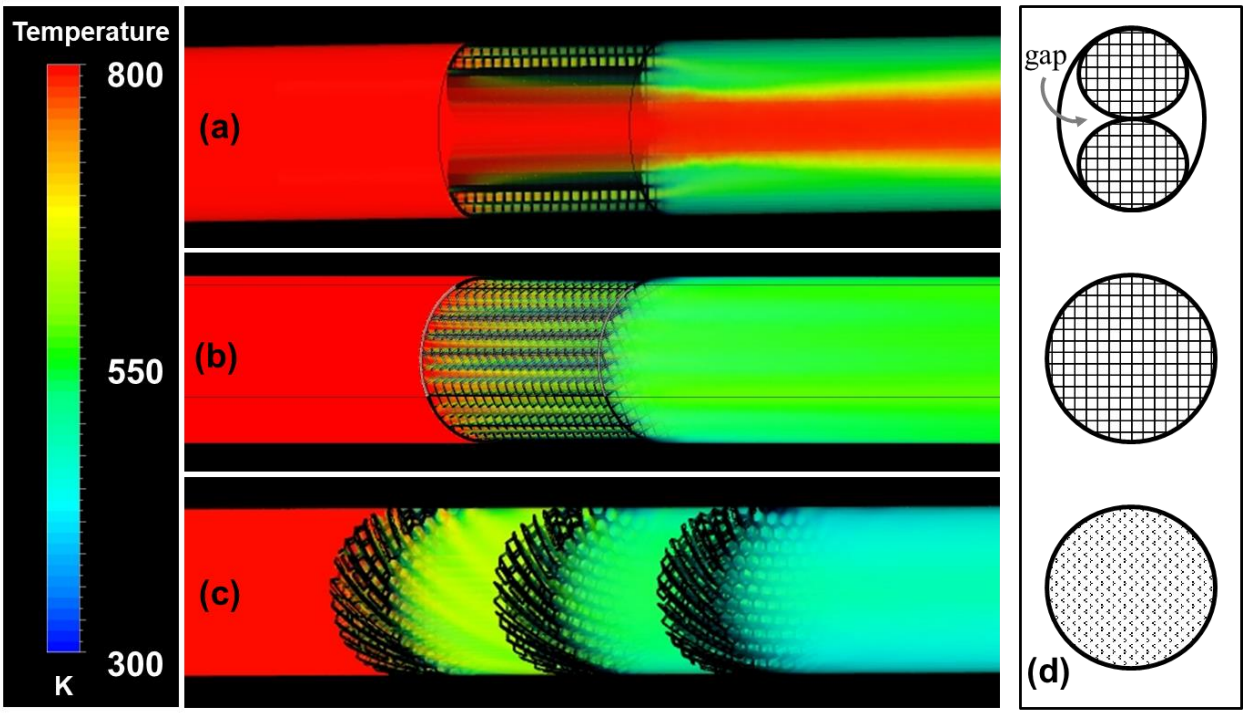

Figure 3-7 The temperature drop through (a) parallel strutted, (b) single strutted, and (c) staged honeycomb configurations. (d) A cross sectional view through each configuration, a-c.

3.5 Discussion

3.5.1 Honeycomb Configurations

The mass and heat transfer analogy was used to evaluate and optimize the Chemofilter design. In this analogy, the temperature drop of a hot fluid passing through the cold device was used to represent the change in the drug concentration due to adsorption. The channels closer to the vessel wall experienced larger temperature drop (drug adsorption) because of the slower velocity and larger flow residence time. The near-wall channels, which are not full hexagons, have the lowest velocity and therefore resulted in the greatest temperature drop as demonstrated in Figure 3-2 and Figure 3-3.

Since the passive diffusion of Dox in blood is low, the advection is dominant everywhere in the flow except in the near wall region (the average Peclet number is 10^5). Therefore, the low diffusion of Dox in blood can be compensated for by increasing the length of channels to provide larger residence time, and allow more Dox diffusion towards the surface. The preliminary *in vitro* and *in vivo* studies showed that drug binds to the entrance region of the Chemofilter more effectively, which is supported by computational studies. Flow mixing in the entrance of the

channels facilitates adsorption, as the concentration gradient is higher at the entrance. The boundary layers forming in the channels act like a transport insulator, thus decreasing the rate of drug adsorption unless the geometry or flow conditions change. One way of enhancing the mixing is to perforate the honeycomb channels to allow the flow from one channel to mix with the adjacent ones, as shown in Figure 3-2 (b).

The mixing can be further enhanced by twisting the honeycomb channels in order to induce secondary flow. The effectiveness of twisting can be estimated by the dimensionless Dean number. In the twisted honeycomb, the channels closer to the center of the vessel have the Dean number of 60, which is the threshold for the appearance of Dean's vortices. The Dean number decreases in the channels away from the center due to the lower Reynolds number, even though the radius of curvature is increased. The low inertia of flow in the vein limits the effect of centripetal forces on the development of the secondary flow. However, in the near wall channels lower velocity results in a smaller Peclet number, which compensates for the absence of Dean vortices due to larger residence time.

The results shown in Figure 3-2 (b-c) demonstrate that perforation and twisting of the channels result in increased temperature drop across the device, with the design combining both features delivering the best performance for the honeycomb configuration. In the twisted-perforated model, the flow is not isolated in the individual channels and the formation of fully developed flow is disrupted due to the secondary flow. It should be noted that the total surface area of the twisted-perforated honeycomb was reduced relative to the plain configuration, while the cooling was further increased. Figure 3-4 (b) shows that by increasing the twist angle, the binding increases while the pressure drop remains below the estimated threshold for flow stagnation (5-7 mm Hg) in the IVC and therefore the 45° twist angle was suggested for the honeycomb prototype.

3.5.2 Parameter Characterization and Sensitivity Analysis

Decreasing the diameter of channels resulted in larger adsorption, Figure 3-4 (a), since the total area in contact with the flow increased. Consequently, the number of binding sites increased, while the diffusion length scale decreased. The ideal Chemofilter configuration provides maximal change of the temperature and low pressure drop, with minimal reduction in cooling rate along the Chemofilter. However, the smaller channels resulted in larger pressure

drop due to increased resistance to the flow. Based on the mass transfer correlations derived by Sieder-Tate for laminar flow [82], the pressure drop and heat transfer in a cylindrical channel change proportional to D^{-2} and $D^{-4/3}$ respectively. Therefore, a cross-point between the two parameters does not exist, as both trend asymptotically in the same direction. As a result, the optimum size of the channels can only be decided by setting a safe threshold for pressure drop to avoid stagnation of the venous flow.

The temperature and pressure drop per unit length provide a measure for characterizing different device configurations and ranking their effectiveness. The pressure drop is only a function of length, for a given channel size, and therefore is constant along the filter's unit length, but the temperature gradient decreases along the channel due to formation of the boundary layers. To avoid the fully developed boundary layer, the channel's length should be shorter than the entrance length. Figure 3-4 (c) also shows that shorter honeycombs have larger temperature change per unit length.

Among the three honeycomb configuration parameters that were studied (channel diameter, twist angle, and Chemofilter length) the dominant parameter was the channel diameter, which caused a two-fold increase in temperature drop when decreased by half in size. Magnifying the passive diffusion coefficient in this study served to estimate the effective diffusion coefficient accounting for the effect of electrochemical forces which may dominate the drug binding. The variation in the average vein velocity is due to the difference between the human and porcine circulation. The results suggest that the dominant parameter determining the binding effectiveness is the diffusion coefficient.

3.5.3 Final Design: Staged Honeycomb Chemofilter

A staged configuration of the device was suggested in order to utilize the high effectiveness of short honeycomb stages without compromising the required surface area of the device. The ideal staging of the devices would result in equal effectiveness of all stages, which means that the flow would be properly mixed before entering each stage. The effect of spacing between the short honeycomb sections was investigated in simulations where the spacing of 1.3, 5.8, and 11.6 mm was used. For example, comparing the continuous model #1 and staged model #2 with 1.3 mm spacing distance, both with identical nominal lengths of 20 mm, the continuous configuration has an overall larger ΔT than that staged model, due to an insufficient distance for

mixing between the stages. Therefore, a short spacing distance only results in reduction of the surface area without utilization of the benefits of the staged configuration. The results show that spacing equal to or larger than the length of the stage provides sufficient flow mixing before it enters the next stage. Another benefit of staging the honeycombs is improved flexibility in device deployment. The number of required Chemofilter stages can be decided by clinicians based on the location of the catheter and patient's vascular anatomy. The benefit of using stages with alternating direction of the twist angle of the channels was also studied. Due to the low inertia of venous flow (Re < 60), this feature was not found to have a significant effect on the resulting temperature changes.

3.5.4 Comparison to *in-vivo* Experiments Carried out for Strutted Chemofilter

The strutted device configurations were developed and used in animal studies to examine the electrochemical binding mechanism for capturing Dox from the blood stream. In the hepatic veins with diameter of 5 mm, the deployment of filters with corresponding size resulted in a close fit in the vein without a gap near the wall. However, the same filter deployed in the IVC moved next to the wall following the guide wire, and the main flow bypassed it. Therefore, two strutted devices were deployed in parallel in the IVC to compensate for this effect. With the placement of two parallel Chemofilters in the hepatic vein, the cross section of the vein was assumed to deform to an oval, resulting in the formation of regions of low resistance in the gaps between the vessel wall and the two filters. The gaps lead to high velocity regions forming between the parallel filters, Figure 3-7 (a), which allowed 63% of blood flow to pass unfiltered, thus resulting in inefficient filtration. Since the gap reduced the resistance to flow, the overall pressure drop across the device was low. However, this decreased resistance also caused a decrease in filtration efficiency. The analysis of the effect of the near-wall gap on device filtration was reported previously in Maani *et al.* [76]. The performance of the strutted Chemofilters illustrated in Figure 3-7 (a-b) is also quantified in Table 3-3. The models of the parallel and single strutted configurations demonstrate that by correctly fitting the device to the intended site of deployment, the overall temperature change downstream of the device improved by 72.6% compared to the parallel strutted configuration, as shown in Table 3-3 and Figure 3-7. The overall performance of the single strutted filter was comparable to that of the plain, un-optimized honeycomb.

Oh *et al.* reported that the strutted Chemofilter delivered a decrease in Dox concentration of 64 ± 6% following the 10-minute injection period [24]. In their study it was assumed that 100% of excess Dox was present in the plasma samples, however it is likely that only about 85% of Dox is present in the plasma [39]. By accounting for this discrepancy, the experimental Dox concentration change reported by Oh *et al.* becomes 54 ± 5%. The computational model of the same device configuration (parallel strutted Chemofilter with inlet velocity of 0.01 m/s) estimated that 50% of Dox would be eliminated from the blood stream, which approximately matches the adjusted results reported by [24]. Despite the observed success of the strutted Chemofilter configuration in achieving significant reduction of the Dox concentrations, computational models suggest that the filtration performance can be further improved by the staged honeycomb Chemofilter.

3.6 Limitations and Future Work

In this study, the mass diffusion coefficient of Dox was matched to the thermal diffusion coefficient of water to facilitate the comparison. In reality, the binding of Dox to the ionic resin is driven by an electrochemical force attracting the particles towards the surface. The electrochemical binding is addressed by applying the dilute and concentrated solution theory approximation in the following chapter (Ch. 4).

Moreover, a direct comparison between the available animal studies and computational results is challenging due to the limitations of the animal study protocol. Namely, during *in vivo* studies the exact cross sectional area, filter position in the vein, and blood velocity in the vein were not measured; therefore the values used in the CFD simulations were taken from literature. To address this problem, Doppler ultrasound measurements will be performed during the next experiments to obtain the accurate cross sectional area and vein velocity, thus enabling a fair comparison of the results. It should be noted that the strutted Chemofilter used for *in vivo* studies contained active sites on the outer surface of the device, where it may contact the vessel wall; whereas in the optimization simulations this area is treated as a non-binding wall and the performance was underestimated.

Also, in this study the blood velocity in the vein was based on values observed in the human IVC, while the velocity in the porcine IVC is about one order of magnitude lower than that of human. Nevertheless, since the flow and transport conditions remain the same in all CFD

studies of the alternative device configurations, the results and conclusions remain valid for a comparison. Using the data provided by the animal studies of the ion-exchange mechanism Chemofilter, the results of the multi-physics models will be calibrated to improve the agreement between different modalities. Based on the results presented in this study, the future *in vitro* and *in vivo* studies will be performed with the optimized honeycomb device and the drug concentration will be compared to the previous set of studies with the strutted Chemofilter.

3.7 Conclusion

In this study, the configuration of the Chemofilter device intended for filtering excessive chemotherapy drugs from blood was optimized with multiphysics CFD modeling. The hemodynamic performance and drug elimination efficiency of a honeycomb-shaped device was compared with that of a strutted Chemofilter, previously tested in animal studies. Utilizing the analogy between the heat and mass transport, a numerical model for evaluating drug transport and chemical binding was developed. The honeycomb-shaped configuration containing multiple parallel channels provided increased surface area for drug binding. The mixing and binding of the drug can also be enhanced by using twisted and perforated channels, which resulted in 44.6% improvement compared to the straight channel design for a honeycomb with the same length. A staged configuration of the honeycomb was suggested to further increase the overall efficiency of the device, which also provided flexibility for deployment of the device during catheterization. The short stage length allowed sufficient mixing and using multiple stages provided the required residence time for the adsorption of drug particles. The comparison of the honeycomb and strutted Chemofilters demonstrated the superior performance of the optimized honeycomb configuration, by 57.4% improvement in drug concentration reduction. Computational simulations allowed the performance of different Chemofilter device configurations to be evaluated, enabling device optimization with minimal need for *in vivo* experiments.

CHAPTER 4. ELECTROCHEMISTRY OF DOX BINDING TO THE ION-EXCHANGE RESIN: AN EFFECTIVE DIFFUSION COEFFICIENT TO ACCOUNT FOR IONIC MIGRATION TIPS

4.1 Introduction

This study is conducted to model the Dox transport in blood flow, and its electrochemical adsorption to the ion-exchange resin, as a part of the computational optimization of the Chemofilter device. Preliminary porcine studies were performed by collaborators with deployment of an ion-exchange Chemofilter prototype with strutted configuration in the common femoral vein, where Dox was injected upstream of the device. Analysis of blood aliquots, from 5 post-device samplings during the 10 minutes of injection, showed the removal of 64±6% of Dox from blood plasma [24]. Electrochemical forces attract positively charged Dox particles (cationic) towards the sulfonate group, $R-SO_3^-$, of the resin which covers the Chemofilter surface (anionic). This results in the induction of a charge density in the solution which greatly impacts the overall flux of particles.

In this study, three distinct models are presented to investigate the contribution of electrochemical forces on the adsorption of Dox to the Chemofilter surface. The mathematical relationships for electrochemical flux of Dox towards the Chemofilter surface were developed based on 1) passive diffusion, 2) dilute solution theory, and 3) concentrated solution theory. Computational Fluid Dynamics (CFD) simulations were then conducted based on the results of these models in order to simulate blood flow and drug transport through different Chemofilter configurations. In order to determine the accuracy of the predicted drug transport and adsorption in each model, the CFD results were compared against the experimental results.

4.2 Theory

In order to develop the computational model of Dox interaction with the Chemofilter surface, different mathematical models were examined. Electrochemical forces are dominant in the Electric double layer (EDL), adjacent to the surface, where binding of the particles is assumed to be instantaneous. In the EDL, the ion's velocity field is not divergence free and is a function of the electrophoretic mobility of ions in the solution. This term is a function of the

electrostatic potential of the electrochemical system and is referred to as the migration term [24]. In this study, it was *hypothesized* that the diffusive and migration term in the material balance equation could be fused into an effective diffusion coefficient term, D_{eff}, which is a function of both the concentration and diffusivity of the ions in the solution. In the dilute solution approximation, the induced migration of ions was accounted for by using the Nernst-Plank equations [24, 41, 83], where the solution of *Dox-Cl* in plasma was approximated as 1) a binary solution, and 2) the non-binary solution. In the concentrated solution approximation, the closed form of the effective diffusion coefficient was derived for a binary solution of *Dox-Cl* in plasma, and its value was approximated.

4.2.1 Dilute Solution Theory (Nernst-Plank)

In an electrochemical system, the flux density of each dissolved species, N_i [mol/cm^2], is due to three transport mechanisms, migration, diffusion, and advection, which are shown in the three terms of Eq. 4-1:

$$N_i = -z_i u_i F c_i \nabla \psi_i - D_i \nabla c_i + c_i \mathbf{v} \quad (4\text{-}1)$$

where z_i is the number of proton charges carried by an ion *i*, u_i is the mobility of species *i*, *F* is the Faraday's constant, c_i is the concentration of ion *i*, ψ is the electrostatic potential, D_i is the diffusion coefficient of species *i*, and **v** is the advective velocity. The material balance for a minor component can be found as:

$$\frac{\partial c_i}{\partial t} = -\nabla \cdot N_i + \mathcal{R}_i \quad (4\text{-}2)$$

where $\mathcal{R}_i$ is the reaction (source) term. In the binding of Dox to the ionic resin, the electrochemical force between Dox^+ and $SO_3{}^-$ attracts the particles towards the surface. Assuming a binary electrolyte, the Dox particles in the injected $Dox - Cl$ solution dissociate (as shown in Eq. 4-3) to Dox^+ (cation) in plasma (solvent) and bind to the surface (Eq. 4-4), where they form solid species which remain on the surface.

$$Dox - HCl \rightarrow Dox^+ + Cl^- \text{ (in solution)} \quad (4\text{-}3)$$

$$Dox^+ + SO_3{}^- \rightarrow Dox - SO_3 \text{ (binding of Dox to the surface)} \quad (4\text{-}4)$$

By substituting the ion's flux (1) to the material balance (2) and rearranging the mathematical equations, the balance equation for Dox cations reduces to:

$$\frac{\partial c}{\partial t} + \mathbf{v} \cdot \nabla c = D_{eff} \nabla^2 c + \mathcal{R} \quad (4\text{-}5)$$

where concentration of the electrolyte is $c = \frac{c_+}{\nu_+} = \frac{c_-}{\nu_-}$ and ν_+ and ν_- are the number of moles of cations and anions that are produced from dissociation of one molecule of the electrolyte (Appendix A). Eq. 4-5 resembles the advection-diffusion-reaction equation [41], with the difference that the passive diffusion coefficient is replaced with the effective diffusion coefficient as:

$$D_{eff-db} = \frac{z_+u_+D_- - z_-u_-D_+}{z_+u_+ - z_-u_-} \tag{4-6}$$

where *db* stands for dilute-binary and the subscripts + and – stand for cation and anion, respectively. Note that migration term is present when an external potential is applied to the system. In the case of Dox binding to the Chemofilter surface, no external potential is present. Instead, an induced potential term appears in the balance equation due to the electrophoretic mobility of ions. The mobility term results in the addition of a non-divergence-free term in the velocity as $\mathbf{v}_+ = -z_+u_+F\nabla\psi$, where $\mathbf{v} = \mathbf{v}_0 + \mathbf{v}_+$ (see details in Appendix). Therefore, a charge density is induced in the presence of a concentration gradient or difference in the diffusion coefficient of anion and cation (note that the diffusion coefficient of Dox is about one order of magnitude lower than other ions such as Cl^- or Na^+). This charge density creates a non-uniform potential which accelerates the ions with smaller diffusion coefficient towards the surface [41].

In the next model, the effective diffusion coefficient was derived for the case where the binding sites were not free and the ionic bond on the surface should be overcome before the Dox particles could bind to the surface. This condition was investigated by Schlogl for an electrostatic system [84, 85], where the exchange of cations from the solution and the resin was considered as:

$$A_s{}^+ + B_r{}^+ \rightarrow A_r{}^+ + B_s{}^+ \tag{4-7}$$

where *r* denotes resin and *s* denotes solution. In their study, the Nernst-Einstein relationship was utilized to derive the flux of particles as a function of concentration gradient for an electrostatic system (Appendix A). In this study, Schlogl's model [84, 85] was expanded to model the flow dynamics, which results in the balance equation as presented in Eq. 4-5 with an effective diffusion coefficient of:

$$D_{eff-dnb} = -\frac{2D_A\,(C_A+C_B)}{\left(\frac{D_A}{D_B}+1\right)C_A+2C_B} \tag{4-8}$$

Where *dnb* stands for dilute-non-binary, and *A* and *B* were assumed to be Dox^+ and Na^+. In the new effective diffusion coefficient based on Schlogl binding conditions, $D_{eff-dnb}$ is a variable and a function of the concentration of the ions.

4.2.2 Concentrated Solution Theory

Even though Nernst-Plank equation is widely used in the modeling of electrochemical systems, its application is limited to dilute solutions and its results are based on several limiting assumptions, such as assumption of ions as point charge to utilize Nernst-Einstein relationship [41]. Therefore, in the next step of this study, the concentrated solution model was investigated to derive a more generally valid model of electrochemical binding of Dox to the Chemofilter surface [41, 86].

In general, there are three main parameters that define the performance of an electrolyte in a concentrated electrochemical system which can be found experimentally; namely 1) the diffusion coefficient, D, 2) the ionic conductivity, κ, and 3) the transference number, t_+^0 [86, 87]. In the concentrated solution theory, the effect of migration and diffusion are expressed in terms of electrochemical potential as shown in Eq. 4-9. This equation is analogous to Eq. 4-1 in dilute solution [41].

$$c_i \nabla \mu_i = RT \sum_j \frac{c_i c_j}{c_T \mathfrak{D}_{ij}} (\mathbf{v}_j - \mathbf{v}_i) \qquad i, j = +, -, 0 \tag{4-9}$$

Where $\mathbf{v}$ is the velocity of the species and its subscripts are corresponding to the cations $(+)$, the anions $(-)$, and the solution (0). In this equation, the interaction of species *i, j* is expressed in terms of Stefan-Maxwell diffusion coefficients, $\mathfrak{D}_{ij}$, to quantify the relationship between the species velocity, $\mathbf{v}_i$, and the electrochemical potential gradient, $\nabla \mu_i$ [41].

For a binary electrolyte the flux of the cation and the anion is expressed as:

$$\mathbf{N}_+ = c_+ \mathbf{v}_+ = -\frac{\nu_+ \mathfrak{D}}{\nu RT} \frac{c_T}{c_0} \nabla \mu_e + \frac{\mathbf{i}\, t_+^0}{z_+ F} + c_+ \mathbf{v}_0 \tag{4-10}$$

$$\boldsymbol{N}_- = c_- \mathbf{v}_- = -\frac{\nu_- \mathfrak{D}}{\nu RT} \frac{c_T}{c_0} \nabla \mu_e + \frac{\boldsymbol{i}\, t_-^0}{z_- F} + c_- \boldsymbol{v}_0 \tag{4-11}$$

where $\nu = \nu_+ + \nu_-$ and $\mu_e = \nu_+ \mu_+ + \nu_- \mu_-$and the current density is defined as:

$$\mathbf{i} = -\kappa \nabla \psi - \frac{\kappa}{F} \left(\frac{s_i}{n \nu_+} + \frac{t_+^0}{z_+ \nu_+} - \frac{s_0 c}{n s c_0} \right) \nabla \mu_e \tag{4-12}$$

where s_i is the stoichiometric coefficient of species *i* and *n* is defined as: $s_+ z_+ + s_- z_- = -n$. It was assumed that the concentration gradient of anion, Cl^-, was negligible, as plasma already

contains high concentration of Cl^{-}, and $n = -1$.Moreover, the first term in the right hand side of Eq. 4-12 was neglected, as there was no external electric potential in the system, thus, the induced current is defined in terms of $\nabla\mu_e$. The gradient of concentration is related to the gradient of electrochemical potential as described by Newman [41] in Eq. 4-13:

$$\frac{\mathfrak{D}}{\nu RT}\frac{c_T}{c_0}\, c\, \nabla\mu_e = D\left(1 - \frac{dlnc_0}{dlnc}\right)\nabla c \tag{4-13}$$

Rearranging the equations, as detailed in the appendix, the final balance equation was reduced to:

$$\frac{\partial c}{\partial t} + \nabla\cdot(c\mathbf{v}_0) = \nabla\cdot\left[D\left(1 - \frac{dlnc_0}{dlnc}\right)\left(1 - \frac{\kappa}{z_+F}\left(\frac{s_+}{n\nu_+} + \frac{t_+^0}{z_+\nu_+} - \frac{s_0 c}{nsc_0}\right)\left(\frac{\nu RT t_+^0}{\mathfrak{D}c}\frac{c_0}{c_T}\right)\right)\nabla c\right] + \mathcal{R} \tag{4-14}$$

and

$$D_{eff-cb} = D\left(1 - \frac{dlnc_0}{dlnc}\right)\left(1 - \frac{\kappa}{z_+F}\left(\frac{s_+}{n\nu_+} + \frac{t_+^0}{z_+\nu_+} - \frac{s_0 c}{nsc_0}\right)\left(\frac{\nu RT t_+^0}{\mathfrak{D}c}\frac{c_0}{c_T}\right)\right) \tag{4-15}$$

Equation 4-15 is a closed form expression of the effective diffusion coefficient which includes the effect of induced migration in the concentrated solution, D_{eff-cb}, as a function of the passive and Stefan-Maxwell diffusion coefficients (D and $\mathfrak{D}$), transference number (t_+^0), conductivity (κ), and concentration of cation and solvent, which are all measurable in experiments.

4.3 CFD Modeling

Three different configurations of the Chemofilter device were considered (Figure 3-1) for the CFD simulations, 1) the porous Chemofilter basket which is composed of a lattice of cells formed by micro-trusses [76], and 2) the non-porous honeycomb Chemofilter consisting of parallel hexagonal channels arranged in three separate stages [77], and 3) the non-porous strutted Chemofilter, which was used in preliminary animal studies [24]. The above configurations differed in their length scale, which was about one order of magnitude smaller in the architected lattice (in the order of 100 μm), resulting in smaller diffusion time-scale and consequently a smaller Peclet number. The geometries for all configurations were generated in SolidWorks software and the CAD files were then imported to ANSYS ICEM for discretization. The details of discretization, mesh sensitivity analysis, and numerical schemes used in the simulations were described in previous chapters [76, 77].

The Navier-Stokes and Advection-Diffusion-Reaction equations were coupled in ANSYS Fluent, to calculate the flow and transport of the Dox through the Chemofilter. The flow was modeled as steady due to negligible effect of the cardiac pulse in the hepatic vein and laminar as the Reynolds number was equal to 30. The inlet velocity was set to 0.01 m/s to match the porcine venous flow and the outflow boundary condition was assigned to the outlet. In the adsorption of Dox to the Chemofilter, the body force was expressed as a sink term to model the elimination of the bound Dox from the system. During the IAC procedure, a steady dose of Dox was injected in the artery for about 10 minutes. In this time window, it was assumed that the efficiency of Dox, i.e. the percentage of Dox that intercalates with tumor cells, and binding capacity of the Chemofilter, i.e. the number of available binding sites, remained constant. In other words, the mass fraction of Dox at the vein's inlet was constant and the Chemofilter surface did not saturate. Therefore, the steady state conditions were assumed during the injection period.

Table 4-1 The progress of developing the computational model for Dox binding to the Chemofilter surface

<table>
<tr><th colspan="3">Models</th><th>D</th><th>Equation</th></tr>
<tr><td>1</td><td colspan="2">Passive binding</td><td>constant</td><td>---</td></tr>
<tr><td rowspan="2">2</td><td rowspan="2">Dilute solution</td><td>Binary</td><td>constant</td><td>Eqn (6)</td></tr>
<tr><td>Non-binary</td><td>depend on concentration of ions</td><td>Eqn (8)</td></tr>
<tr><td>3</td><td colspan="2">Concentrated solution</td><td>depend on concentration of ions</td><td>Eqn (15)</td></tr>
</table>

To model Dox binding to the Chemofilter, the energy and species transport were activated in Fluent. The chemical reaction was modeled by solving the material balance equation for all species that were introduced in a mixture except the bulk fluid (blood). The chemical reactions were based on Arrhenius model ($k = A_r\, T^{\beta_r} e^{-E_r/RT}$), where k is the rate constant. Finite rate reaction was chosen for laminar flow and Arrhenius constants were $A_r = 1e20$, $\beta_r = 0$, $E_r = 0$. Mass deposition source was activated to include the effect of surface mass

transfer in the continuity equation. The density was calculated based on volume rated mixing law and the diffusivity of Dox in plasma was used in the simulations, set to 2.442×10^{-10} m^2/s, since the majority of the Dox particles reside in blood plasma. Dox mass fraction at the inlet was 0.005, and the site density was set to 1e-8 $kgmol/m^2$. It was assumed that the temperature did not change in this process, thus, the energy balance equation was not solved.

In this study, three models were developed for Dox transport and binding to the Chemofilter surface, as summarized in Table 4-1. In the initial studies, model 1, the induced migration term was neglected and only a constant diffusion of Dox towards the surface was considered. This diffusion coefficient was varied in the computations from 10^{-10} m^2/s (passive diffusion) to 10^{-8} m^2/s to estimate the order of magnitude of the effective diffusion coefficient. In model 2, the dilute solution approximation, the simulations were conducted for both the binary and the non-binary electrolyte and the results were compared for different Chemofilter configurations. The diffusion of Chloride anion and sodium cation in blood were set to 2.032×10^{-9} and 1.334×10^{-9} m^2/s, respectively [41]. In model 3, the binary concentrated solution approximation, the simulations were conducted based on an estimated D_{eff} for high-molecular-weight non-structured polystyrene-*b*-poly(ethylene oxide) (SEO) copolymer electrolyte doped with a lithium salt, due to the lack of experimental data for Dox performance in plasma [87]. In the species transport, D_{eff} was incorporated into each numerical model with an external User Defined Function (UDF). The UDF was developed in C language and implemented via the species transport dialogue box in Fluent.

4.4 Results

4.4.1 Model 1

Figure 4-1 shows the results of the preliminary study for different diffusivity values of the passive particles. A representative element of the porous Chemofilter membrane was modeled as three layers of architected material, each layer consisting of 2x2 matrix of microcells. The concentration of Dox decreases as blood flows through the architected lattice of the Chemofilter. The passive diffusion coefficient was equal to 10^{-10}, 10^{-9}, and 10^{-8} m^2/s, corresponding to the Peclet number of 5000, 500, and 50 for the average velocity set to 0.01 m/s. The overall Dox mass fraction at the outlet of the flow domain was predicted to be 0.00474,

0.00395, and 0.00146, corresponding to Dox concentration reduction of 5.2%, 11.6%, and 70.8% for the diffusion coefficients of 10^{-10}, 10^{-9},10^{-8} m^2/s., respectively.

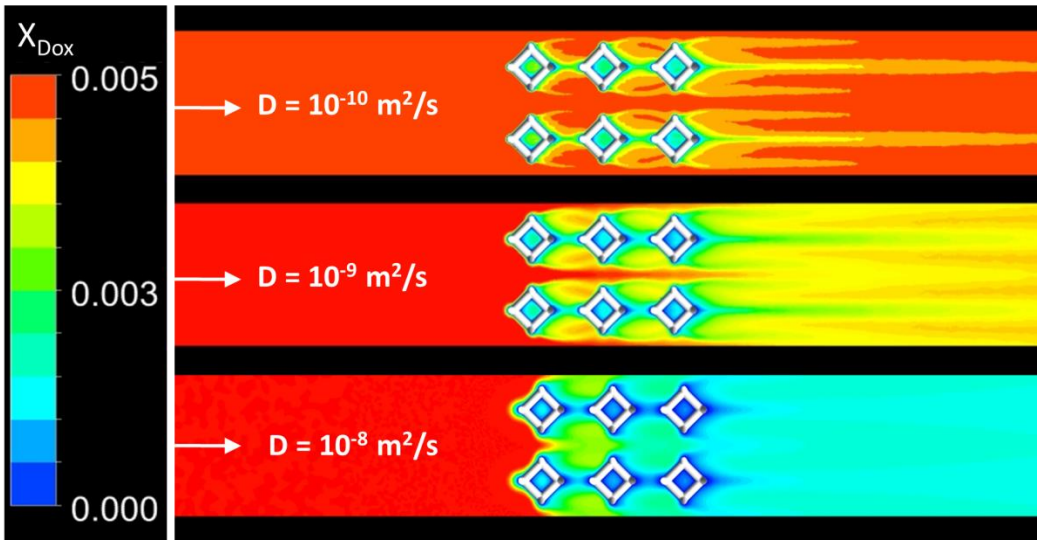

Figure 4-1 The heat map of Dox concentration for a section through the porous membrane computed for a constant diffusion coefficient of a) 10^{-10} m^2/s, b) 10^{-8} m^2/s, c) 10^{-7} m^2/s. (inlet velocity is 0.01 m/s and Dox mass fraction is 0.005 at the inlet)

4.4.2 Model 2

Based on the relations derived for the dilute solution, the effective diffusion coefficient of the binary *Dox-Cl* electrolyte was a constant which depended only on the diffusion coefficients of *Dox* and *Cl* ions in the solution. By using the Nersnt-Einstein relation to express the mobility of ions in term of passive Diffusivity, Equation 4-6 was used to calculate the $D_{eff\text{-}db}$ to be 4.128×10^{-10} m^2/s. However, in a non-binary electrolyte with Schlogl assumptions [84, 85], the $D_{eff\text{-}dnb}$ was a function of the concentrations of *Dox* and *Na*, as well as their passive diffusion coefficients. The mass fraction of Dox computed for the flow through a matrix of architected lattice as well as though the 3-stages of the twisted perforated honeycomb configuration is shown in Figure 4-2 (a) and b, respectively. The lowest value of $D_{eff\text{-}dnb}$, 2.44×10^{-10} m^2/s, was found in the near wall region, where the instantaneous binding results in the elimination of Dox particles and their lower concentration. With the decrease of Dox ions away from the walls and release of *Na* ions to the solution, $D_{eff\text{-}dnb}$ in the bulk of the flow increased to 4.36×10^{-10} m^2/s, as demonstrated in Figure 4-2 (c).

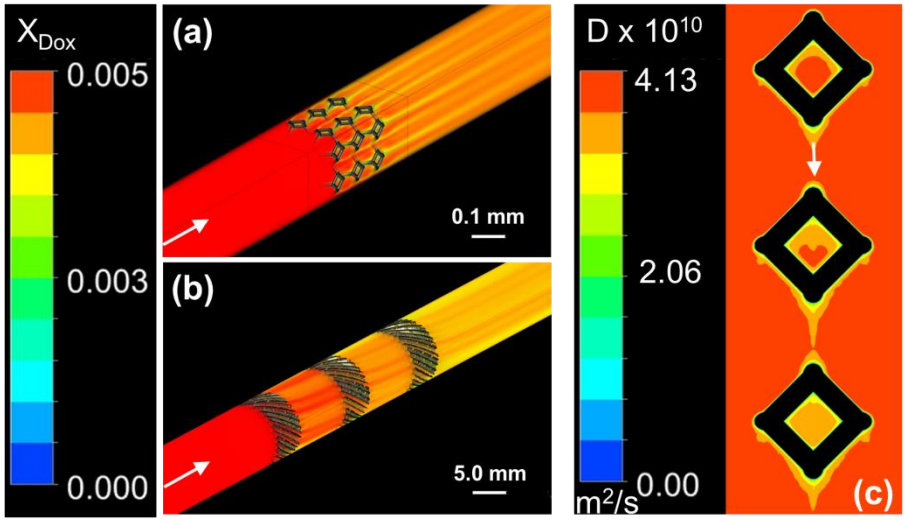

Figure 4-2 Comparison of results based on the dilute non-binary approximation (Schlogl model [84, 85]). Mass fraction of Dox through a) an architected lattice, b) a non-porous 3-stage honeycomb, c) the effective diffusion coefficient of Dox around the microcells of the architected lattice

The overall comparison of Dox binding for different Chemofilter configurations based on the dilute binary and dilute non-binary approximations are presented in Figure 4-3. Based on the computational predictions for the dilute binary model, the non-porous honeycomb eliminated 13.8% of Dox from the blood stream, while this binding performance decreased to 12.6% for the architected lattice, and 5.8% for the non-porous strutted configuration. with dilute non-binary approximation. The performance of the above configurations reduces to 12.2%, 11.6% and 5.2% respectively. These results were obtained for the honeycomb and strutted configurations with the respective surface area of 4800 mm^2, and 1900 mm^2, and for the surface area of the architected lattice, expanded across a vein with the same cross section of 6100 mm^2. The pressure drop through the honeycomb and strutted configurations were 391 Pa, 288 Pa, respectively, while the pressure drop through the porous Chemofilter basket is320 Pa.

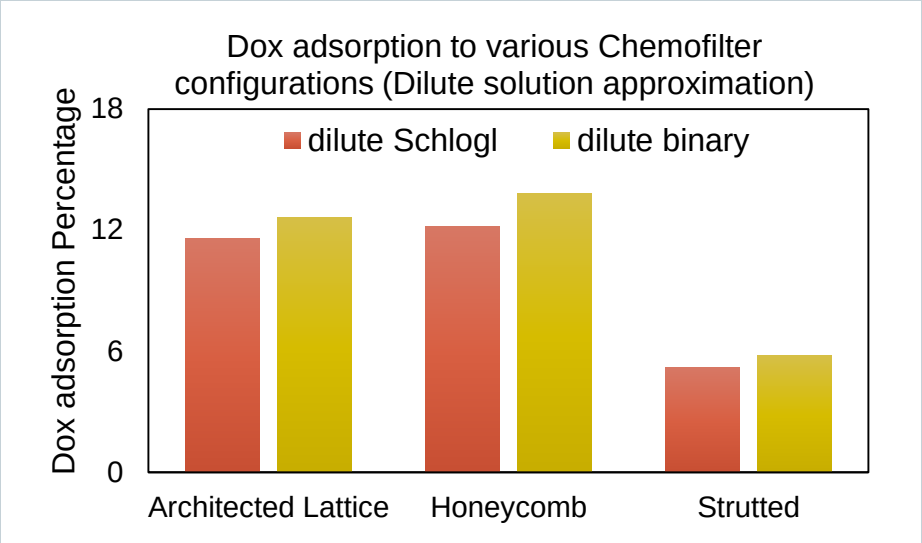

Figure 4-3 Dox concentration reduction based on different solution assumptions for a) non-porous honeycomb configuration, b) architected lattice of Chemofilter basket, c) non-porous strutted configuration.

4.4.3 Model 3

The qualitative transport and binding of Dox through different configurations of the Chemofilter is shown in Figure 4-4. These results are obtained based on the experiments on SEO polymer electrolyte [87], due to lack of experimental results for Dox solution in plasma. The approximated effective diffusion coefficient for SEO polymer electrolyte was about 65 times larger than that of the passive diffusion coefficient. The overall reduction of the Dox concentration in blood for the honeycomb Chemofilter, the architected lattice of the Chemofilter basket, and the strutted Chemofilter were predicted to be 80.56%, 82.96%, and 43.28%, respectively.

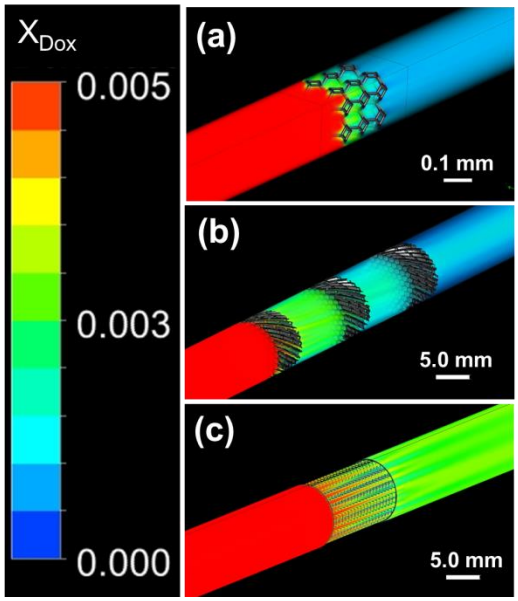

Figure 4-4 The qualitative representation of Dox transport and binding based on concentrated solution theory, through (a) a 2x2 matrix of the architected lattice that forms the Chemofilter basket, (b) the honeycomb Chemofilter, (c) the strutted Chemofilter. (the results are obtained based on experiments on SEO copolymer electrolyte [87])

4.5 Discussion

4.5.1 Model 1

This study was conducted in order to develop a computational model accounting for the binding of Dox to the Chemofilter surface. The modeling was guided by the results of the porcine *in vivo* studies performed at UCSF, which is reported by Oh *et al.* [24]. In order to achieve this goal, the material balance equation was derived, where the effect of ions migration was accounted for by an effective diffusion coefficient, D_{eff}. In the first model that was presented in this study, the binding of Dox to the surface of the Chemofilter was modeled for different constant diffusion coefficients in order to estimate the order of magnitude of D_{eff} which would result in a close match between these computational predictions and the experiments. The results presented in Figure 4-1 (a) show a marginal filtration performance with utilizing the passive diffusivity of Dox in the material balance equation, thus suggesting that the dominant binding mechanism is due to the electrochemical attraction of the ions towards the surface. By increasing the order of magnitude of the diffusion coefficient (shown in Figure 4-1 b and c), the predicted binding performances matched closer to the experimental data. The study by Maani *et al.* [77]

showed that the Peclet number should be in the order of 500 to match the binding performance observed in the animal studies.

4.5.2 Model 2

The electrochemistry of a dilute electrolyte is well-established and is expressed with Nernst-Plank equations. Therefore, in model 2 of the study, the binding performance of the Chemofilter was examined with the dilute solution approximations. In Figure 4-2 the reduction of Dox in plasma is presented for a non-binary solution of Dox, which shows that the dilute solution approximation results in a very low binding of Dox to all Chemofilter configurations. In this model, the effective diffusion coefficient was a function of concentration as shown in Figure 4-2 (c). Therefore, D_{eff} was lower in the near-wall region, where Dox particles were being adsorbed to the wall and thus eliminated from the domain.

The predicted binding performance slightly improved when using binary solution approximations relative to that of the non-binary, as shown in Figure 4-3. The higher performance of the binary approximation can also be explained by the fact that with the binary approximation, there is only one cation (Dox) in the solution and its binding to the anionic surface of the Chemofilter is a one-step reaction. In the non-binary approximation, however, the binding consists of two reactions; 1) dissociation of sodium from the surface, and 2) reaction of Dox with the surface. The two-step reaction makes the binding process slower as the sodium ion from the surface are being replaced by Dox, which results in lower overall binding performance. It is worth to mention that for the architected lattice, the length scale is one order of magnitude smaller that of the non-porous honeycomb or strutted configurations. Thus, the diffusion time scale and, therefore, the Peclet number is smaller, which results in greater adsorption. We note in passing that the comparable binding performance of Dox to the architected lattice and honeycomb (Figure 4-3) was achieved despite the fact that the surface area of honeycomb was about 8 times larger than that of the architected lattice, if the lattice was extended to cover the same cross section of the tube.

The architected lattice was designed to be 3D printed in the shape of the Chemofilter basket [76]. The CFD results showed the pressure drop of 320 Pa in the Chemofilter basket, where the surface area and thickness were 940 mm^2 and 0.3 mm, respectively. The pressure drop of the Chemofilter basket was comparable to that of the honeycomb, 391 Pa, while the surface

area and the length of the honeycomb were 4800 mm^2 and 17.4 mm. Design of the Chemofilter basket geometry was inspired by the RX-Accunet which is widely used in clinical practice. The honeycomb Chemofilter was also designed to be 3D printed with a flexible polymer which can be squeezed into a catheter for deployment. It is shown that the manufacturing of the honeycomb Chemofilter is more feasible, as its larger scale, e.g. thicker walls, provides more mechanical strength and safety in the application. In this study it was assumed that the Chemofilter surface had unlimited binding sites and the surface saturation was also neglected. In reality, the larger surface area of the Chemofilter reassures larger number of binding sites, which makes the honeycomb configuration a more desirable design than the Chemofilter basket or the strutted configuration.

4.5.3 Model 3

Comparing the dilute solution results against that of the experiments, it is clear that performance of the Chemofilter was underestimated with the dilute approximations and a different model was required for more accurate expression of the binding mechanism. Therefore, in model 3 of this study, the effective diffusion coefficient is derived with the concentrated solution approximation as presented in Eq. 4-15. Even though the experimental data on the transport coefficients of Dox-plasma solution was unavailable, the following relationship was implemented in the Chemofilter simulations for SEO polymer electrolyte [87] to estimate the binding performance. Based on the numbers presented by Villaluenga *et al.*, the effective diffusion of this system was$1.56x10^{-8}$ m^2/s, which was about 65 times that of its passive diffusion. In [87], the salt concentration in the electrolyte was higher than that of Dox in plasma, which magnified the effective diffusion coefficient. However, it can be assumed that the diffusion coefficient and migration of Dox particles is less interrupted in plasma compared to a polymer electrolyte, due to larger mean free path of blood as the solvent. We, therefore, assumed that the estimated result should be the same order of magnitude as the expected result in the Chemofilter modeling. Note that the effective diffusion coefficient in a concentrated solution is a function of Dox concentration. Consequently, D_{eff} is smaller near the wall, where Dox is being adsorbed to the surface and its concentration is decreasing. The adsorption results obtained with the concentrated solution were a closer match to those obtained from *in vivo* animal studies.

These results also confirmed the superiority of the honeycomb design to the strutted design, as predicted by Maani *et al.* [77].

4.6 Limitations and Future Work

The main limitation in this study was the lack of experimental results on the characterization of concentrated solution of Dox in plasma, and utilization of the electrochemical characterization of the SEO polymer electrolyte to examine the developed model. Besides, in the *in vivo* experiment the geometry and hemodynamics of vein and venal flow in the specific animal was not characterized. Therefore, the numbers in this study are based on the literature and clinical approximations.

The parallel strutted Chemofilter prototype was used in the *in vivo* study. However, based on the previous data, it is suspected that the strutted Chemofilters deployed in parallel in the vein are forming a negligible gap with the wall. Therefore, in this study we assumed that the performance of two small strutted Chmofilters deployed in parallel is the same as that of one single strutted Chemofilter, which is large enough to fit inside the vein without the gap.

Study of the porous Chemofilter basket is a two-scale problem due to the length scale difference between the microscale architected lattice and the macroscale basket-shape configuration [76]. In this study, only the microscale architected lattice was modeled and the macroscale modeling of the Chemofilter basket is one of the future directions for this study, once the mechanical strength of the 3D printed lattice is determined.

Another limitation of this study is the assumption of binary electrolyte in the development of the model, for its simplicity. In reality, plasma consists of various proteins and ionic components, and Dox may be surrounded or bound to these ionic particles, which affects the mechanism of binding.

4.7 Conclusion

A multiphysics modeling approach was developed to investigate the Dox transport and adsorption for different configurations of the Chemofilter device. The mathematical relationship for an effective diffusion coefficient was established based on three distinct solution approximations: 1) passive diffusion, 2) dilute solution, and 3) concentrated solution. The first

model was used in a preliminary study conducted to estimate the order of magnitude of the effective diffusion coefficient, D_{eff}, that would improve the agreement between the simulation and experimental results. The second model was based on the well-established Nernst-Plank equation for dilute solution. In the results obtained using the second model, the Dox binding performance was underestimated relative to that observed in the experiments. The third model was based on concentrated solution theory, which provides a more general platform for modeling an electrochemical system. The $D_{eff\text{-}cb}$ derived from the concentrated solution theory was calculated using experimental data for an SEO polymer electrolyte, as the experimental data for Dox was unavailable. The order of magnitude of concentration changes for these computational results obtained utilizing SEO copolymer electrolyte properties, corresponded with that for the porcine *in vivo* study. Therefore, we conclude that the concentrated solution approximation is the most accurate out of the three models considered for Dox transport and binding in the Chemofilter device.

CHAPTER 5. THE SHARK-SKIN EFFECT ON PLATELET ACTIVATION AND HEMODYNAMIC PERFORMANCE OF THE CHEMOFILTER: FROM HYDROPHOBICITY TO 'HAEMOPHOBICITY'

In the following study, we discuss how the surface micropattern affects liquid flow. One area of application of patterns in the liquid flow is the so-called 'shark-skin' effect. Shark-skin effect is one of the biomimetic surface examples, applied on immersed surfaces for controlling the drag force and facilitating the flow. Owing to the presence of micro-riblets (similar to those in the shark-skin scales) positioned parallel to the flow, the drag is reduced in the shark-skin patterned surface. Thus, the effect of the surface pattern can be substituted with an effective force. The shark-skin effect is well known for water flow; however, here we discuss a similar effect for blood flow in biomedical applications and introduce the concept of surface 'haemophobicity' (similar to hydrophobicity or oleophobicity, from the Greek root *haemo* meaning 'blood'). Owing to a properly tailored surface microstructure in a device such as the Chemofilter, blood adhesion and stagnation can be controlled and, therefore, the risk of thrombosis can be reduced significantly.

5.1 Methods

The goal in this part of the project was to design a blood-repelling surface for the Chemofilter in order to reduce the risk of thrombus formation. Therefore, we 1) optimized the riblet configuration, 2) determined the platelet activation close to the wall. In order to optimize the configuration of the shark-skin riblets, the flow in a microchannel with parallel, staggered, and continuous microriblets was modeled. Following this, the configuration which resulted in the largest drag reduction was applied to a tube surface to investigate its effect on the platelet activation. The maximum shear profile was calculated on the elements close to the wall, where the platelets reside. Based on the critical stress threshold found in the literature, the elements with activated platelets were located and marked to examine the effectiveness of shark-skin texturing.

5.1.1 Hemodynamic Performance Due to Riblet Configuration

A microchannel was patterned by riblets of different configurations and heights, placed on one of its walls, in order to study their effect on the near-wall flow. Symmetry boundary conditions were assigned to the side walls of the channel to eliminate their effect on the flow over the textured surface at the bottom. In the first step, the height of the riblet was optimized to reduce the amount of overall drag on the surface. In the next step, the flow of blood over the surface with continuous, parallel, and staggered configurations of riblets was simulated and the shear stress and drag in the channel were computed for each case in order to find the most effective configuration.

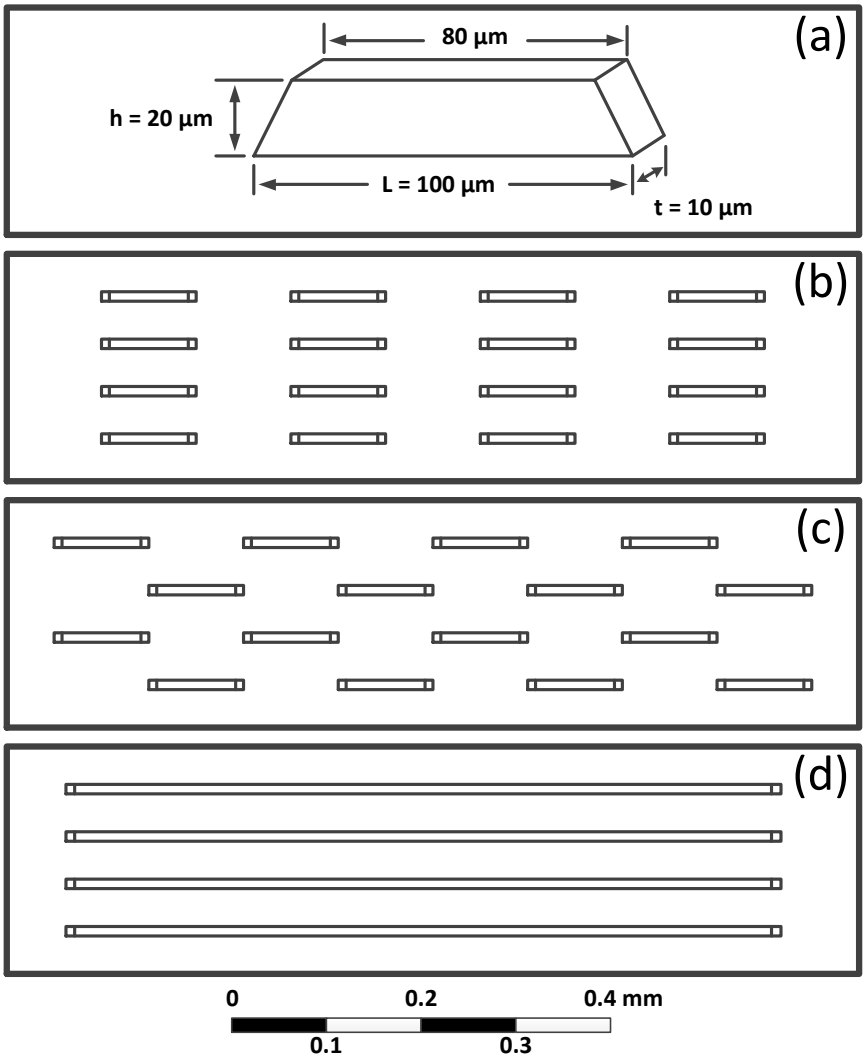

Figure 5-1 Different arrangement of riblets used in the CFD model; the top view of (a) a single riblet size, the arrangement of (b) aligned riblets, (c) staggered riblets, and (d) continuous riblets

The channel cross-section area was 0.5 mm × 0.8 mm, with the channel length of 1.7 mm; the rows of trapezoidal riblets were located in the region of fully-developed flow. Figure 5-1(a) shows the dimensions of a riblet, while the parallel, staggered and continuous riblet configurations are shown in 1(b), 1(c), and 1(d) respectively. In all configurations, each row of riblets was placed s=50 μm apart from the next one in the continuous and aligned configurations and s = 100 μm in the staggered configuration. These values correspond to the non-dimensional spacing values of $s^+ = 2.77$ and $s^+ = 5.54$ (the method for non-dimensionalising is described in [74]).

The flow domain was discretized with fully structured mesh generated with ANSYS ICEM CFD software; the finest mesh cell volume around the riblets was $1.5x10^{-17}$ m^3, and the whole channel contained 500,164 elements. The mesh was refined in the lower region of the channel to adequately resolve the flow around the riblets and in the boundary layer.

Blood was modeled as a non-Newtonian fluid using Herschel-Bulkley model, which accounts for the shear-thinning and yield stress properties of the blood. A constant flow velocity of 0.5 m/s (corresponding to Re = 227) was prescribed at the model inlet, and the outflow boundary condition was assigned to the outlet. The shear stress and drag force were computed in the boundary layer near the surface and around the riblets and their values were compared for simulations with different geometries, including a smooth surface and the alternative riblet configurations.

5.1.2 Platelet Activation Analysis

Platelet activation levels were investigated for a fully-developed blood flow in a tube with the microriblets on the inner surface. Platelet activation was assumed proportional to their adhesion and accumulation on the surface, thus correlated to the chance of thrombosis. Tube geometries were constant in all simulations, and flow regimes with high and low Reynolds number were considered. Human platelet activation thresholds vary between 7.5 Pa and 8.5 Pa [88]. In this work, the effect of the threshold values was investigated by determining platelet activation at the extremes of the threshold range. Previous activation models have been used to generate the shear stress and exposure time relationships as well as the resulting activation level. The output of this model included shear stress profiles and platelet activation levels based on the spatial distribution of shear stress.

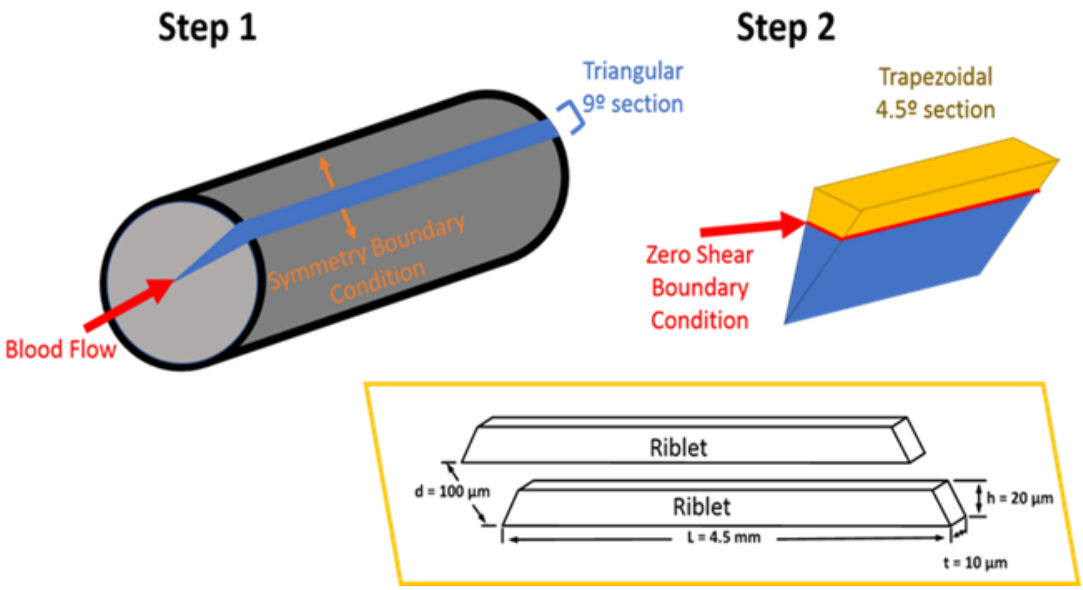

Figure 5-2 (Step 1) Schematic of the tube, showing the modeled section (blue triangle), boundary conditions (orange), and blood flow direction (red arrow). (Step 2) Trapezoidal section of tube (gold) with zero shear boundary condition (red). In set figure of micro-riblet structure (gold box)

The geometry of a tube was developed in SolidWorks, as shown in Figure 5-2. A nine-degree section of the tube was modeled with symmetry boundary conditions applied to the side walls to account for the entire tube. The angle had to be large enough to avoid complications on the acute area between the walls. The flow domain inside the tube was meshed with unstructured tetra elements, using ANSYS ICEM software. Several layers of prism elements were applied at the wall and around the riblets in order to resolve the flow in the boundary layer. Given that the domain had an acute angle, the density of the mesh was reduced around the center of the tube to avoid reversed flow in the solution.

Over 2.5 million unstructured elements were needed to fully resolve the flow in the tube section. To limit this number, the following assumptions were applied: (1) shear rate is negligible for platelet activation near the center of the tube, and (2) the majority of the platelet population in a vessel is located in the outer-third of the fluid domain, i.e. closest to the wall of the tube [89]. Given these assumptions, the tube outer-forth trapezoidal part of its 4.5º section was modeled as the focal domain for platelet activation analysis, depicted in Figure 5-2 (step 2). Structured mesh was used for discretizing the domain to reduce the number of elements to 0.5 million. Zero shear stress boundary condition was applied on the top wall of the trapezoid to mimic the flow in the

triangular section simulation. The velocity and shear profiles obtained in step 2 were compared with those found in step 1 to validate the results. The first layer of elements adjacent to the wall, in the trapezoidal domain, was set to 1-μm height (i.e. platelet diameter). The flow equations were solved with ANSYS Fluent and numerical results, including velocity gradients, were imported to MATLAB for further analysis.

Given that the viscous stress is the main parameter to consider in platelet activation, the ANSYS Fluent velocity profiles and Cartesian velocity gradients (L_{ij}) were used to calculate the Cauchy stress tensor ($T_{ij}; with\ i,j = 1\ to\ 3$) and scalar stress ($\tau_{max}$) in each element. Having the velocity gradient tensor ($L_{ij} = \frac{\partial u_i}{\partial x_j}$) obtained from Fluent, the rate of deformation and Cauchy stress tensor were calculated with,

$$D_{ij} = 1/2(L_{ij} + L_{ji}) \qquad \text{and} \qquad T_{ij} = 2\mu D_{ij} \tag{5.1}$$

where μ was Newtonian blood viscosity. Using the viscous shear stress, a scalar stress was calculated based on the formulation inspired by Von Mises stress, as outlined by Apel, *et al.*[90]

$$\tau_{max} = \left[\frac{1}{6}\sum_{i,j=1}^{3}(T_{ii} - T_{jj})(T_{ii} - T_{jj}) + T_{ij}T_{ij}\right]^{1/2} \tag{5.2}$$

By obtaining the maximum shear profile, the elements on which the stress was greater than the critical platelet activation threshold, 7.5-8.5 Pa [88] were located and marked to calculate the percentage of activated platelets. In this model, it was assumed that 1) all platelets within a given mesh volume will activate once the shear stress was greater than the activation threshold, 2) platelet concentration in the blood flow is homogeneous, and 3) the rate of platelet activation was proportional to the rate of platelet adhesion which consequently contributes to the platelet accumulation and thrombus formation on the wall. The platelet concentration in blood was set to 4.5×10^{11} platelets/m^3 [91]. The results are then compared with those obtained for a control tube model without any microstructure, in order to evaluate the effect of the shark-skin on platelet activation.

The tube had a 5 mm diameter and was 7.5 mm long. The micro-riblets were 4.5-mm long, located 2.8 mm from the inlet of the tube. The riblet height and the distance between the riblets were 20 μm and 100 μm, respectively. The configuration of micro-riblets was such that two riblets, in parallel, were evenly spaced along the wall of the tube (Figure 5-1(d), and Figure 5-6 (c)). Since the tube was not long enough for the blood flow to fully develop before reaching

the riblets, a preliminary flow simulation was carried out to obtain a fully-developed outlet velocity profile, which was then used as the inlet for the following simulations. The height of the trapezoidal domain close to the wall was 0.6 mm. Two velocity values, 0.5 m/s and 1 m/s, corresponding to the Re = 757 and Re = 1514, were used for the simulations. Blood density and viscosity were set to 1060 kg/m3 and 0.0035 kg/ms, respectively. The Reynolds numbers indicated the flow was laminar.

5.1.3 Dox Mass Transfer and Binding

The mass transfer and binding of Dox particles were investigated in the hexagonal channels of a plain honeycomb Chemofilter, with 5.8 mm length and 0.9 mm diameter, where each side of the channel was covered with four continuous riblets of the optimized dimensions, mentioned above. The inlet velocity was varied between 0.02 and 0.2 m/s, to account for the difference in the inlet velocity of each channel based on their location in fully developed parabolic venous flow (for the upstream velocity of 0.1 m/s). The heat/mass transfer analogy was utilized in these simulations, where the thermal diffusivity of Dox was set to that of water to match the simulations in [77].

5.2 Results

5.2.1 Hemodynamic Performance of the Microchannels Due to Riblet Configuration

The presence of riblets on the microchannel wall results in the drag reduction on the flat plate, by introducing a zone with lower shear stress. Therefore, by texturing the surface, we transport the high shear stress to the riblet’s top and front edges. The contours of the shear stress are shown in Figure 5-3 where the shear stress is minimum in the valleys around the riblets, while the highest wall shear stress (WSS) is observed at the edges of the riblets.

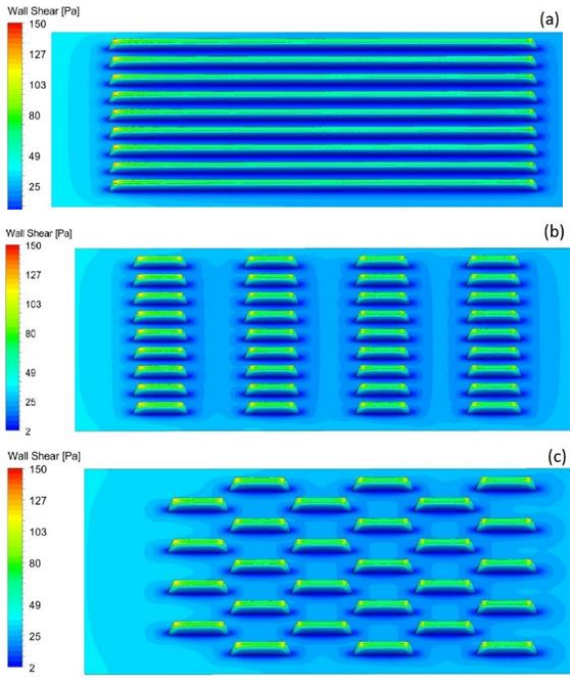

Figure 5-3 The shear stress distribution on the wall with (a) continuous riblets (b) aligned riblets (c) staggered riblets

In order to optimize the riblet height, several simulations were performed with the continuous riblets of varying heights (h = 10-60 μm, or non-dimensional h^+ = 0.554-3.325) and also with the smooth surface, and the drag force on the wall was calculated. The results are depicted in Figure 5-4, where the x and y axis show the riblet height and the drag force on the wall respectively. We observe that the minimum drag force is achieved when the height is 20 μm (h^+ = 1.113).

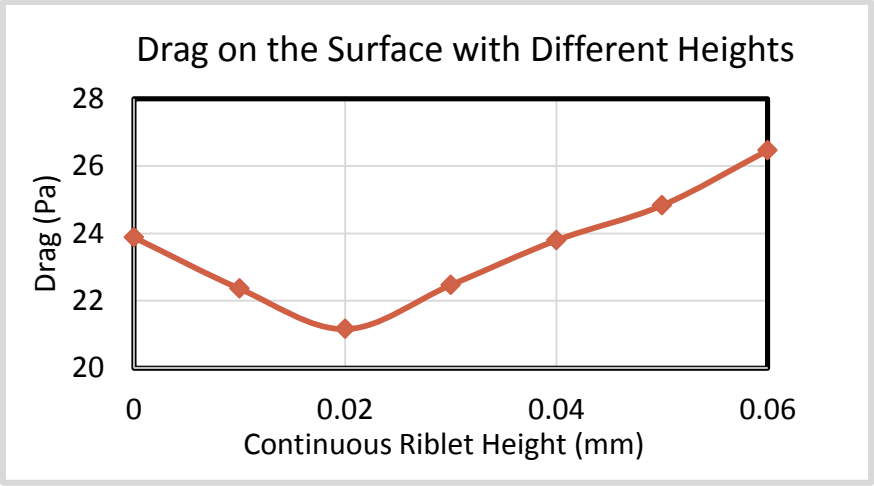

Figure 5-4 The drag on the surface of the channels with different riblet heights

It is interesting that while the overall drag increases with height for the riblet higher than 20 μm, the minimum shear stress continues to decrease. The reason is that the increased riblet height provides more space for the flow in the valleys between the riblets, which results in the lower momentum transfer and in a decrease of the shear stress. However, the leading edge of the riblet acts like an obstacle to the flow which is associated with both the higher friction and pressure drag. Thus, the pressure drag increased by 260% while the viscous drag only decreases by 14% when the riblet height increases from 20 to 60 μm. Therefore, the optimum height provides the minimum overall shear stress between the riblets (low shear zones) and on their edges (high shear zones).

In the next step, the overall WSS along a line passing through the zone between the riblets (along the red line shown on Figure 5-5) was calculated for the optimum height of h = 20 μm. On Figure 5-5, the x-axis is in the direction of the flow showing the section of the channel which contains the riblets and the y-axis shows the shear stress. Note that the section of the channel corresponding to the onset of the boundary layer is smooth. To study the effectiveness of the riblets, the shear stress and drag forces presented in here exclude the entrance region. The wall shear stress over a line on the smooth surface is uniform and is also greater than that for the patterned walls.

On the wall with continuous riblets the shear stress is uniform and the smallest of all considered cases. The shear stress fluctuates on the wall with aligned riblets, since there is a repeating pattern of riblets and smooth zones along the flow with the minimum shear stress observed in the valleys between the riblets. The staggered riblet pattern produces higher line shear stress than the parallel riblets. The same trend can be observed when calculating the overall average shear stress on the riblets with exclusion of the flat surface. The average shear stresses on the riblets are $\tau_{continuous} = 30.29$ Pa $< \tau_{staggered} = 38.88$ Pa $< \tau_{aligned} = 39.64$ Pa. In this study we observe that by patterning the wall with riblets, up to 6% drag force reduction is achieved while the surface area is increased by 25.4%.

These shear stresses are the highest stresses on the patterned surfaces while on the smooth surface the average shear stress is 44.035 Pa, which is still higher than the peak stress on the riblets. Therefore, we can conclude that the shark-skin pattern is effective for drag reduction in the blood flow and the continuous riblet configuration is the most effective one. The shark-skin effect is usually studied for turbulent flows around fast moving objects, as it was originally

inspired by the skin patterns of fast-swimming sharks which allow them to reduce the drag force. However, in this work, it is applied to a laminar flow of blood in a microchannel [79, 92].

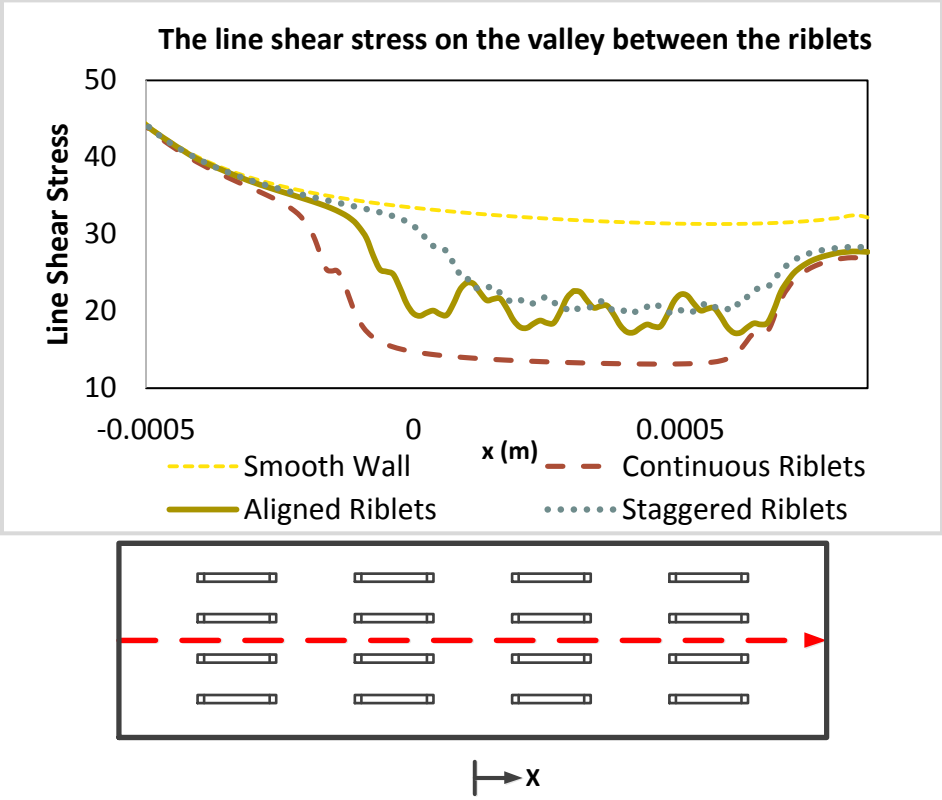

Figure 5-5 The comparison of the line shear stress distribution on the valleys between the riblets and the schematics of the aligned riblet configuration

5.2.2 Platelet Activation Analysis

In order to study the platelet activation, the flow was simulated in a tube with the optimum riblet configuration determined in the previous section (continuous micro-riblets with the height of 20 μm). Four different simulations were conducted to study platelet activation: (1) smooth tube, low velocity; (2) smooth tube, high velocity; (3) textured tube, low velocity; (4) textured tube, high velocity. The flow was solved to obtain the shear stress on the riblets, Figure 5-6 (d,e) showing the maximum shear stress on their tips. In the analysis of the results, two platelet activation thresholds were considered to account for the high (8.5Pa) and low (7.5Pa) thresholds of activation. The flow regions where the shear stress exceeded the threshold were deemed 'activated,' and the corresponding number of the activated platelets was calculated.

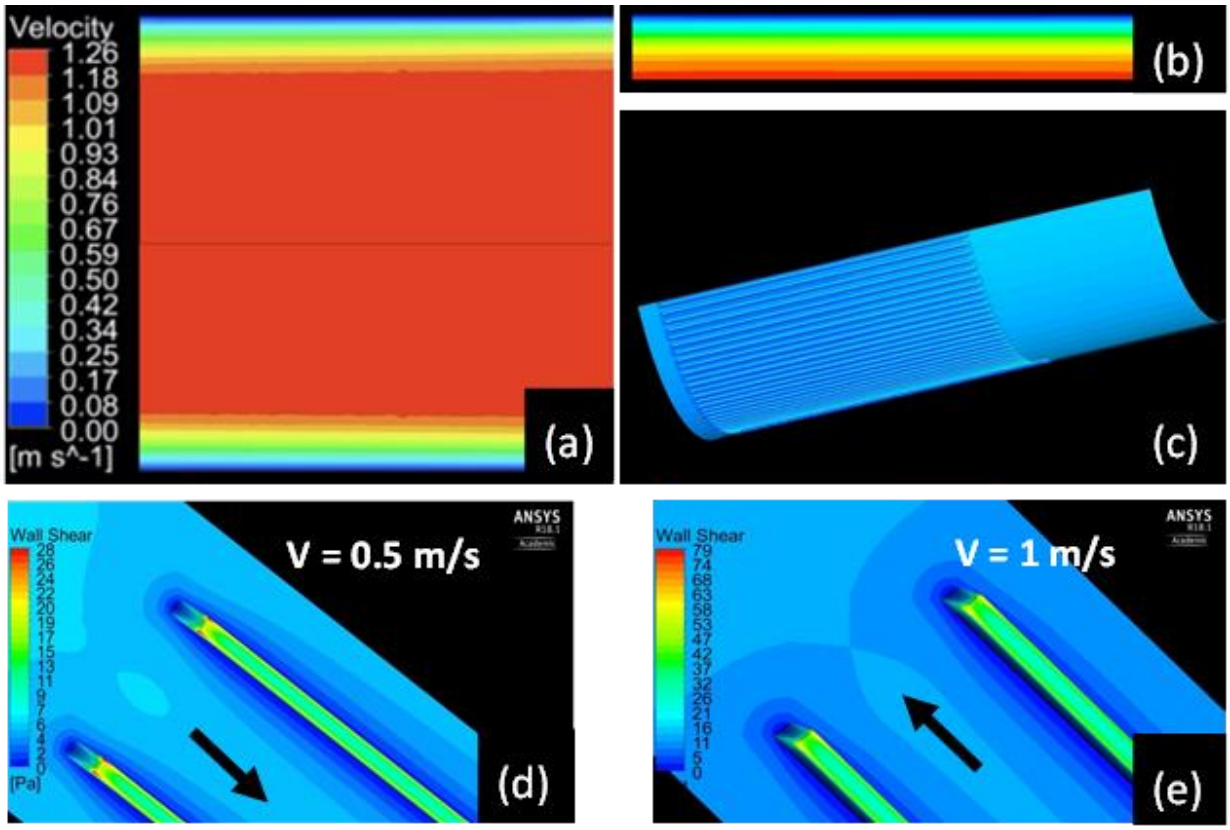

Figure 5-6 (a) Fully developed fluid flow levels inside the textured tube in step 1, (b) step 2, (c) Representation of continuous microriblets on a tube section. (d) shear profile for low velocity conditions, contours of shear stress on the patterned wall, demonstrating low shear stress on the flat surface and high shear stress on the riblets' top surface and tips, (e) Outlet shear profile for high velocity conditions

As expected, platelet activation levels increased with the inlet velocity for the both types of tube. Interestingly, the case of a smooth tube with low velocity resulted in zero percent activation. The faster flow in a 7mm tube caused 1.76% and 0.011% activation, corresponding to 503 and 3 activated platelets for the lower and higher thresholds respectively. Ribletted tubes exhibited low activation levels for low velocity and higher activation for increased velocity values. At the lower threshold, 2.47% of the platelets in the tube were activated, whereas high threshold activated 0.7% of platelets. In addition to the general trend of increasing activation with increasing velocity, the average shear stress levels along the surface increased. However, the average shear stress decreased after micro-riblets were added to the inner surface. The average shear stress on the wall of the smooth tube was 4.8 Pa and 13.08 Pa, compared to 4.02Pa and 10.96 Pa in the ribbletted tube, for the low and high velocity, respectively. This is consistent

with Figure 5-6 (d,e) where there is a shift of maximum shear stress to the micro-riblets, rather than the wall surface. Our simulation results did not support the hypothesis that the application of micro-riblets to a blood-contacting surface would reduce the risk of clotting. The addition of the riblets increased the percentage of platelet activation for all flow regimes. At high velocity, there were about 200 more platelets activated per tube fragment. Platelet activation was localized around the micro-ribelts, as shown in Figure 5-7.

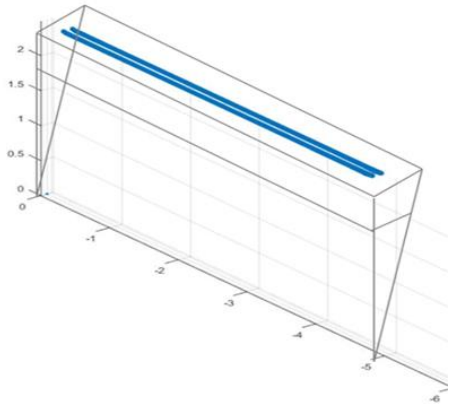

Figure 5-7 Spatial location of activated platelets (blue dots) in ribletted, high velocity flow simulation (Blue regions correspond with tips of riblets)

As shown in Table 5-1 Platelet activation levels for smooth and textured tubes, the average shear stress on the wall is reduced by 16% by applying the riblets. The results suggest that platelet activation due to altering geometry is more important at higher Reynolds numbers, while at lower Reynolds number, the platelet activation is negligible. The shark-skin effect introduces areas of low shear stress on the flat surface and between the riblets, Figure 5-6 (e,f). This effect is due to the transport of the higher shear stress to the riblet's tip and away from the surface. The sharpness of the riblet's tip is responsible for formation of the area of concentrated high shear stress on the riblets' edge. Therefore, we suspect that by modifying the tip's geometry (e.g. applying curved tip) the platelet activation will be reduced.

Table 5-1 Platelet activation levels for smooth and textured tubes

Total platelet counts in whole tube = 28,624 platelets. (Total volume = 6.36 x 10^{-8} mm^3, platelet concentration = 4.5 x 10^{11} platelets / mm^3)								
	Smooth Tube				**Textured Tube**			
	Low Velocity v = 0.5m/s Re = 757		High Velocity v = 1m/s Re = 1514		Low Velocity v = 0.5m/s Re = 757		High Velocity v = 1m/s Re = 1514	
Average WSS	4.8 Pa		13.08 Pa		4.022 Pa		10.96 Pa	
Platelet Activation Threshold	7.5 Pa	8.5 Pa	7.5 Pa	8.5 Pa	7.5 Pa	8.5 Pa	7.5 Pa	8.5 Pa
% Platelet Activation	0.0000	0.0000	1.7600	0.0110	0.0046	0.0024	2.4700	0.7000
# of Activated Platelets	0	0	503	3	1	0	707	200

5.2.3 Dox Mass Transfer and Binding

Figure 5-8 shows that the temperature drop (analogous to Dox concentration reduction which defines the binding performance) in the honeycomb Chemofilter increased when the surface of the channels were textured with the shark-skin inspired riblets. The temperature drop was greater in the textured channels closer to the center of the vessel, characterized by larger velocity. At the same time, the temperature drop decreased with the larger Peclet numbers, which corresponded to increased advective velocity. The percentage of improvement in binding of ribletted surface ranges from 0.7% to 3.5% in individual channels, which on average amounted to a 2.0% overall improvement in the plain honeycomb.

The impact of surface texturing on the binding performance of the channels with larger advection was due to the alteration of the flow in the valleys between the riblets. The lower momentum in these valleys promoted larger residence time and greater binding. However, for the low velocity channels the residence time was already sufficiently high and, subsequently, the effectiveness of the riblets decreased. Using the same reasoning, we can predict greater impact of texturing in the twisted and perforated honeycomb configuration, where the riblets provide larger residence time while the whole flow is imposed to more mixing.

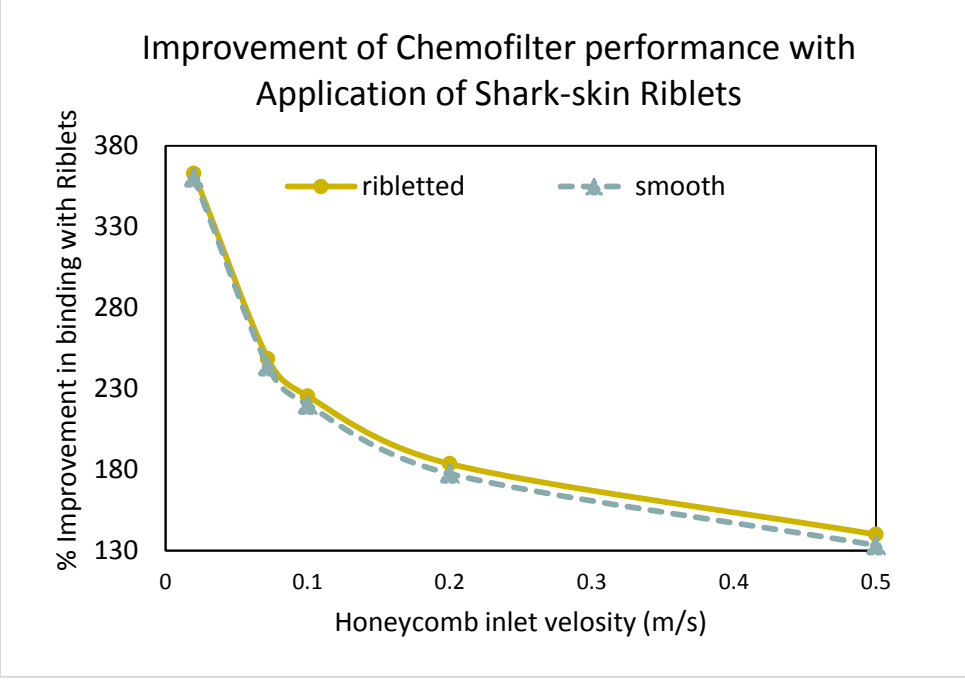

Figure 5-8 The binding performance of the Chemofilter with application of the shark-skin riblets

5.3 Conclusion

To recap, microriblets can facilitate blood flow by reducing the shear stress and drag force on the wall but they may have adverse effects on thrombus deposition potential. In this study, the near-wall hemodynamics and platelet activation was investigated. The tube surface was textured with parallel continuous riblets and placed in laminar flow at the Reynolds numbers of 757 and 1514. The high Reynolds numbers were chosen to examine the thresholds at which the platelets are activated. Even though our primary hypothesis was not supported in this model, it should be noted that the presented velocity range is much higher than the velocity range in hepatic veins (Re<300).

It should be noted that a high dose of anticoagulation drugs such as heparin is commonly used during the IAC procedure, thus reducing the chance of thrombosis. In addition, application of textured surface will provide low shear stress areas with higher residence time between the riblets adjacent to the wall. Contact area is also increased 19% which provides more drug absorption sites along the flow. Besides, there are other parameters such as flow residence time that will contribute to platelet activation that are not included in this model.

CHAPTER 6. SUMMARY AND CONCLUSION

6.1 Summary of the Project

In this study, CFD modeling was used to develop an optimized configuration for the Chemofilter device for filtering excessive chemotherapy drugs from blood. This project involved the following specific tasks: 1) defining the flow conditions and identifying the constraints imposed on the design; 2) developing models for alternative configurations of the device; 3) evaluating hemodynamic performance and resulting drug concentration reduction for the developed configurations and optimizing the design; 4) comparing computational predictions with *in vivo* results.

The Chemofilter is to be deployed from a catheter in the hepatic vein or IVC during the IAC procedure in order to chemically adsorb the drugs. The low pressure in the vein imposes the first design restriction, i.e. the limitation on the pressure drop through the device. Blood flow in these vessels is laminar and can be assumed to be steady state. The proposed configurations should result in minimal disturbance to the flow in order to avoid stagnation. In order to reduce the risk of blood clot formation, administration of a high dose of anticoagulation drugs, e.g. heparin, is suggest during the time that the Chemofilter is deployed in the vein. Also, the size of the Chemofilter pores should be large enough to warrant a safe passage of cells in the blood, e. g. RBCs with an average diameter of 8μm.

Porous Chemofilter basket (Chapter 2): A design using a microscale architected material (tetradecahedron microcells) was suggested by Greer's lab (California Institute of Technology). A porous membrane consisting of a lattice of microcells can be installed on umbrella-shaped Nitinol frame, thus forming a basket. The microcell size was set in the order of 100 μm to allow the passage of RBCs through them, and the basket shape was inspired by RX- Accunet device, for the ease of deployment. The porous lattice provided a large surface area for drug binding in a compact form, while the adsorption was facilitated due to the small length scales (resulting in a small Pectel number). Development of the Chemofilter basket was the result of design iterations to characterize the device's hemodynamic performance as a function of microcell size and number of micro-cell layers forming the membrane, as well as the effect of the tip angle in various macroscale configurations. The macroscale design ranged from a parabolic to umbrella-

shape configurations with 4, 6, or 8 membrane sectors. Smaller microcell size enhanced the binding, while it had an adverse effect on the pressure drop. In macroscale, the acute tip angles of the membrane resulted in lower pressure drop but larger flow separation regions. For example, a pressure drop of 204 Pa was predicted for a Chemofilter basket with 40º tip angle which was made of 2 layers of 150 μm microcells. An important design point shown by the CFD models was the avoidance of gaps between the Chemofilter's membrane and the wall of the vein. For example, about 82% of the flow could escape unfiltered through the gaps if the lattice was not expanded to cover the basket's frame. In summary, the size of the microcells and the thickness of the lattice were decided by the maximum allowable threshold of the pressure drop in the venous flow. However, another restriction for usage of smaller microcell was due to the manufacturing limitations. The lattice of the Chemofilter basket was 3D printed and it was shown that the mechanical strength of the lattice decreases in smaller microcells, making the Chemofilter susceptible to tear.

Non-porous honeycomb Chemofilter (Chapter 3): The original honeycomb design consisted of parallel hexagonal channels with 0.45-0.90 mm range of diameter. The benefit of this configuration was the lower pressure drop across the unit length of the device and less flow disturbance, compared to the porous configuration. The enhanced hemodynamics was due to the larger size of channels and their alignment with the flow direction. However, the binding performance declined along the length of honeycomb channels due to the decrease in mixing with the development of the concentration boundary layer. The multiphysics CFD models were developed by utilizing the energy and mass transport analogy, after verifying that the results of both models were matching. In order to increase adsorption, the parallel channels were twisted and perforated to enhance the flow mixing and disturbing the boundary layer. A longer honeycomb unit provides greater residence time, thus allowing to increase binding, however the efficiency can be further improved by dividing the device into shorter stages arranged in series in order to avoid fully developed flow in the channels. Different design parameters were studied to optimize the honeycomb configuration, including: the channel diameter, the twist angle, the length, and the spacing between different stages of the Chemofilter. Subsequently, a sensitivity analysis was performed to rank the significance of the channel diameter, inlet flow velocity and effective diffusivity of Dox. The sensitivity analysis suggested the dominance of the effective diffusion coefficient in the final results. Computations showed a 44.6% improvement in the

binding performance of a 16 mm long, twisted and perforated honeycomb compared to the original plain configuration. The computational analysis of the alternative configurations led to the final honeycomb design which included three device stages of 5.8 mm length, perforated and twisted by 45º, with spacing larger than the length of each stage. The final honeycomb design was predicted to reduce the Dox concentration in blood by 66.8%, while staging also provided flexibility for deployment of the device.

Ionic binding and electrochemistry (Chapter 4): Of the three suggested binding mechanisms, the ion-exchange mechanism was investigated because the devices used in porcine *in vivo* experiments conducted by our collaborators utilized this mechanism. The multiphysics models for Dox transport and electrochemical binding was developed based on dilute and concentrated solution theory. An effective diffusion coefficient was derived to account for migration of ions using each of these models. Performance of the alternative honeycomb configurations was computationally compared against a strutted Chemofilter configuration used in the animal studies. The CFD model of the strutted Chemofilter predicted a 50% elimination of Doxorubicin which was supported by the *in vivo* experiments. The comparison of the honeycomb and strutted Chemofilters demonstrated the superior performance of the optimized honeycomb configuration, as evidenced by 57.4% improvement in drug concentration reduction.

Note that in modeling of the binding it was assumed that unlimited binding sites were available and that the adsorption was warranted for any particle that reached the vicinity of the surface of the device. However, the binding sites can become saturated during the IAC procedure resulting in performance decay. Therefore, the configuration with larger surface area is advantageous, as the number of binding sites is proportional to the surface area. Consequently, the honeycomb with over 5 times larger surface area was the configuration of choice in this study. The honeycomb is also the preferred configuration from the manufacturing stand point. With the current limitations for the 3D- printing, the non-porous honeycomb is shown to have greater mechanical strength compared to the porous architected lattice, making the former a pragmatic choice.

Surface texturing with shark-skin effect (Chapter 5): The effect of surface texturing with shark-skin inspired riblets was investigated on the overall Chemofilter performance. While the shear stress reduced on the textured surface and the surface area increased, its resulting platelet

activation and drug binding efficiency were negligible in the honeycomb Chemofilter deployed in the venous flow.

6.2 Limitations and Future Directions

The main limitation of this study was the limited number of animal studies to validate the computational results. Besides, insufficient imaging data obtained during the animal studies limited our knowledge about the orientation of the prototype relative to the vein as well as the blood velocity in the vein. Therefore, we guessed the orientation and used the velocities reported in the literature rather than that of the specific animal that was studied. The specific limitations encountered in each methodology and modeling is presented in a separate section for each chapter.

Design of the future *in vitro* studies with the honeycomb configuration and developing a protocol for examining the performance of honeycomb Chemofilter *in vivo*, will be one of the directions for the Chemofilter project. Besides, in this study only the ionic binding of Dox was investigated. In collaboration with our co-investigators at Caifornia Institute of technology, the DNA intercalation mechanism can be investigated. Subsequently, the *in vitro* studies will be a possible option.

APPENDIX

ELECTROCHEMISTRY

Dilute Solution

Substituting of Eq. 4-1 into Eq. 4-2 and neglecting the reaction term, the balance equation is expressed by Eq. A-1 and Eq. A-2, for the cation and anion in a binary dilute solution, respectively.

$$\frac{\partial c}{\partial t} + \mathbf{v} \cdot \nabla c = z_+ u_+ F \nabla \cdot \left(c \nabla \psi\right) + D_+ \nabla^2 c \quad \text{(A-1)}$$

$$\frac{\partial c}{\partial t} + \mathbf{v} \cdot \nabla c = z_- u_- F \nabla \cdot \left(c \nabla \psi\right) + D_- \nabla^2 c \quad \text{(A-2)}$$

By subtracting Eq. A-1 and Eq. A-2 the electrostatic potential, $\nabla\psi$, can be expressed in terms of concentration gradient, ∇c. The above substitution results in Eq. 4-5 which resembles the advection-diffusion equation, except that the diffusion coefficient is replaced with Eq. 4-6 for the binary dilute solution.

$$\frac{\partial c}{\partial t} + \mathbf{v} \cdot \nabla c = D_{eff} \nabla^2 c + \mathcal{R} \quad \text{(4-5)}$$

$$D_{eff-db} = \frac{z_+ u_+ D_- - z_- u_- D_+}{z_+ u_+ - z_- u_-} \quad \text{(4-6)}$$

Note that in this calculation it is assumed that $\nabla \cdot \mathbf{v} = 0$ (divergence-free velocity). In reality, the velocity in the advective term of flux is not divergence free and for the cation it is expressed as, $\mathbf{v} = \mathbf{v}_0 + \mathbf{v}_+$. Besides, the migration term is negligible due to the lack of external electrostatic potential in the blood flow. Thus, the balance equation reduces to:

$$\frac{\partial c_+}{\partial t} + \mathbf{v} \cdot \nabla c_+ = \nabla \cdot (D_+ \nabla c_+) - c_+ \nabla \cdot \mathbf{v}_+ \quad \text{(A-3)}$$

In Eq. A-3, the Dox velocity, $\mathbf{v}_+$, can be expressed in terms of mobility, $\mathbf{v}_+ = -z_+ u_+ F \nabla\psi$, and the second term on the RHS of Eq. A-3 will reduce to a term which resembles the first term in RHS of Eq. A-1. Therefore, in this study the overall effect of the ion's mobility is referred to induced migration, as it results in an induced potential.

In order to find a relationship between diffusion and mobility, the Nernst-Einstein relation, $D_i = RT\, u_i$, can be utilized with assumption of point charges. Therefore, the balance equation will reduce to:

$$\frac{\partial c}{\partial t} + \mathbf{v} \cdot \nabla c = D_+ \nabla \cdot \left(\frac{z_+ F c}{RT} \nabla \psi + \nabla c \right) \quad \text{(A-4)}$$

In the Schlogl study [84, 85] it is assumed that the flux of species from resin to the solution and vice versa is equal ($N_A + N_B = 0$), flux of anions is zero ($N_M = 0$), and concentration of cations in the resin and solution is equal to the anion concentration ($C_A + C_B = C_M$). With the above boundary condition, they derived the flux equation for the species A and B which are being exchanged between resin (r) and solution (s) described in Eq. 4-7 below

$$A_s^+ + B_r^+ \rightarrow A_r^+ + B_s^+ \quad \text{(4-7)}$$

as:

$$N_A = -D_A \left[\nabla C_A + \frac{C_A F}{RT} \nabla \psi_A \right] = -\frac{\mathbf{2D_A\,(C_A+C_B)}}{\left(\frac{D_A}{D_B}+\mathbf{1}\right)\mathbf{C_A}+\mathbf{2C_B}} \boldsymbol{\nabla C_A} \quad \text{(A-5)}$$

$$N_B = -D_B \left[\nabla C_B + \frac{C_B F}{RT} \nabla \psi_B \right] = -\frac{\mathbf{2D_B\,(C_A+C_B)}}{\left(\frac{D_B}{D_A}+\mathbf{1}\right)\mathbf{C_B}+\mathbf{2C_A}} \boldsymbol{\nabla C_B} \quad \text{(A-6)}$$

In this study, the same boundary condition was used in material balance equation (Eq. 4-2) and with some mathematical maanipulations, the Nernst-Plank equation was reduced to Eq. A-7 (for cation) and Eq. A-8 (for anion).

$$\frac{\partial C_A}{\partial t} + \vec{v} \cdot \nabla C_A = -\nabla \cdot \left[-\frac{2D_A\,(C_A+C_B)}{\left(\frac{D_A}{D_B}+1\right)C_A+2C_B} \nabla C_A \right] + \mathcal{R}_A \quad \text{(A-7)}$$

$$\frac{\partial C_B}{\partial t} + \vec{v} \cdot \nabla C_B = -\nabla \cdot \left[-\frac{2D_B\,(C_A+C_B)}{\left(\frac{D_B}{D_A}+1\right)C_B+2C_A} \nabla C_B \right] + \mathcal{R}_B \quad \text{(A-8)}$$

Equation A-7 resembles the advection-diffusion-reaction equation (Eq. 4-5), where the constant Diffusion coefficient is replaced with an effective Diffusion coefficient for the cation, of Eq. 4-8.

Concentrated Solution

In the concentrated solution, Eq (4-9) provides a linear combination of resistances instead of one resistance (that of solvent) and since the relative velocities are considered, the reference or mean velocity is not required. In the binary electrolyte, the flux equation for cation and anion can be expressed as [41]:

$$c_+ \nabla \mu_+ = K_{0+}(v_0 - v_+) + K_{+\,-}(v_- - v_+) \quad \text{(A-9)}$$

$$c_- \nabla \mu_- = K_{0-}(v_0 - v_-) + K_{+\,-}(v_+ - v_-) \quad \text{(A-10)}$$

where the drag force due to the friction between different species ($K_{ij} = \frac{RTc_ic_j}{c_T\mathfrak{D}_{ij}}$) is described in terms of Stefan-Maxwell diffusion coefficient $\mathfrak{D}_{ij}$. The diffusion coefficient of the salt (usually measured), is based on the gradient of the concentration and is related to the diffusion coefficient of electrolyte, $\mathfrak{D}$, by:

$$\mathrm{D} = \mathfrak{D}\frac{c_T}{c_0}\left(1 + \frac{dln\gamma_{+-}}{dlnm}\right) \tag{A-11}$$

where $\gamma_{+-}$the mean molar activity coefficient and m is the molality (moles of electrolyte per kg of solvent). The relationship between other diffusion coefficients are found in [87] as

$$\mathfrak{D}_{+0} = \frac{\mathfrak{D}}{2\,(1-t_+^0)} \tag{A-12}$$

$$\mathfrak{D}_{-0} = \frac{\mathfrak{D}}{2\,t_+^0} \tag{A-13}$$

$$\mathfrak{D}_{+-} = \left(\frac{c_T\,F^2\phi_c}{\kappa RT} - \frac{2c_T\,t_+^0(1-t_+^0)}{c_T\mathfrak{D}}\right)^{-1} \tag{A-14}$$

where t_+^0 is the cation transference number which defined as the fraction of the current carried by cation during the electrolysis. In other words, it can be expressed as the ratio of the mobility of the cation to the mobility of all ions in the system as shown in Eq. A-15.

$$t_+^0 = \frac{current\ carried\ by\ cation}{total\ current} = \frac{u_+}{\sum_{+,-}u_i} \tag{A-15}$$

The above relations can be used to derive the relationship for the effective diffusion coefficient of a binary concentrated solution, Eq. 4-15.

REFERENCES

[1] S. F. Altekruse, "Hepatocellular carcinoma incidence, mortality, and survival trends in the United States from 1975 to 2005," *Journal of Clinical Oncology*, vol. 27, no. 9, pp. 1485-1492, 2009, doi: 10.1200/JCO.2008.20.7753.

[2] A. Roche, "Trans-catheter arterial chemoembolization as first-line treatment for hepatic metastases from endocrine tumors," *European Radiology*, vol. 13, no. 1, p. 136, 2003.

[3] K. Stuart, "Chemoembolization in the Management of Liver Tumors," *Oncologist*, vol. 8, no. 5, pp. 425-437, 2003, doi: 10.1634/theoncologist.8-5-425.

[4] W. J. Hwu, "A clinical-pharmacological evaluation of percutaneous isolated hepatic infusion of doxorubicin in patients with unresectable liver tumors," *Oncology Research*, vol. 11, no. 11-12, p. 529, 1999.

[5] S. Curley *et al.*, "Complete hepatic venous isolation and extracorporeal chemofiltration as treatment for human hepatocellular carcinoma: A phase I study," *Annals of Surgical Oncology*, vol. 1, no. 5, pp. 389-399, 1994, doi: 10.1007/BF02303811.

[6] D. A. August, N. Verma, M. A. Vaerten, R. Shah, J. C. Andrews, and D. E. Brenner, "Pharmacokinetic evaluation of percutaneous hepatic venous isolation for administration of regional chemotherapy," *Surgical Oncology*, vol. 4, no. 4, pp. 205-216, 1995, doi: 10.1016/S0960-7404(10)80037-4.

[7] Y. Ku, "Efficacy of repeated percutaneous isolated liver chemoperfusion in local control of unresectable hepatocellular carcinoma," *Hepato-Gastroenterology*, vol. 45, no. 24, p. 1961, 1998.

[8] Y. Ku, "Induction of long-term remission in advanced hepatocellular carcinoma with percutaneous isolated liver chemoperfusion," *Annals Of Surgery*, vol. 227, no. 4, p. 519, 1998.

[9] Y. Ku, M. Tominaga, T. Iwasaki, T. Fukumoto, and Y. Kuroda, "Isolated hepatic perfusion chemotherapy for unresectable malignant hepatic tumors," *International Journal of Clinical Oncology*, vol. 7, no. 2, pp. 82-90, 2002, doi: 10.1007/s101470200011.

[10] Y. Ku, "Percutaneous isolated liver chemoperfusion for treatment of unresectable malignant liver tumors: technique, pharmacokinetics, clinical results," *Recent Results In Cancer Research. Fortschritte Der Krebsforschung. Progres Dans Les Recherches Sur Le Cancer*, vol. 147, p. 67, 1998.

[11] L. F. Porrata and A. A. Adjei, "The pharmacologic basis of high dose chemotherapy with haematopoietic stem cell support for solid tumours," (in eng), *Br J Cancer*, vol. 85, no. 4, pp. 484-9, Aug 17 2001, doi: 10.1054/bjoc.2001.1970.

[12] M. C. Walker, C. N. Parris, and J. R. Masters, "Differential sensitivities of human testicular and bladder tumor cell lines to chemotherapeutic drugs," *Journal of the National Cancer Institute,* vol. 79, no. 2, p. 213, 1987.

[13] H. E. Skipper *et al.*, "Implications of biochemical, cytokinetic, pharmacologic, and toxicologic relationships in the design of optimal therapeutic schedules," *Cancer chemotherapy reports,* vol. 54, no. 6, p. 431, 1970.

[14] M. Buijs, "Nonresectable hepatocellular carcinoma: long-term toxicity in patients treated with transarterial chemoembolization--single-center experience," *Radiology,* vol. 249, no. 1, p. 346, 2008, doi: 10.1148/radiol.2483071902.

[15] M. S. Aboian *et al.*, "In vitro clearance of doxorubicin with a DNA-based filtration device designed for intravascular use with intra-arterial chemotherapy," (in eng), *Biomed Microdevices,* vol. 18, no. 6, p. 98, Dec 2016, doi: 10.1007/s10544-016-0124-5.

[16] C. M. Alexander, M. M. Maye, and J. C. Dabrowiak, "DNA-capped nanoparticles designed for doxorubicin drug delivery," *Chem. Commun.,* vol. 47, no. 12, pp. 3418-3420, 2011, doi: 10.1039/c0cc04916f.

[17] C. M. Alexander, J. C. Dabrowiak, and M. M. Maye, "Investigation of the drug binding properties and cytotoxicity of DNA-capped nanoparticles designed as delivery vehicles for the anticancer agents doxorubicin and actinomycin D," *Bioconjugate chemistry,* vol. 23, no. 10, p. 2061, 2012, doi: 10.1021/bc3002634.

[18] A. L. Lewis, R. R. Taylor, B. Hall, M. V. Gonzalez, S. L. Willis, and P. W. Stratford, "Pharmacokinetic and Safety Study of Doxorubicin-eluting Beads in a Porcine Model of Hepatic Arterial Embolization," *Journal of Vascular and Interventional Radiology,* vol. 17, no. 8, pp. 1335-1343, 2006, doi: 10.1097/01.RVI.0000228416.21560.7F.

[19] T. B. Dougherty, J. A. Mikolajek, and S. A. Curley, "Safe anesthetic management of patients undergoing a novel method of treating human hepatocellular cancer," *Journal of Clinical Anesthesia,* vol. 9, no. 3, pp. 220-227, 1997, doi: 10.1016/S0952-8180(97)00031-7.

[20] A. Patel *et al.*, "Development and Validation of Endovascular Chemotherapy Filter Device for Removing High-Dose Doxorubicin: Preclinical Study," *J. Med. Devices,* vol. 8, no. 4, 2014, doi: 10.1115/1.4027444.

[21] D. K. Rana, S. Dhar, A. Sarkar, and S. C. Bhattacharya, "Dual intramolecular hydrogen bond as a switch for inducing ground and excited state intramolecular double proton transfer in doxorubicin: an excitation wavelength dependence study.(Report)," *Journal of Physical Chemistry A,* vol. 115, no. 33, pp. 9169-9179, 2011, doi: 10.1021/jp204165j.

[22] P. Agrawal, "Studies on self-aggregation of anthracycline drugs by restrained molecular dynamics approach using nuclear magnetic resonance spectroscopy supported by absorption, fluorescence, diffusion ordered spectroscopy and mass spectrometry," *European Journal Of Medicinal Chemistry,* vol. 44, no. 4, p. 1437, 2009, doi: 10.1016/j.ejmech.2008.09.037.

[23] P. Bilalis, L.-A. Tziveleka, S. Varlas, and H. Iatrou, "pH-Sensitive nanogates based on poly(l-histidine) for controlled drug release from mesoporous silica nanoparticles," *Polymer Chemistry,* 10.1039/C5PY01841B vol. 7, no. 7, pp. 1475-1485, 2016, doi: 10.1039/C5PY01841B.

[24] H. J. Oh *et al.,* "3D Printed Absorber for Capturing Chemotherapy Drugs before They Spread through the Body," *ACS Central Science,* vol. 5, no. 3, pp. 419-427, 2019, doi: 10.1021/acscentsci.8b00700.

[25] G. Bramaramba *et al.,* "Chemical and Physical Characteristics of Doxorubicin Hydrochloride Drug-Doped Salmon DNA Thin Films," *Scientific Reports,* vol. 5, 2015, doi: 10.1038/srep12722.

[26] X. C. Chen *et al.,* "Block Copolymer Membranes for Efficient Capture of a Chemotherapy Drug," *ACS macro letters,* vol. 5, no. 8, p. 936, 2016, doi: 10.1021/acsmacrolett.6b00459.

[27] M. W. Wilson *et al.,* "Hepatocellular carcinoma: regional therapy with a magnetic targeted carrier bound to doxorubicin in a dual MR imaging/ conventional angiography suite--initial experience with four patients," (in eng), *Radiology,* vol. 230, no. 1, pp. 287-93, Jan 2004, doi: 10.1148/radiol.2301021493.

[28] M. C. Mabray *et al.,* "In Vitro Capture of Small Ferrous Particles with a Magnetic Filtration Device Designed for Intravascular Use with Intraarterial Chemotherapy: Proof-of-Concept Study," *Journal of Vascular and Interventional Radiology,* vol. 27, no. 3, pp. 426-432, Mar 2016, doi: 10.1016/j.jvir.2015.09.014.

[29] Y. Tian, "Complexation and release of doxorubicin from its complexes with pluronic P85-b-poly(acrylic acid) block copolymers," *Journal Of Controlled Release: Official Journal Of The Controlled Release Society,* vol. 121, no. 3, p. 137, 2007.

[30] Y. Tian, M. K. C. Tam, T. A. Hatton, and L. Bromberg, "Titration Microcalorimetry Study: Interaction of Drug and Ionic Microgel System," ed, 2004.

[31] Y. Tian, P. Ravi, L. Bromberg, T. A. Hatton, and K. C. Tam, "Synthesis and aggregation behavior of pluronic F87/poly(acrylic acid) block copolymer in the presence of doxorubicin," *Langmuir : the ACS journal of surfaces and colloids,* vol. 23, no. 5, p. 2638, 2007, doi: 10.1021/la060780a.

[32] Y. Li, N. Taulier, A. Rauth, and X. Wu, "Screening of Lipid Carriers and Characterization of Drug-Polymer-Lipid Interactions for the Rational Design of Polymer-Lipid Hybrid Nanoparticles (PLN)," *An Official Journal of the American Association of Pharmaceutical Scientists,* vol. 23, no. 8, pp. 1877-1887, 2006, doi: 10.1007/s11095-006-9033-2.

[33] H. A. Santos, J. A. Manzanares, L. Murtomäki, and K. Kontturi, "Thermodynamic analysis of binding between drugs and glycosaminoglycans by isothermal titration calorimetry and fluorescence spectroscopy," *European Journal of Pharmaceutical Sciences,* vol. 32, no. 2, pp. 105-114, 2007, doi: 10.1016/j.ejps.2007.06.003.

[34] S. Daoud-Mahammed *et al.*, "Cyclodextrin and polysaccharide-based nanogels: entrapment of two hydrophobic molecules, benzophenone and tamoxifen," *Biomacromolecules,* vol. 10, no. 3, p. 547, 2009, doi: 10.1021/bm801206f.

[35] M. Biondi, "Investigation of the mechanisms governing doxorubicin and irinotecan release from drug-eluting beads: mathematical modeling and experimental verification," *Journal of Materials Science: Materials in Medicine,* vol. 24, no. 10, pp. 2359-2371, 2013.

[36] M. Biondi, S. Fusco, A. L. Lewis, and P. A. Netti, "New Insights into the Mechanisms of the Interactions Between Doxorubicin and the Ion-Exchange Hydrogel DC Bead T for Use in Transarterial Chemoembolization (TACE)," (in English), *Journal of Biomaterials Science-Polymer Edition,* Article vol. 23, no. 1-4, pp. 333-354, 2012, doi: 10.1163/092050610x551934.

[37] V. Boudy, N. Voute, D. Pradeau, and J. C. Chaumeil, "Adsorption of an ionizable drug onto microspheres: experimental and modeling studies," *International journal of pharmaceutics,* vol. 239, no. 1-2, p. 13, 2002, doi: 10.1016/S0378-5173(02)00033-9.

[38] M. Singh, J. A. Lumpkin, and J. Rosenblatt, "Mathematical modeling of drug release from hydrogel matrices via a diffusion coupled with desorption mechanism," *Journal of Controlled Release,* vol. 32, no. 1, pp. 17-25, 1994, doi: 10.1016/0168-3659(94)90221-6.

[39] A. S. o. H. S. Pharmacists, *AHFS Drug Information 2009*. Bethesda, MD, 2009.

[40] D. A. Fedosov, B. Caswell, A. S. Popel, and G. E. Karniadakis, "Blood Flow and Cell-Free Layer in Microvessels," *Microcirculation,* vol. 17, no. 8, pp. 615-628, 2010, doi: 10.1111/j.1549-8719.2010.00056.x.

[41] J. S. Newman, *Electrochemical systems*, 3rd ed.. ed. Hoboken, N.J.: Hoboken, N.J. : Wiley-Interscience, 2004.

[42] C. Tu and M. Deville, "Pulsatile flow of non-Newtonian fluids through arterial stenoses," *Journal of Biomechanics,* vol. 29, no. 7, pp. 899-908, 1996, doi: 10.1016/0021-9290(95)00151-4.

[43] F. R, "Viscosity of Blood in Narrow Capillary Tubes," vol. **96**, L. R, Ed., ed. *Am. J. Physiol.* , 1931, pp. 562-568.

[44] D. Sankar and U. Lee, "Two-phase non-linear model for the flow through stenosed blood vessels," *Journal of Mechanical Science and Technology,* vol. 21, no. 4, pp. 678-689, 2007, doi: 10.1007/BF03026973.

[45] D. Liepsch, "An introduction to biofluid mechanics—basic models and applications," *Journal of Biomechanics,* vol. 35, no. 4, pp. 415-435, 2002, doi: 10.1016/S0021-9290(01)00185-3.

[46] G. R. Cokelet, "The rheology of human blood," E. R. G. E. W. Merrill, Ed., ed: Massachusetts Institute of Technology, 1963.

[47] D. S. Sankar, "Non-linear mathematical models for blood flow through tapered tubes," *Applied Mathematics & Computation,* vol. 188, no. 1, pp. 567-583, 2007, doi: 10.1016/j.amc.2006.10.013.

[48] D. S. Sankar, "A non-Newtonian fluid flow model for blood flow through a catheterized artery—Steady flow," *Applied Mathematical Modelling,* vol. 31, no. 9, pp. 1847-1865, 2007.

[49] G. W. Scott Blair and D. C. Spanner, "introduction to biorheology," in *introduction to biorheology,* ed. Amsterdam New York: Amsterdam ; New York: Elsevier Scientific Publ. Co., 1974.

[50] G. D. O. Lowe, "Virchow's Triad Revisited: Abnormal Flow," vol. 33, no. 5-6, pp. 455-457, 2003.

[51] M. H. Kroll, J. D. Hellums, L. V. McIntire, A. I. Schafer, and J. L. Moake, "Platelets and shear stress," *Blood,* vol. 88, no. 5, p. 1525, 1996.

[52] Z. Ren, S. Wang, and M. Singer, "Modeling hemodynamics in an unoccluded and partially occluded inferior vena cava under rest and exercise conditions," *Medical & Biological Engineering & Computing,* vol. 50, no. 3, pp. 277-287, 2012, doi: 10.1007/s11517-012-0867-y.

[53] G. M. Siewiorek, "Computational modeling of distal protection filters," *Journal of Endovascular Therapy,* vol. 17, no. 6, pp. 777-789, 2010, doi: 10.1583/10-3178.1.

[54] M. A. Singer, "Computational modeling of blood flow in the TrapEase inferior vena cava filter," *Journal Of Vascular And Interventional Radiology: JVIR,* vol. 20, no. 6, p. 799, 2009, doi: 10.1016/j.jvir.2009.02.015.

[55] M. A. Singer, "Modeling blood flow in a tilted inferior vena cava filter: does tilt adversely affect hemodynamics?," *Journal Of Vascular And Interventional Radiology: JVIR,* vol. 22, no. 2, p. 229, 2011, doi: 10.1016/j.jvir.2010.09.032.

[56] E. Previtali, P. Bucciarelli, S. M. Passamonti, and I. Martinelli, "Risk factors for venous and arterial thrombosis," in *Blood Transf.* vol. 9, ed, 2011, pp. 120-138.

[57] M. Hedayat, H. Asgharzadeh, and I. Borazjani, "Platelet activation of mechanical versus bioprosthetic heart valves during systole," *Journal of Biomechanics*, vol. 56, pp. 111-116, 2017, doi: 10.1016/j.jbiomech.2017.03.002.

[58] Y. S. Chatzizisis, A. U. Coskun, M. Jonas, E. R. Edelman, C. L. Feldman, and P. H. Stone, "Role of Endothelial Shear Stress in the Natural History of Coronary Atherosclerosis and Vascular Remodeling: Molecular, Cellular, and Vascular Behavior: Molecular, Cellular, and Vascular Behavior," *Journal of the American College of Cardiology*, vol. 49, no. 25, pp. 2379-2393, 2007, doi: 10.1016/j.jacc.2007.02.059.

[59] S.-H. Yun, E.-H. Sim, R.-Y. Goh, J.-I. Park, and J.-Y. Han, "Platelet Activation: The Mechanisms and Potential Biomarkers," *BioMed Research International*, vol. 2016, 2016, doi: 10.1155/2016/9060143.

[60] P. A. Holme, "Shear-induced platelet activation and platelet microparticle formation at blood flow conditions as in arteries with a severe stenosis," *Arteriosclerosis, Thrombosis, And Vascular Biology*, vol. 17, no. 4, p. 646, 1997.

[61] D. Bluestein, L. Niu, R. Schoephoerster, and M. Dewanjee, "Fluid mechanics of arterial stenosis: Relationship to the development of mural thrombus," *Annals of Biomedical Engineering*, vol. 25, no. 2, pp. 344-356, 1997, doi: 10.1007/BF02648048.

[62] Y. Alemu, "Flow-induced Platelet Activation and Damage Accumulation in a Mechanical Heart Valve: Numerical Studies," *Artificial Organs*, vol. 31, no. 9, pp. 677-689, 2007, doi: 10.1111/j.1525-1594.2007.00446.x.

[63] J. S. Soares, J. Sheriff, and D. Bluestein, "A novel mathematical model of activation and sensitization of platelets subjected to dynamic stress histories," *Biomechanics and Modeling in Mechanobiology*, vol. 12, no. 6, pp. 1-15, 2013, doi: 10.1007/s10237-013-0469-0.

[64] R. C. Starling *et al.*, "Unexpected Abrupt Increase in Left Ventricular Assist Device Thrombosis," *The New England Journal of Medicine*, vol. 370, no. 1, pp. 33-40, 2014, doi: 10.1056/NEJMoa1313385.

[65] Y. Miyazaki *et al.*, "High shear stress can initiate both platelet aggregation and shedding of procoagulant containing microparticles," *Blood*, vol. 88, no. 9, p. 3456, 1996, doi: 10.1080/00039896.1996.9934428.

[66] P. Fratzl and R. Weinkamer, "Nature's hierarchical materials," *Progress in Materials Science*, vol. 52, no. 8, pp. 1263-1334, 2007, doi: 10.1016/j.pmatsci.2007.06.001.

[67] M. Nosonovsky and B. Bhushan, "Surface self-organization: From wear to self-healing in biological and technical surfaces," *Applied Surface Science*, vol. 256, no. 12, pp. 3982-3987, 2010, doi: 10.1016/j.apsusc.2010.01.061.

[68] S. Kim, J. Lim, Y. Jung, C. Mun, J. Kim, and S. Kim, "Preparation of enhanced hydrophobic poly(L-lactide-co-epsilon-caprolactone) films surface and its blood compatibility," *Appl. Surf. Sci.,* vol. 276, no. C, pp. 586-591, 2013, doi: 10.1016/j.apsusc.2013.03.137.

[69] L. Chen, D. Han, and L. Jiang, "On improving blood compatibility: From bioinspired to synthetic design and fabrication of biointerfacial topography at micro/nano scales," *Colloids and Surfaces B: Biointerfaces,* vol. 85, no. 1, pp. 2-7, 2011, doi: 10.1016/j.colsurfb.2010.10.034.

[70] R. Liu, Y. Qin, H. Wang, Y. Zhao, Z. Hu, and S. Wang, "The in vivo blood compatibility of bio-inspired small diameter vascular graft: effect of submicron longitudinally aligned topography.(Report)," *BMC Cardiovascular Disorders,* vol. 13, no. 1, 2013, doi: 10.1186/1471-2261-13-79.

[71] K. Chung, J. Schumacher, E. Sampson, R. Burne, P. Antonelli, and A. Brennan, "Impact of engineered surface microtopography on biofilm formation of Staphylococcus aureus," *Biointerphases,* vol. 2, no. 2, pp. 89-94, 2007, doi: 10.1116/1.2751405.

[72] D. Bechert, M. Bruse, W. Hage, J. Vanderhoeven, and G. Hoppe, "Experiments on drag-reducing surfaces and their optimization with an adjustable geometry," *J. Fluid Mech.,* vol. 338, pp. 59-87, 1997.

[73] S. J. Lee and S. H. Lee, "Flow field analysis of a turbulent boundary layer over a riblet surface," *Experimental Methods and their Applications to Fluid Flow,* vol. 30, no. 2, pp. 153-166, 2001, doi: 10.1007/s003480000150.

[74] B. Dean, "Shark-skin surfaces for fluid-drag reduction in turbulent flow: a review," *Philosophical Transactions. Series A, Mathematical, Physical, And Engineering Sciences,* vol. 368, no. 1929, p. 4775, 2010, doi: 10.1098/rsta.2010.0201.

[75] S. Martin and B. Bhushan, "Fluid flow analysis of continuous and segmented riblet structures," *RSC Adv.,* vol. 6, no. 13, pp. 10962-10978, 2016, doi: 10.1039/c5ra20944g.

[76] N. Maani, S. W. Hetts, and V. L. Rayz, "A two-scale approach for CFD modeling of endovascular Chemofilter device," *Biomechanics and Modeling in Mechanobiology,* journal article vol. 17, no. 6, pp. 1811-1820, December 01 2018, doi: 10.1007/s10237-018-1058-z.

[77] N. Maani, T. Diorio, S. Hetts, and V. Rayz, "Computational Modeling of Drug Transport and Mixing in the Chemofilter Device: Enhancing the Removal of Chemotherapeutics from Circulation," *Biomechanics and Modeling in Mechanobiology,* [Under Review]

[78] N. Maani, S. Hetts, and V. Rayz, "Electrochemistry of Dox Binding to the Ion-Exchange resin: an Effective Diffusion Coefficient to Account for Ionic Migration," *J of Electrochemical Society* [Under Review]

[79] N. Maani, V. S. Rayz, and M. Nosonovsky, "Biomimetic approaches for green tribology: from the lotus effect to blood flow control," *Surface Topography: Metrology and Properties,* vol. 3, no. 3, p. 034001, 2015, doi: 10.1088/2051-672X/3/3/034001.

[80] N. Maani, D. Yee, J. R. Greer, S. W. Hetts, M. Nosonovsky, and V. L. Rayz, "Computational modeling in design of endovascular Chemofilter device for removing toxins from blood," ed, 2017, pp. 1-1.

[81] S. C. Cotter, "A Screening Design for Factorial Experiments with Interactions," *Biometrika,* vol. 66, no. 2, pp. 317-320, 1979, doi: 10.2307/2335664.

[82] J. R. Welty, *Fundamentals of momentum, heat, and mass transfer,* 3rd ed.. ed. New York: New York : Wiley, 1984.

[83] B. J. Kirby, *Micro- and nanoscale fluid mechanics : transport in microfluidic devices*. New York: New York : Cambridge University Press, 2010.

[84] R. Schlögl and F. Helfferich, "Comment on the Significance of Diffusion Potentials in Ion Exchange Kinetics," *The Journal of Chemical Physics,* vol. 26, no. 1, pp. 5-7, 1957, doi: 10.1063/1.1743264.

[85] F. A. Glaski and J. S. Dranoff, "Ion exchange kinetics: A comparison of models," *AIChE Journal,* vol. 9, no. 3, pp. 426-431, 1963, doi: 10.1002/aic.690090332.

[86] N. P. Balsara and J. Newman, "Relationship between steady-state current in symmetric cells and transference number of electrolytes comprising univalent and multivalent ions," *Journal of the Electrochemical Society,* vol. 162, no. 14, pp. A2720-A2722, 2015, doi: 10.1149/2.0651514jes.

[87] I. Villaluenga *et al.*, "Negative Stefan-Maxwell Diffusion Coefficients and Complete Electrochemical Transport Characterization of Homopolymer and Block Copolymer Electrolytes," *Journal of The Electrochemical Society,* vol. 165, no. 11, pp. A2766-A2773, 2018, doi: 10.1149/2.0641811jes.

[88] S. Neelamegham, H. Shankaran, and P. Alexandridis, "Aspects of hydrodynamic shear regulating shear-induced platelet activation and self-association of von Willebrand factor in suspension," *Blood,* vol. 101, no. 7, pp. 2637-2645, 2003, doi: 10.1182/blood-2002-05-1550.

[89] P. A. Aarts, S. A. van Den Broek, G. W. Prins, G. D. Kuiken, J. J. Sixma, and R. M. Heethaar, "Blood platelets are concentrated near the wall and red blood cells, in the center in flowing blood," *Arteriosclerosis, Thrombosis, and Vascular Biology,* vol. 8, no. 6, pp. 819-824, 1988, doi: 10.1161/01.ATV.8.6.819.

[90] J. Apel, R. Paul, S. Klaus, T. Siess, and H. Reul, "Assessment of Hemolysis Related Quantities in a Microaxial Blood Pump by Computational Fluid Dynamics," *Artificial Organs,* vol. 25, no. 5, pp. 341-347, 2001, doi: 10.1046/j.1525-1594.2001.025005341.x.

[91] E. R. Marx, "Platelet-Rich Plasma (PRP): What Is PRP and What Is Not PRP?," *Implant Dentistry*, vol. 10, no. 4, pp. 225-228, 2001, doi: 10.1097/00008505-200110000-00002.

[92] R. Ramachandran, "Vibrations and spatial patterns in biomimetic surfaces: using the shark-skin effect to control blood clotting," *Philosophical Transactions. Series A, Mathematical, Physical, And Engineering Sciences*, vol. 374, no. 2073, 2016, doi: 10.1098/rsta.2016.0133.

PUBLICATIONS

1- N. Maani, V. S. Rayz, and M. Nosonovsky, "Biomimetic approaches for green tribology: from the lotus effect to blood flow control," *Surface Topography: Metrology and Properties,* vol. 3, no. 3, p. 034001, 2015, doi: 10.1088/2051-672X/3/3/034001.

2- R. Ramachandran, "Vibrations and spatial patterns in biomimetic surfaces: using the shark-skin effect to control blood clotting," *Philosophical Transactions. Series A, Mathematical, Physical, And Engineering Sciences,* vol. 374, no. 2073, 2016, doi: 10.1098/rsta.2016.0133.

3- N. Maani, S. W. Hetts, and V. L. Rayz, "A two-scale approach for CFD modeling of endovascular Chemofilter device," *Biomechanics and Modeling in Mechanobiology,* journal article vol. 17, no. 6, pp. 1811-1820, December 01 2018, doi: 10.1007/s10237-018-1058-z.

4- N. Maani, T. Diorio, S. Hetts, and V. Rayz, "Computational Modeling of Drug Transport and Mixing in the Chemofilter Device: Enhancing the Removal of Chemotherapeutics from Circulation," *Biomechanics and Modeling in Mechanobiology,* [Under Review]